



HAL
open science

Synthesis and characterization of acoustic-sensitive perfluorinated microvesicles and nanocapsules for theranostic application

Guilherme Picheth

► **To cite this version:**

Guilherme Picheth. Synthesis and characterization of acoustic-sensitive perfluorinated microvesicles and nanocapsules for theranostic application. Galenic pharmacology. Université Paris Saclay (COMUE); Universidade federal do Paraná (Brésil), 2017. English. NNT : 2017SACLS105 . tel-02085930

HAL Id: tel-02085930

<https://theses.hal.science/tel-02085930>

Submitted on 1 Apr 2019

HAL is a multi-disciplinary open access archive for the deposit and dissemination of scientific research documents, whether they are published or not. The documents may come from teaching and research institutions in France or abroad, or from public or private research centers.

L'archive ouverte pluridisciplinaire **HAL**, est destinée au dépôt et à la diffusion de documents scientifiques de niveau recherche, publiés ou non, émanant des établissements d'enseignement et de recherche français ou étrangers, des laboratoires publics ou privés.

NNT : 2017SACLS105

THESE DE DOCTORAT
DE
L'UNIVERSITE PARIS-SACLAY
ET
UNIVERSIDADE FEDERAL DO PARANA
PREPAREE A
“ L'UNIVERSITE PARIS-SACLAY ”

ECOLE DOCTORALE N°425
Innovation thérapeutique du fondamental à l'appliqué
Spécialité de doctorat : Pharmacotechnie et Physico-chimie Pharmaceutique

Par

M. Guilherme Picheth

Synthesis and characterization of acoustic-sensitive perfluorinated microvesicles and nanocapsules for theranostic application

Thèse présentée et soutenue à Curitiba, le 15 février 2017:

Composition du Jury :

M. Freitas, Rilton, Professeur, Universidade Federal do Paraná, Directeur de Thèse, Président du jury
M. Tsapis, Nicolas, Directeur de recherche, Université Paris-Saclay, Directeur de Thèse
Mme. Guterres, Silvia, Professeur, Universidade Federal do Rio Grande do Sul, Rapporteur
Mme. Bresolin, Tânia, Professeur, Universidade do Vale do Itajaí, Rapporteur
Mme. Klassen, Giseli, Professeur, Universidade Federal do Paraná, Rapporteur
M. Pontarolo, Roberto, Professeur, Universidade Federal do Paraná, co-directeur de Thèse

Abstract

Fluorinated materials are intensively used as ultrasound contrast agents (UCA) to facilitate the diagnosis of many diseases by real-time imaging. All the commercially available UCAs are microbubbles constituted by a perfluorinated gaseous-core stabilized by a monolayer of phospholipids, proteins or surfactants. Unfortunately, the theranostic application (i.e. therapeutic and diagnostic ability) of such materials are severely limited by the (i) poor stability of the fluorinated component, (ii) inherent micrometer size range and (iii) lack of effective compartments for drug accumulation. To overcome these limitations, we proposed two different strategies to improve the persistence of the fluorinated core and simultaneously provide functional interfaces for drug encapsulation.

The first approach involves intercalating chitosan with phospholipids (DSPC) to increase the stability of microvesicles containing the fluorinated gas decafluorobutane (C_4F_{10}). The affinity of DSPC and chitosan was disclosed by surface sensitive techniques and fluorescence microscopy. ^{19}F nuclear magnetic resonance (^{19}F -NMR) and *in vitro* ultrasound of chitosan-coated microvesicles exhibited intense signals of the gaseous-component after 48 h, twice as long compared to plain samples. Altogether, chitosan increased the stability of microvesicles and is a suitable platform for drug accumulation. As a result, the chitosan-phospholipid shell may enhance the theranostic potential of related microvesicles. However, the use of a fluorinated gas-core imposed an important restriction to stabilize sub-micrometric vesicles. Therefore, the second strategy was focused in developing a theranostic agent at the nanoscale by entrapping a liquid fluorinated core of perfluorohexane (PFH; C_6F_{14}) into a rigid polymeric shell of polylactide (PLA). To enhance the interaction of biodegradable polymers with perfluorocarbons, we synthesized PLA polymers containing five distinct lengths of fluorinated end-groups (from C_3F_7 until $C_{13}F_{27}$) by ring-opening polymerization of D,L-lactide. A greater extent of fluororous interactions was indicated by ^{19}F spin-spin relaxation time and, subsequently, all the block copolymers were formulated into spherical nanocapsules (NC) with average diameter of 150 nm as verified by transmission electron microscopy. ^{19}F -NMR showed that NC produced with fluorinated polymers increased two-fold the encapsulation efficiency of PFH compared with non-fluorinated derivatives. As a result, the NC echogenicity increased 10-fold for both fundamental and harmonic ultrasound imaging modalities. In addition, acoustic drop vaporization of PFH was successfully attained by focused ultrasound as observed by fragmented or disrupted morphologies in many samples. Effects of the fluorinated end-groups were further explored by a morphological evaluation of microcapsules (MC) produced with the polymers. Finally, both NC and MC present an interesting theranostic potential, being able to perform ultrasound-assisted diagnosis and potentially release drug contents when irradiated by high acoustic pressures.

Abstract

Compostos fluorados são intensamente utilizados como agentes de contraste ultrassônicos (ACU) por facilitar o diagnóstico de diversas doenças via geração de imagens em tempo-real. Todos os ACU disponíveis comercialmente são microbolhas constituídas por um núcleo gasoso fluorado que é estabilizado por finas camadas de fosfolipídios, proteínas ou surfactantes. Infelizmente, a aplicação terapêutica (i.e. habilidade terapêutica e diagnóstica) de tais compostos é severamente limitada devido a (i) baixa estabilidade do componente fluorado, (ii) tamanho inerente à escala micrométrica, (iii) ausência de compartimentos efetivos para acumulação de fármacos. A fim de superar estas limitações, nós propomos duas estratégias distintas para aumentar a persistência do núcleo fluorado e, simultaneamente, prover interfaces funcionais para encapsulação de fármacos.

A primeira abordagem envolve a intercalação de quitosana com fosfolipídios (DSPC) a fim de aumentar a estabilidade de microvesículas contendo o gás fluorado decafluorobutano (C_4F_{10}). A afinidade entre DSPC e quitosana foi inicialmente verificada através de técnicas sensíveis de superfície e microscopia de fluorescência. Análises de ressonância magnética nuclear de ^{19}F (^{19}F -RMN) e imagens ultrassônicas *in vitro* mostraram sinais intensos do componente gasoso após 48h, o dobro comparado com amostras sem quitosana. Desta forma, o revestimento com quitosana foi capaz de prolongar a estabilidade de microvesículas e consiste em uma plataforma adequada para acumulação de fármacos. A camada interfacial formada por DSPC-quitosana pode, portanto, incrementar o potencial terapêutico de microvesículas. Entretanto, o uso de gás fluorado impôs uma importante restrição à estabilização de vesículas na escala nanométrica. Assim, a segunda estratégia estudada neste trabalho foi focada no desenvolvimento de agentes com habilidade terapêutica na nanoescala. Para tal, buscou-se encapsular um líquido fluorado, o perfluorohexano (PFH; C_6F_{14}), dentro um rígida cápsula polimérica de polilactídio (PLA). A fim de melhorar a interação entre polímeros biodegradáveis para com perfluorocarbonos, nós sintetizamos polímeros de PLA contendo grupamentos terminais fluorados com cinco diferentes comprimentos (desde C_3F_7 até $C_{13}F_{27}$) via polimerização por abertura de anel do D,L-lactídio. Resultados de relaxação ^{19}F spin-spin mostraram a presença de interações entre os componentes fluorados e, subsequentemente, todos os polímeros foram formulados em nanocápsulas (NC) esféricas com um diâmetro de 150 nm como verificado por microscopia eletrônica de transmissão. Ensaios de ^{19}F -RMN mostraram que as NC preparadas com polímeros fluorados dobraram a eficiência de encapsulação de PFH comparado com derivativos não fluorados. Estas NC aumentaram a ecogenicidade em 10 vezes para modalidades de imagens ultrassônicas fundamental e harmônica. Além disso, a vaporização acústica do PFH foi realizada por ultrassom focalizado, através da observação de cápsulas fragmentadas ou despedaçadas em diversas amostras. Os efeitos provenientes dos grupamentos fluorados foram explorados via avaliação da morfologia de microcápsulas (MC) produzidas com os polímeros. Finalmente, tanto as NC como as MC apresentam um interessante potencial terapêutico, sendo capazes de efetuar diagnóstico assistido por ultrassom e são potencialmente hábeis em liberar fármacos quando irradiados por altas pressões acústicas.

Abstract

Les composés fluorés sont très utilisés dans les agents de contraste ultrasonore (ACU) pour faciliter le diagnostic de nombreuses maladies par imagerie en temps réel. Tous les ACU commerciaux sont des microbulles de gaz perfluoré stabilisé par une monocouche de phospholipides, protéines ou tensioactifs. Cependant, l'application théranostique (de la contraction de thérapeutique et de diagnostic) de ces matériaux est sévèrement limitée par (i) la faible stabilité du composé fluoré, (ii) leur taille micrométrique et (iii) le manque de compartiments efficaces pour l'encapsulation d'un principe actif. Nous avons proposé deux stratégies différentes pour améliorer la stabilité du cœur fluoré et fournir simultanément des interfaces fonctionnelles pour l'encapsulation d'un principe actif.

La première approche a consisté à intercaler le chitosane avec des phospholipides (DSPC) pour augmenter la stabilité de microvésicules contenant du gaz fluoré décafluorobutane (C_4F_{10}). L'affinité du DSPC et du chitosane a été révélée par des techniques de caractérisation de surface et par microscopie à fluorescence. Les microvésicules contenant du chitosane ont présenté des signaux intenses de la composante gazeuse en résonance magnétique nucléaire du fluor (RMN ^{19}F) et en échographie *in vitro* après 48 h, deux fois plus longtemps que les échantillons sans chitosane. Le chitosane permet ainsi d'augmenter la stabilité des microvésicules et constitue une plateforme appropriée pour l'encapsulation de médicaments. La coque de chitosane-phospholipide pourrait donc améliorer le potentiel théranostique de ces microvésicules. Cependant, l'utilisation d'un cœur gazeux a rendu la stabilisation de vésicules submicrométriques difficile. Par conséquent, la deuxième stratégie s'est focalisée sur le développement d'un agent théranostique à l'échelle nanométrique en piégeant un cœur fluoré liquide de perfluorohexane (PFH; C_6F_{14}) dans une enveloppe polymère rigide de polylactide (PLA). Pour améliorer l'interaction des polymères biodégradables avec les perfluorocarbones, nous avons synthétisé des polymères PLA contenant cinq longueurs différentes de groupes terminaux fluorés (de C_3F_7 à $C_{13}F_{27}$) par polymérisation par ouverture de cycle du D,L-lactide. Les mesures de temps de relaxation spin-spin ^{19}F ont démontré la présence d'interactions fluorophiles intenses entre les chaînons fluorés et le PFH. Les polymères ont ensuite été formulés en nanocapsules (NCs) sphériques de 150 nm de diamètre, comme vérifié par microscopie électronique en transmission. La RMN ^{19}F a montré que l'efficacité d'encapsulation du PFH dans les capsules est doublée grâce à l'utilisation des polymères fluorés comparé aux dérivés non fluorés. Par conséquent, la réponse acoustique des NCs a été multipliée par dix avec les deux modes d'imagerie fondamentale et harmonique. En outre, l'utilisation d'ultrasons focalisés a permis la vaporisation acoustique de gouttelettes de PFH, confirmée par l'observation de morphologies fragmentées ou perturbées dans de nombreux échantillons. Les effets des groupes terminaux fluorés ont été davantage explorés par une évaluation morphologique des microcapsules (MCs) produites avec les polymères. Finalement, les NCs et MCs présentent un potentiel théranostique intéressant, puisqu'elles permettent d'effectuer un diagnostic assisté par ultrasons et de libérer potentiellement un principe actif lorsqu'elles sont soumises à des pressions acoustiques élevées.

Acknowledgements

First and foremost I would like to thank all of my supervisors, Prof. Roberto Pontarolo, Prof. Rilton Alves de Freitas, Dr. Nicolas Tsapis and Dr. Laurence Moine. I'm extremely grateful for all of the contributions, ideas, funding and time they devoted to me. All of them, in it's own particular way, has shared precious amounts of knowledge that inspired me in the pursuit of my Ph.D.

I'm especially thankful to Prof. Maria Rita Sierakowski for all the contributions to my work and for kindly receiving me at the Laboratório de biopolímeros since 2011. I would also like to thank Prof. Elias Fattal for welcoming me at the Institut Galien in Châtenay-Malabry.

I'm thankful to Dr. Ana Camarozano and Dr. Olivier Couture for all the help with ultrasound experiments and interesting discussions.

I would like to specially thank Sophie Houvenagel and Cleverton Pirich. To Sophie, for her sympathy, solicitude and for the very important contributions made to my work. To Cleverton for all of his help with the experiments, discussions and interest in pushing our research forward.

Thanks to Renata Silva, Andressa Martin, Vivian Spier, Gabriel Kaminski, Caroline Sakakibara, Helen Bassani and Larissa Antoniacomi, all from the Biopol group in Brazil with whom I shared great moments during the time we spent in the laboratory.

Thanks to Jean Baptiste Coty, Marie-Line Helou, Rosana Simon, Felix Sauvage, Marion Quaillet, Barbara Tessier, Emilie Langlois, Ludivine Mousnier, Tanguy Boissenot, Mathilde Lorscheider, Thais Leite, Henrique Marcelino, Herman Palacio and Walhan Alshaer, all from the Université Paris-Saclay. Their help and friendship were fundamental during my period in France.

Thanks to the NMR specialists Fernanda Ocampos, Leociley Menezes, Camille Dejean, Prof. Anderson Barisson and Prof. Jaísa Soares.

Finally, I'm thankful to my parents, Geraldo and Cyntia Picheth, who have supported and stimulated me with great enthusiasm during all my academic life.

Table of Contents

Abbreviations	10
General Introduction	12
Literature review	14
1. Theranostic agents	15
1.2. Enhanced Permeability and Retention Effect.....	17
1.3. Ultrasound.....	20
1.3.1. Ultrasound Parameters	21
1.3.2. Ultrasound Diagnostic Imaging	24
1.3.2.1. Ultrasound Contrast Agents	26
1.3.2.2 UCA acoustic response	29
1.3.2.3 Harmonic Imaging.....	31
1.3.3 Therapeutic ultrasound.....	33
2. References	36
Objectives.....	43
Gaseous-core microvesicles coated with chitosan	44
Chitosan-coated microvesicles: effect of polysaccharide-phospholipid affinity on decafluorobutane dissolution	46
1. Introduction.....	48
2. Materials and methods	50
2.1 Chemicals	50
2.2 Quartz Crystal Microbalance (QCM)	50
2.3 Infrared Spectroscopy	51
2.4 Atomic Force Microscopy.....	51
2.5 Contact Angle Analysis	51
2.6 Microvesicles preparation	52
2.7 Fluorescence Microscopy.....	52
2.8 Differential Scanning Calorimetry.....	53
2.9 Decafluorobutane quantification – ¹⁹ F-NMR	53
2.10 In vitro Ultrasound	53
3. Results and Discussion.....	54
3.1 Phospholipid-chitosan interaction	54
3.2 In vitro stability of microvesicles	57
4. Conclusion	60
5. Acknowledgements	60
6. References	61
Synthesis of fluorinated polymers for nanocapsule formulation.....	65
1. Introduction.....	69
2. Materials and Methods.....	71
2.1 Materials	71
2.2 Polymer Synthesis	71
2.3 Characterization	72
2.4 Differential Scanning Calorimetry (DSC)	72
2.5 Nanocapsules Formulation	73
2.6 Size and ζ-potential.....	73
2.7 Electron Microscopy.....	73

2.8 PFH encapsulation efficiency	74
2.9 Cell viability	74
2.10 In vitro Ultrasound Characterization	75
2.11 Focused Ultrasound	76
3. Results and discussion	77
3.1 Synthesis and characterization of fluorinated polymers	77
3.2 PFH Nanocapsules	79
3.3 In vitro cytotoxicity of NCs.....	82
3.4 In vitro Ultrasound imaging.....	84
3.5 PFH vaporization by FUS	85
4. Conclusions	87
5. Acknowledgements	87
6. References	89

Dynamics and influence of F-polymers over microcapsules 94

Influence of fluorinated end-group dynamics on the morphology of microcapsules	96
1. Introduction.....	98
2. Materials and Methods.....	100
2.1 Materials	100
2.2 Polymer Synthesis	100
2.3 Characterization	101
2.4 Interfacial surface tension	101
2.6 Microcapsules Formulation	102
2.7 Confocal Microscopy.....	103
2.8 Scanning Electron Microscopy.....	103
2.9 PFH encapsulation efficiency by ¹⁹ F-NMR spectroscopy	103
2.10 Focused ultrasound.....	104
3. Results and Discussion.....	105
3.1 Polymers synthesis and characterization.....	105
3.2 Polymers dynamics.....	105
3.3 Solvent Influence on MC formulation	109
3.5 MC characterization and ultrasound	113
4. Conclusion	114
5. Acknowledgements	114
6. References	115

General Discussion 120

General Discussion	121
1.1 Gas-core microvesicle stabilization and functionalization	122
1.2 Formulation	122
1.3 Theranostic potential	123
1.3.1 Ultrasound Imaging.....	123
1.3.2 Drug uptake and release mediated by ultrasound	124
1.4 Limitations.....	126
2. Nano and microcapsules	127
2.1 Interfacial behavior of fluorinated polymers.....	128
2.2 Polymer dynamics	131
2.3 Solvent influence on PFH entrapment and MC morphology	136
2.4 Theranostic potential	139
2.4.1 Imaging	139
2.4.1.2 Ultrasound imaging.....	139
2.4.1.3 ¹⁹ F-MR imaging	141

2.4.2 Drug release mediated by ultrasound	142
3. References	144
General conclusion	151

Abbreviations

AFM – Atomic force microscopy

AM – Amplitude modulation

CryoTEM – Cryogenic transmission electron microscopy

CT – Computed tomography

DCM – Dichloromethane

DNA – Deoxyribonucleic acid

DSC – Differential scanning calorimetry

DSPC – 1,2-distearoyl-sn-glycero-3-phosphocholine

EPR – Enhanced permeability and retention effect

FDA – Food and drug administration

FITC – Fluorescein isothiocyanate

FTIR – Fourier transformed infrared

FUS – Focused ultrasound

HIFU – High intensity focused ultrasound

HUVEC – Human endothelial umbilical vein cells

J774 - Murine macrophage-monocytes

MC – Microcapsule

MI – Mechanical index

MMP – Promatrix metalloproteinase

MRI – Magnetic resonance imaging

MTT – 3-(4,5-dimethylthiazol-2-yl)-2,5-diphenyltetrazolium bromide

Mv – Microvesicle

MvC – Microvesicle coated with chitosan

NC – Nanocapsule

NIR – Near infrared

NMR – Nuclear magnetic resonance

NP – Nanoparticle

PBS – phosphate buffer saline

PCL – poly(ϵ -caprolactone)

PDI – Polydispersity index

PEG – Polyethylene glycol

PET – Positron emission tomography
PFC – Perfluorocarbon
PFCE – Perfluoro-crow-ether
PFH – perfluorohexane
PFOB – perfluorooctyl bromide
PFP – Perfluoropentane
PI – Pulse inversion
PIAM – Pulse inversion and amplitude modulation
PLA – poly(lactide)
PLA-*b*-PEG – poly(lactide)-*b*-polyethylene glycol
PLGA – poly(lactide)-co-glycolide
PLGA-*b*-PEG – poly(lactide-co-glycolide)-*b*-polyethylene glycol
PVA – Polyvinyl alcohol
QCM – quartz crystal microbalance
ROP – Ring opening polymerization
SC – Sodium cholate
SEC – Size exclusion chromatography
SEM – Scanning electron microscopy
SFE – Surface free energy
SNR – Signal-to-noise ratio
SPECT – Single photon emission computed tomography
TEM – Transmission electron microscopy
TFA – Trifluoroacetic acid
THF – Tetrahydrofuran
TI – Thermal index
UCA – Ultrasound contrast agent
US – Ultrasound

General Introduction

Cancer is the leading cause of death worldwide with a projected increase of 45% in cases until 2030 (up to 11.5 million deaths). In developed countries, cancer is the second cause of deaths, surpassed only by heart diseases, affecting people of all ages with one out of three people will experience a cancer diagnosis during their lifetime (Orellana 2003).

However, even after 100 years of intense research, the conventional cancer chemotherapy is not always successful. The standard treatments are based on the delivery of toxic anticancer agents indiscriminately, reaching both tumors and healthy tissues (Iyer, Khaled et al. 2006). This lack of specificity often generates undesirable side-effects and creates an urge in the development of drugs or delivery systems able to recognize particular cancerous “fingerprints”, such as modified metabolism (Tennant, Duran et al. 2010), altered cell-signaling molecules (Dube and Bertozzi 2005) or fenestrated vasculature (Maeda 2015). In this context, Paul Ehrlich’s vision of a magic bullet, a “personalized and tailored drug” that precisely target molecular defects in a highly specific fashion has become a crucial concept for advanced cancer treatment (Strebhardt and Ullrich 2008).

A recent approach that combines real-time imaging and local drug-delivery performed by a single agent displays an unmatched potential to personalize and improve the outcome of cancer treatments. These so-called theranostic systems may selectively deliver therapeutics to tumors with pin-pointed accuracy and dramatically increase the chemotherapy efficacy. In this thesis, we describe the development of theranostic micron and nano-sized agents sensitive to ultrasonic pulses.

This manuscript is divided into 5 sections. The first chapter is devoted to a general context based on bibliographic evidences, involving the theranostic concept explored into micron and nano-sized systems with ultrasonic sensitivity. The sections 2-4 concern the developed experimental work in the form of three publications. Initially, the formulation of ultrasound-sensitive microvesicles coated with chitosan for improved perfluorocarbon stability and potential theranostic use is presented (chapter 2). Next, the synthesis and influence of end-group fluorinated polymers is considered in the development of nanotheranostic capsules containing a liquid perfluorocarbon core. The impact of the fluorinated groups comprising different

lengths on nanocapsule morphology and the inherent acoustic response under clinical and focused ultrasound are presented in chapter 3. Finally, the role of the fluorinated interfaces to improve the stability of perfluorocarbons is microscopically evaluated in formulated microcapsules (chapter 4). At the end of the manuscript (chapter 5), a general discussion will confront the obtained results with the literature, present limitations and highlight new perspectives for the proposed systems.

Chapter 1

Literature review

1. *Theranostic agents*

“Theranostics” are versatile materials able to perform both therapy and diagnostic in a single object (Funkhouser 2002). This term defines an integrated system that may diagnose, deliver targeted drugs and also monitor the response of diseased tissues to applied therapies in a single administered dose. It is assumed that combining real-time imaging with local drug delivery will improve the management of tumor treatment, reducing risks and costs compared to the current chemotherapy (Ahmed, Fessi et al. 2012).

This interesting approach also opposes the concept that “one fits all” and introduces the possibility of individualized treatments for several diseases, allowing the assessment and subsequent therapy of tumors with distinct phenotypes and heterogeneities as well as reducing the numerous side effects (Kelkar and Reineke 2011). In fact, the monitoring of drug accumulation in targeted areas offers an unprecedented possibility to treat specific individual responses to a certain disease, also screening and selecting patients who could benefit from alternative therapies (e.g. surgery or conventional chemotherapy).

To this end, “classical” drug-delivery systems or contrast agents used in clinical imaging (e.g. liposomes, nanocapsules or microbubbles) are being co-loaded with imaging probes and drug payloads (Lammers, Aime et al. 2011). Theranostic agents are multifunctional systems that effectively integrate imaging probes to drug-loaded carriers, presenting distinct architectures and building blocks, such as drug-polymer conjugates, polymeric/magnetic nanoparticles (NP), solid-lipid NP, dendrimers, liposomes and microvesicles (Bardhan, Lal et al. 2011). The anchoring or accumulation of extracorporeal tracking components allows *in vivo* and non-invasive imaging by many distinct techniques, such as magnetic resonance imaging (MRI), X-ray computed tomography (CT), positron emission tomography (PET), single-photon emission computed tomography (SPECT), near infrared (NIR) or ultrasound (Table 1) (Ding and Wu 2012). A subsequent drug-release may be locally triggered by pH or enzymes and also by the transmission of extracorporeal stimuli, such as temperature increase, external magnetic fields or acoustic waves (You, Wang et al. 2016). Additionally, the development of systems able to perform passive (based on the enhanced permeability and retention effect) or active targeting present an unmatched potential to treat and monitor diseases at their earliest development

stage, thus, increasing the possibility of cure (Jo, Ku et al. 2016). The versatility of theranostic agents is illustrated in Figure 1, exhibiting the potential of theranostics in performing distinct imaging techniques, releasing drugs once stimulated and reaching the desired tissue via active or passive targeting (Mura and Couvreur 2012).

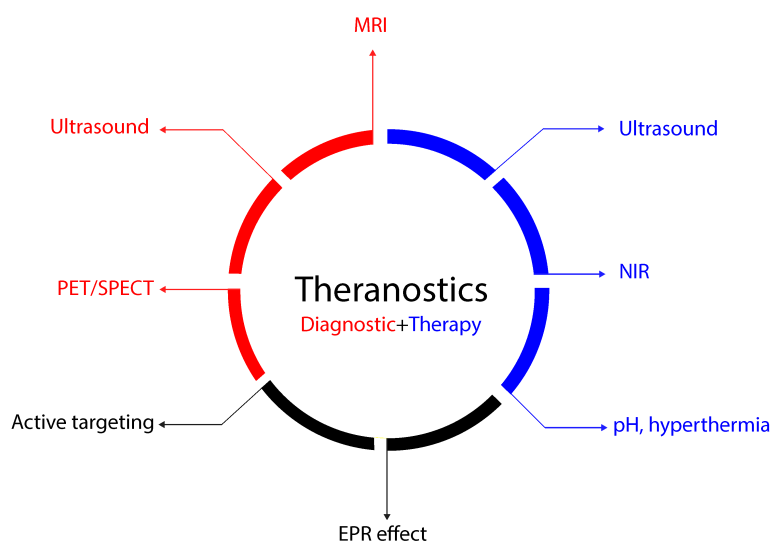


Figure 1. Schematic representation of theranostic agent design. The same system is able to respond to non-invasive imaging techniques (e.g. MRI, ultrasound or PET/PECT scan) releasing its drug content by specific stimuli (e.g. acidic pH, particular enzymes or hyperthermia) or triggering mechanisms (e.g. ultrasound or NIR), and may also target active or passively diseased tissues.

Nevertheless, several drawbacks still limits such all-in-one approach; for example, a correct ratio of diagnostic and therapeutic components may not always be assembled in a composite suitable for *in vivo* applications. Also, the biocompatibility and toxicological profile are also matter of intense discussion since the safety of the system building blocks does not ensure innocuity of the entire system (Sharma 2014). In addition, many of the employed imaging agents present a potential toxicity. As a result, a great deal of intense research and development efforts is still required for an effective introduction of theranostic agents in the medical practice (Mura and Couvreur 2012).

Table 1. Theranostic Imaging and therapy modalities indicated by the respective extracorporeal tracking probes and therapeutic agents. Adapted from Bardhan *et al.* 2011 (Bardhan, Lal *et al.* 2011).

Type	Modality	Agent
Imaging	Fluorescence	Quantum dots, organic fluorophores
	MRI	Iron oxide NP, gadolinium chelates, perfluorocarbons
	PET, SPECT	Radioisotopes (^{64}Cu , ^{18}F , ^{124}I , ^{111}In)
	CT	Iodine, gold nanoparticles
	Ultrasound	Perfluorocarbons
Therapy	Chemotherapy	Doxorubicin, paclitaxel and other anticancer drugs
	Gene therapy	siRNA, DNA
	Radiotherapy	^{64}Cu radionuclide

1.2. Enhanced Permeability and Retention Effect

Selective targeting to tumor cells still remains one of the greatest challenges in the current pharmaceutical chemotherapy. However, a phenomenon originally proposed by Matsumura and Maeda in 1986 (Matsumura and Maeda 1986), the enhanced permeability and retention effect (EPR), has provided new concepts in the design of drug-delivery systems addressed to tumor treatment.

The EPR effect is characterized by local tumor angiogenesis to provide additional metabolic income for newly developed cells. As tumor cells multiply, the local neovascularization process is induced to fully supply the developing tissue with increased demands of oxygen and nutrients (Maeda 2002). Nevertheless, this vasculature is essentially distinct from healthy tissues, presenting irregular shapes with poorly aligned endothelial cells. This aberrant morphology is normally dilated and exhibits large fenestrations that allow the leakage of blood plasma components (Iyer, Khaled *et al.* 2006). Combined with the inefficient lymphatic clearance and a characteristic slow venous return of solid tumors, macromolecules and specially designed intravascular nanostructured drug-carriers larger than 40 kDa might accumulated in various tumors, while concentrations in normal organs and tissues remain low (Figure 2A) (Clark, Wiley *et al.* 2016). This passive accumulation or EPR

effect has increasingly drawn the attention of researchers and may constitute one of the basis of future tumor therapy (Kobayashi, Sano et al. 2014) (Jeong, Kang et al. 2016). Conversely, low molecular weight drugs diffuses rapidly in the circulating blood and are eliminated by renal clearance (Maeda 2015).

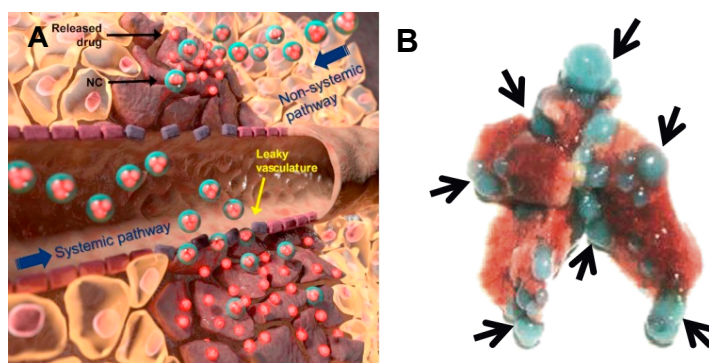


Figure 2. Schematic illustration of nanocarrier drug delivery by systemic mediated by the EPR effect and non-systemic pathway (A). EPR effect demonstrated by albumin (70 kDa) stained with Evans blue accumulation in lung cancer metastatic tumor nodules (B). Adapted from Jeong *et al.* 2016 (Jeong, Kang et al. 2016) and Maeda 2015 (Maeda 2015).

The increased tumor vascular permeability is modulated by the release and the constant demand of several signaling mediators (Table 2). The known inducers of neovascularization include the vascular permeability factor, bradykinin and nitric oxide. Other factors that enhance tumor development and local retention of macromolecules are prostaglandins – which reduce the blood flow in the tumor bed – and peroxynitrite – that activates promatrix-metalloproteinases (MMPs) to degrade the extracellular matrix and facilitate the tumor invasiveness (Iyer, Khaled et al. 2006).

Table 2. Factors affecting the EPR effect in solid tumors. Adapted from Maeda 2015 (Maeda 2015).

Mediators	Responsible enzymes or mechanisms
Bradykinin	Kallikrein/protease
Nitric oxide	By inducible nitric oxide synthase
Vascular permeability factor	Involved in NO generation
Prostaglandins	By cyclooxygenase 1
Collagenase (MMPs)	By activation from pro-MMPs
Peroxyntirite	Produced by $\text{NO} + \text{O}_2^- \rightarrow \text{ONOO}^-$

Carbon monoxide	By Heme oxygenase
Induced hypertension	Using angiotensin II
Inflammatory cells	Neutrophil/NADPH oxidase, etc.
Transforming growth factor inhibitor	Activation of inflammatory reaction
Tumor necrosis factor	Activation of inflammatory reaction
Anticancer agents	Reactive oxygen species generation
Heat	Activation of pro inflammatory mediators
Blood pressure	Hydrodynamic systolic blood pressure

As pre-requisites for EPR targeting, selected macromolecules or drug-delivery systems must be biocompatible, sufficiently small to pass the fenestrated vasculature (~100 nm) and remain in the bloodstream for a prolonged time (>6h) (van de Ven, Kim et al. 2012). Therefore, many classes of nanomedicines have been developed for diverse applications based on the EPR effect, providing significant improvements in pharmacokinetics, toxicity and biodistribution compared to freely administered molecules, increasing the overall drug accumulation in tumors. According to Maeda *et al.* 2000 (Maeda, Wu et al. 2000), the EPR targeting is already considered a gold standard for novel drug design.

However, tumors are highly diverse and heterogeneous, varying in size, pathological characteristics (e.g. primary or metastatic), etiologies, vascular densities and treatment history (Figure 2B). In fact, even experimental models, such as orthotopic and autochthonous also present different features, which hinders a uniform nanomedicine treatment response (Maeda 2015).

Although the passive targeting using nanomedicine has provided more efficient therapeutic outcomes compared to conventional chemotherapy, improvements in tissue selectivity, cellular recognition and drug uptake strategies are still required for the achievement of an uniform drug availability (Choi, Chung et al. 2010). In general, selective accumulation driven by the EPR effect varies according to tumor vascular heterogeneity and drug contents are reported to increase only up to 30% of the initial dose in tumors (Prabhakarandian, Shen et al. 2015) (Kobayashi and Choyke 2016).

Despite the tumor heterogeneity, the EPR effect might be modulated or enhanced with effectors to provide higher drug concentrations into the tumor bed and generate more homogeneous responses. For example, recent reports already

correlate a combined nanomedicine treatment – pirarubicin conjugated with hexamethylphosphoramide copolymer – with radiotherapy, revealing an effective remission of metastatic nodules in the lungs and bones (Dozono, Yanazume et al. 2016). Also, by utilizing NIR sensitive monoclonal antibodies – monoclonal antibody bound to absorbing phthalocyanine dye – Kobayashi *et al.* 2016 reported a significant increase on cell death induced by immediate necrosis (Kobayashi and Choyke 2016).

Among the many methodologies currently utilized to enhance drug uptake in tumor tissues by passive accumulation, ultrasound is considered one of the most promising techniques to trigger drug release into a desired tissue and synergistically enhance the therapeutic effect (Zheng, Jin et al. 2016). In fact, ultrasound is considered an ideal drug-release trigger mechanism for it provides spatial and temporal control over the transmission of mechanical and thermal energy. It also displays many advantages over light-based stimuli techniques, such as non-invasiveness, sub-milimetric precision and a maximum of 10 cm penetration depth (Duncanson, Arriaga et al. 2014) (Bezagu, Errico et al. 2014). Many recent studies report highly efficient treatments after focused ultrasound (FUS) exposure combined with liposomes (Liang, Gao et al. 2015) (Jeong, Hwang et al. 2016), nanoparticles (Zhang, Chen et al. 2014) or nanocapsules (Zhang, Li et al. 2016) (You, Wang et al. 2016).

1.3. Ultrasound

Ultrasound is a versatile technique with a long history in diagnostic imaging, though recent therapeutic applications have demonstrated an unparalleled potential to enhance and also reduce side effects in the treatment of diabetes, stroke, cancer, cardiovascular diseases, infections, osteoporosis, thrombosis, glaucoma, nerve damage, skin wounds and bone fractures as illustrated in Figure 3 (Mitragotri 2005). Ultrasound is a very popular technique for permitting the visualization of internal structures, stimulate cells and tissues as well as activate drug-carriers without being invasive (Calliada, Campani et al. 1998).

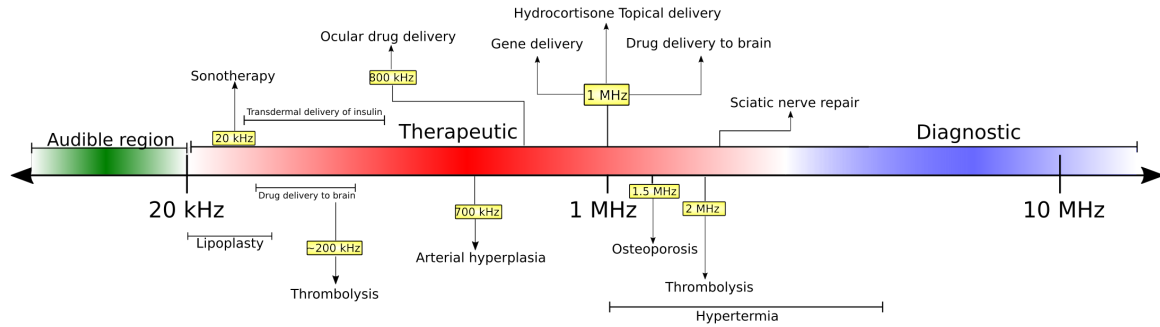


Figure 3. Therapeutic and diagnostic ultrasonic ranges in the medical practice. Adapted from Mitragori *et al.* 2005 (Mitragotri 2005).

As an acoustic pulse travels into the body, it interacts and creates periodic pressure oscillations – determined by the frequency and amplitude of the source – allowing image formation or inducing local stimulation by temperature increase and pressure oscillation (Mitragotri 2005). In general, ultrasound with diagnostic purposes (e.g. echocardiography) are not focused into a precise spot and allow real-time imaging of large body areas in a single exam (Boissenot 2015). Conversely, therapeutic ultrasound, currently used for thermal tumor ablation, focus on specific tissues to avoid damage to adjacent healthy cells (Bezagu, Errico et al. 2014) (Clark, Wiley et al. 2016). Hence, focused ultrasound is currently utilized to trigger the release of nucleic acids, chemotherapeutics and anti-inflammatory drugs from ultrasound-sensitive drug carriers in targeted tissues, thus, presenting an important role in the forthcoming clinical therapy.

1.3.1. Ultrasound Parameters

The response of distinct materials or tissues to ultrasound is dependent on the applied acoustic parameters. According to the propagation of the transmitted ultrasonic intensity, the local environment is affected by pressure variations with successive compression and rarefaction phases as illustrated in Figure 4. The intensity (I) of the effective pressure over a specific tissue might be calculated in W/cm^2 by the positive and negative ultrasonic peaks as shown in Equation 1.

$$I = P^2 / \rho_0 c \quad Eq. 1$$

where P is the acoustic pressure, ρ_0 is the tissue density and c is the ultrasound propagation velocity.

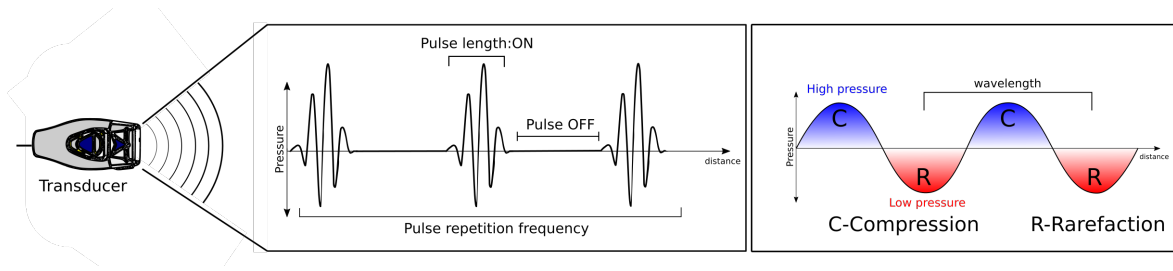


Figure 4. Ultrasound parameters. A transducer is positioned over the skin and transmits pulses with a determined repetition frequency to irradiate and detect scattered signals. Ultrasonic pulses are characterized by the transmission of high (compressive) and low (rarefractive) acoustic pressures along its course into the body.

The total applied intensity is an important safety parameter, since acoustic power higher than 5 W/cm^2 may cause irreversible tissue damage with dependency on tissue depth and wave attenuation. For the observation and focusing of deep structures into the body, lower ultrasonic frequencies are required because the wave is absorbed and attenuated during its transit along the tissues (Ahmadi, McLoughlin et al. 2012). The frequency dependence with ultrasound absorption might be estimated according to equations 2 and 3. The use of higher frequencies is indicated to stimulate or visualize superficial structures whereas lower values are employed for deep organs imaging. Unfortunately, resolution and penetration are inversely correlated as shown in Figure 5, thus, hindering an optimal observation of internal structures (Boissenot 2015).

$$P_x = P_o e^{-\alpha x}, \text{Eq. 2}$$

$$\alpha = \alpha_o f^n, \text{Eq. 3}$$

Where P_x is the acoustic pressure at a distance x from the source, P_o is the surface pressure at the transducer surface, α is the absorption coefficient, α_o is the reference absorption coefficient of the particular tissue, n is a factor related to the tissue's homogeneity (slightly higher than 1 for soft tissues) and f is the frequency.

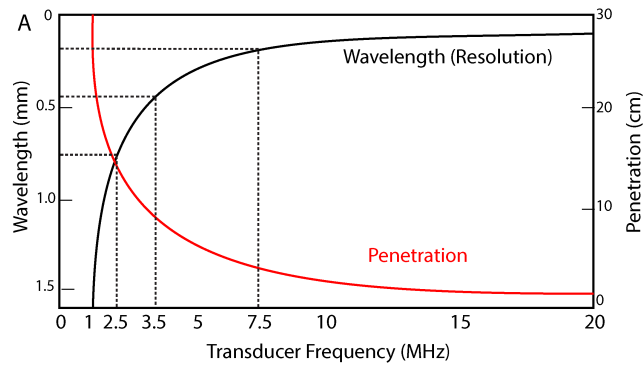


Figure 5. Evolution of penetration and spatial resolution as a function of ultrasound frequency. Adapted from Boissenot *et al.* (Boissenot 2015) and Otto *et al.* (Otto 2000).

The continuous irradiation of ultrasonic waves into the body, however, might lead to tissue destruction due to energy accumulation and heating (Ahmadi, McLoughlin *et al.* 2012). To avoid undesired damage, the pulse is modulated with on and off cycles with a determined repetition frequency, allowing the energy to dissipate between two impulsions as shown in Figure 4.

Ultrasound induces distinct biological effects depending on the employed acoustic parameters, determined as thermal or mechanical: thermal effects are related to energy absorption and temperature increase, prone to cause burns and necrosis due to protein denaturation. The local temperature increase up to a threshold of 43°C is correlated only with increased blood debit and vascular permeability, with important implication for localized drug delivery (Frenkel 2008). In this case, the tissues are not irreversibly damaged, even at long exposition (Dewey 2009). Oppositely, the application of higher temperatures than 43°C is usually employed to ablate tumor tissues, provoking a fast protein denaturation, cell death and degradation of the vascular system (Illing, Kennedy *et al.* 2005) (Boissenot 2015).

Mechanical effects are generally characterized by the interaction of ultrasound with gas bubbles or other intravascular contrast agents. The generation of bubbles arises from intense negative pressures in blood or tissues when insonified with high acoustic intensities: this is called cavitation (Bailey, Khokhlova *et al.* 2003). Their exposal to ultrasonic waves generates size oscillation according to the passage of negative (rarefaction) and positive (compression) pressure peaks. In general, two distinct behaviors are observed depending on the ultrasonic intensity: a linear size oscillation (inertial cavitation) or an asymmetric size oscillation followed

by disruption – nonlinear (non-inertial cavitation). The latter process may create mechanical stress on surrounding tissue and precipitate fluid microjet formation – bubble disruption that leads to the creation of jet streams, which are able to crash against cellular membranes and generate pores. This phenomenon called sonoporation is employed to enhance the penetration of nuclei acids into cells or to permeate drugs through the blood brain barrier (Frenkel 2008, Lentacker, De Cock et al. 2014).

The tissues that are more susceptible to cavitation effects are the lungs, intestine and bones due to the presence of residual gases and, thus, a precise control over ultrasonic parameters is required to avoid cavitation and undesired tissue damage (Boissenot, Bordat et al. 2016). The risk of cavitation and temperature increase might be evaluated through the mechanical (MI) and thermal indices (Eq. 4 and 5, respectively).

$$\text{Mechanical Index: } MI = \frac{P}{\sqrt{f}}, \text{ eq. 4}$$

$$\text{Thermal Index: } TI = \frac{W_p}{W_{deg}}, \text{ eq. 5}$$

where P is the peak negative pressure in MPa, f is the frequency in MHz, W_p is the attenuated acoustic intensity and W_{deg} is the intensity required to increase the tissue temperature by 1°C.

The maximum MI stipulated by the american surveillance department, the food and drug administration (FDA) is of 1.9 for safe ultrasound imaging exposure. Nevertheless, focused ultrasound might employ MI values above the recommended imaging range for succesfull tumor ablation therapies or targeting of specific drug-carriers. The TI value estimates the local temperature increase in degrees and a maximum of 43°C for diagnostic ultrasound is preconized by the FDA (Boissenot, Bordat et al. 2016).

1.3.2. Ultrasound Diagnostic Imaging

Ultrasound is the second most utilized imaging modality in the medical practice – only surpassed by X-ray in number on exams – and conventional ultrasound scanners are ubiquitous in hospitals worldwide (Shung 2015). This technique is non-invasive and presents many advantages, such as safety, lower

price, portability and ability to generate real-time images that distinguishes it from other competing modalities (e.g. X-ray computed tomography, magnetic resonance imaging and radionuclide emission tomography). Additionally, the capability to measure blood flow and perfusion according to the Doppler principle provides effective information about tissue function and represents a key tool for the diagnostic of arterial occlusion and congenital heart disease. Ultrasound imaging is mainly employed in cardiac, vascular, abdominal, obstetrics and urology for the detection of tumors, cardiac malformations and assessment of pregnancy (Camarozano 2013).

Modern ultrasonic scanners operate by transmitting electronically delayed pulses that produces high frequency sound waves in the range of 1 to 20 MHz by piezoelectric transducers – generally zirconate titanate. The echoes are generated by reflection as the ultrasonic wave passes and interacts with soft tissues of distinct acoustic impedances (e.g. organs with different compressibility and density, Eq. 6) (Figure 6). Such reflected signals are collected, processed and displayed as bidimensional or tridimensional images. As previously introduced, diagnostic ultrasound systems are not focused into a precise point in the scanned area and therefore allow real-time imaging of large body regions in a single exam (Powers and Kremkau 2011) (Boissenot 2015). Unfortunately, the ultrasound technology is currently incapable to generate useful images of internal bone tissue and gas-filled organs, such as lungs and bowel (Anderson 2000).

$$Z = \rho_0 c = \sqrt{\rho_0 c_{elas}}, eq. 6$$

where Z is the acoustic impedance, ρ_0 is the tissue density, c is the sound speed and c_{elas} is the tissue elasticity.

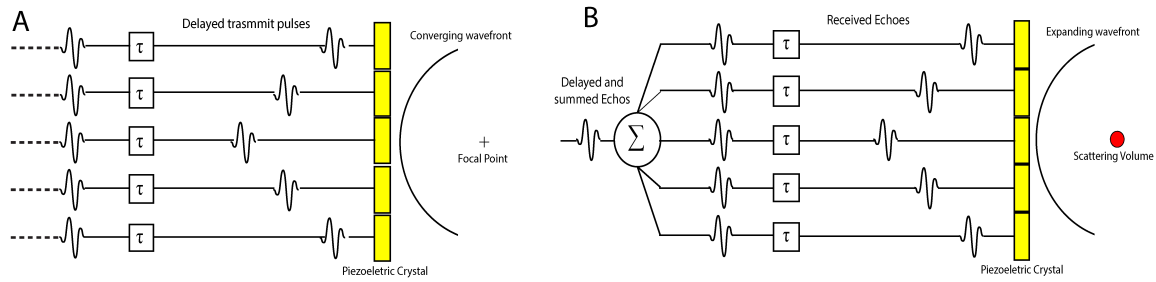


Figure 6. Schematic representation of ultrasonic image formation mechanism. Delayed pulses are transmitted from piezoelectric elements to achieve steering and focus (A). The returning echoes are delayed and summed to generate a strong signal for processing and imaging formation (B). Adapted from Anderson *et al.* 2000 (Anderson 2000).

Many distinct ultrasound imaging modalities might be performed – brightness, motion, amplitude and Doppler modes – and, although all present important roles in the diagnosis of many diseases, the brightness or B-mode is currently highlighted as the most employed one. The B-mode generates gray-scale images that are proportional to the echoes' amplitude as a function of their position in the scanned region (Anderson 2000). Also, distinct frequencies might be employed to modulate resolution and depth of penetration, with a range varying from 20 kHz up to values higher than 40 MHz (Ahmadi, McLoughlin *et al.* 2012) (Couture 2007).

1.3.2.1. *Ultrasound Contrast Agents*

Ultrasound contrast agents (UCAs) are intravascular echo-enhancers intensively utilized in cardiology and several oncological interrogations (Calliada, Campani *et al.* 1998) (Cosgrove 2006). As many structures lack of sufficient compressibility and density to favor the formation of well-resolved ultrasonic images, UCAs are normally employed to increase the resulting echo and provide enhanced contrast with respect to the tissues. In normal scanning conditions, the UCAs provide enhanced resolution of gray-scale images and therefore supports the diagnostic accuracy in the detection of thrombosis, endomyocardial fibrosis and hear ischemia (Camarozano 2013). Moreover, distinct multipulse ultrasonic sequences are employed to selectively detect and trace UCAs signals into the microvasculature or large vessels as sensitive markers of blood-pool (Cosgrove 2006) (Couture, Bannouf *et al.* 2009).

In general, UCAs are constituted of entrapped gases (e.g. air, sulfur hexafluoride, octafluoropropane and decafluorobutane) or liquids (e.g. perfluorooctyl bromide and perfluorohexane) stabilized by functional biomaterial shells composed of phospholipids, proteins or tensoactives (Figure 7) (Raisinghani, Rafter et al. 2004) (Diaz-Lopez, Tsapis et al. 2010) with an effective diameter inferior of 7.5 μm as required for safe transit through the capillary bed (Camarozano 2013). The UCA acoustic response is determined by the compressibility, as well as stability of both core and shell components (Jafari, Diou et al. 2014).

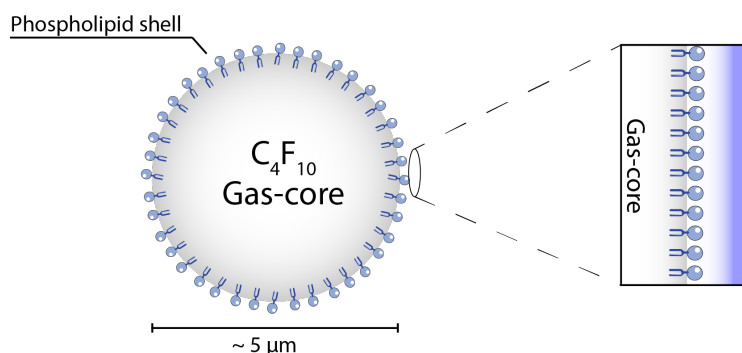


Figure 7. Schematic representation of an UCA containing a decafluorobutane (C_4F_{10}) gas-core stabilized by a phospholipid thin layer.

The first generation of UCA consisted of air bubbles stabilized by a proteic membrane based on the observations that the injection of air bubbles into the bloodstream enhanced the ultrasonic echo of the vasculature (Gramiak, Shah et al. 1969). Since then, inert gases with lower blood solubility and higher molecular weight substituted the air core; lipids or polymers provided more resistant shells, increasing the UCA half-life from seconds to the order of minutes in the bloodstream (Deelman, Declèves et al. 2010). The main microbubbles currently used and clinically approved are presented in Table 3, all are indicated for echocardiography and Doppler.

Table 3. UCA core and shell materials for echocardiography of distinct brands.

Brand	Core material	Shell component	Manufacturer
Sonovue [®]	Sulfur hexafluoride	Phospholipid	Bracco
Definity [®]	Octafluoropropane	Phospholipid	Bristol-Myers Squibb
Optison [®]	Octafluoropropane	Albumin	GE Healthcare
Levovist [®]	Air	Phospholipids/galactose	Schering

Apart from their use in diagnostic imaging, UCAs also present a limited potential to assimilate and carry drug-payloads. As UCA act as foci for local deposition of ultrasound energy, local drug release might be performed near target tissues and be greatly enhanced by sonoporation (Rychak and Klibanov 2014). However, the current generation of ACU lacks of functionalities and adequate compartments for drug encapsulation. Thereby, distinct work report attempts modify UCAs to overcome such difficulties and fully benefit from their theranostic potential. For example, Lentacker *et al.* 2009 have coupled a phospholipid-based UCA to liposomes loaded with doxorubicin for cumulative release in tumors (Lentacker, Geers *et al.* 2009). A more simple approach is described by Abdalkader *et al.* 2015 that have used anionic phospholipids for electrostatic intercalation with doxorubicin (Abdalkader, Kawakami *et al.* 2015). Conversely, the anchoring of negatively charged nucleic acids (e.g. cDNA and siRNA) is reported on positively charged UCA surfaces (Xie, Wu *et al.* 2016);

A distinct and more recent class of UCA comprises the stabilization of liquid perfluorocarbon cores by polymer shells (Figure 8) (Pisani, Fattal *et al.* 2008). The more resistant shell and lower PFC diffusion provides higher stability, longer lasting echogenicity (ability to backscatter ultrasound) and increased resistance to pressure and mechanical fluctuations compared to gaseous-core UCA (Pisani, Tsapis *et al.* 2006). Although the shell compressibility might be controlled according to polymeric layer thickness, the echoes arising from such capsules still remain lower than gas/phospholipid formulations, which hinder its diffused clinical use as ultrasonic contrast agents.

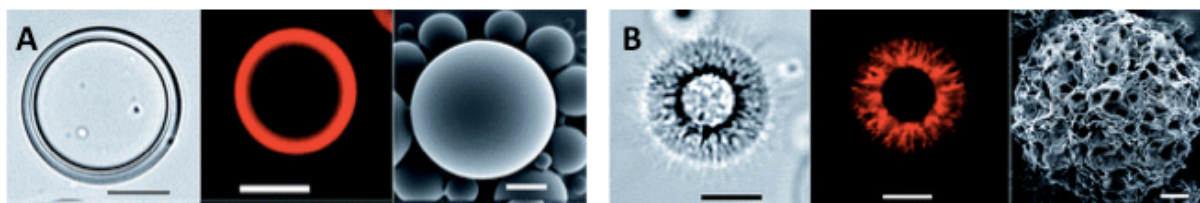


Figure 8. Sequence of bright field, confocal and SEM microscopic images of microcapsules containing a liquid perfluorooctyl bromide core and polymeric PLGA (A) and PLGA-*b*-PEG (B). Adapted from Pisani *et al.* 2009 (Pisani, Ringard *et al.* 2009).

Nevertheless, the use of liquid PFCs offers an important technological advantage for allowing a precise control over the size distribution, favoring the

formation of capsules at the nanoscale (Diou, Tsapis et al. 2012) – a condition hardly attained with gaseous PFC. In addition, the polymeric layer might be specially designed to target specific endogenous ligands, presenting interesting prospects in localized drug release and molecular imaging (Diaz-Lopez, Libong et al. 2008). The employment of PFCs with lower boiling points, such as perfluoropentane or perfluorohexane (29°C and 56°C, respectively) also presents many promises as theranostic agents in localized drug delivery driven by ultrasound (Mousnier, Huang et al. 2014). In addition, the PFC liquid core offers the possibility of tracking by ^{19}F magnetic resonance imaging (MRI) (Diou, Tsapis et al. 2012).

1.3.2.2 UCA acoustic response

The acoustic response of UCAs depends on the difference of acoustic impedances between the blood and the UCAs. The echogenicity also depends on UCA parameters: size, shell thickness, viscosity, concentration, and ultrasound frequency or applied power (Hernot and Klibanov 2008). For a single particle, comprising a diameter inferior than the incident wavelength, the total scattered intensity ($\sigma_d(\theta)$) – per unit of solid angle in the opposite direction of the incident beam – might be determined based on Equation 7 (Rayleigh 1947). As this model assumes an isotropic scattering, it evidences the influence of bigger particles to produce stronger echoes as well as the contribution arising from surface oscillation. This is the case for many nanometric liquid-core UCA, provided the diameter is below the ultrasound wavelength.

$$\sigma_d(\theta) = \frac{\kappa^4 r^6}{9} \left[\frac{k_v - k_0}{k_0} + \frac{3(\rho_v - \rho_0)}{2\rho_v + \rho_0} \cos\theta \right]^2, Eq. 7$$

where κ is the wavenumber, r is the radius, k_v is the particle compressibility, k_0 is the medium's compressibility, ρ_v is the particle density and ρ_0 is the medium's density.

Gaseous-core UCAs (also referred as microbubbles), however, produces comparatively stronger echoes than liquid containing materials. This effect is pronounced because of the gas higher compressibility, which undergo alternate contraction and expansion phases according to the passage of compressive and rarefractive ultrasonic pulses, thus, resonating within the megahertz range

frequencies utilized in clinical ultrasound (2-10 MHz). A symmetrical or “linear” size oscillation is observed for acoustic pressures values inferior of 0.05 MPa ($MI=0.04$) and the correspondent scattered signal is in the same frequency as the transmitted pulse (Figure 9) (Calliada, Campani et al. 1998). In this regime, the echogenicity of UCA is about a billion times higher than red blood cells, which present similar size as microbubbles, although exhibiting lower compressibility values (Powers and Kremkau 2011). Due to the more complex response to ultrasonic waves, these systems are modeled based on the Faran model or differential equations that describe the surrounding fluid compressibility (Anderson 2000).

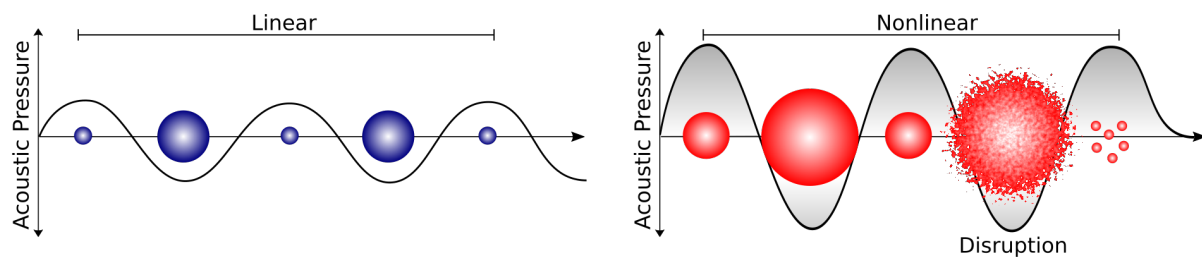


Figure 9. Size oscillation of gaseous-core ultrasound contrast agents in response to the applied acoustic intensity. UCAs submitted to low acoustic pressures resonate linearly according to the passage of compressive and rarefractive phases. High acoustic pressures provoke a nonlinear behavior that might lead to structural collapse or acoustic drop vaporization if liquid cores are employed.

The irradiation of higher acoustic pressures – 0.2 to 2 MPa ($MI=0.1$ to 1.4) – provokes a “nonlinear” size oscillation of such UCAs, which respond with more intense expansion and higher resistance to the compression ultrasonic phases (Cosgrove 2006). This behavior produces harmonics: signals at frequencies that are multiple of the fundamental frequency that are scattered and collected by the transducer. Although the harmonic frequencies present decreased intensity compared to main one, the second harmonic still displays enough energy to be explored in diagnostic imaging. It is, in fact, possible to discriminate the UCA signal from those arising from the tissue, thus, increasing the signal-to-noise ratio and reducing artifacts from surrounding anatomical structures (Calliada, Campani et al. 1998).

Increased acoustic pressures – normally higher than 2 MPa – causes violent UCA size oscillation and eventually leads to their disruption by inertial cavitation, depending on the shell mechanical properties (Postema, van Wamel et al.). This process increases the UCA backscattered signal due to a significant decrease in membrane damping after disruption and a passage to resonant size during dissolution of the gaseous component (Couture, Bannouf et al. 2009). Moreover, UCA cavitation generates microstreaming in the surrounding fluid and induces shear forces on nearby cell membranes, enhancing the vascular permeability to drugs (Frenkel 2008).

1.3.2.3 Harmonic Imaging

As previously introduced, the UCA nonlinear oscillation produces echoes that are not proportional to the incident pulse in amplitude, phase and frequency, which allow their harmonic signal to be distinguished from the fundamental frequency scattered by the tissues (Couture 2007). This characteristic is intensively investigated in echocardiography, tumor molecular imaging and assessment of angiogenesis biomarkers (Camarozano 2013, Yang, Cai et al. 2015) (Leguerney, Scoazec et al. 2015).

Nevertheless, tissues can also produce harmonics by a distinct mechanism of UCA oscillation: at high acoustic pressures, the sound speed is slightly higher than at ambient pressure and the high-pressure crest propagates faster than the low-pressure trough (Figure 10) (Anderson 2000). This behavior leads to peaking of the sound wave and the creation of harmonics (Powers and Kremkau 2011). Although the amount of harmonics generated in the tissue during the pulse propagation remains infinitesimal at the skin level, the cumulative harmonic intensity increases as it reaches deeper structures (Eckersley, Chin et al. 2005). For this reason, the second harmonic is intensively explored in ultrasound imaging for providing improved quality, reduce artifacts, distortions and reverberations, especially those generated by surface-related structures such as ribs and fat layers which only produce echoes in the fundamental frequency (Powers and Kremkau 2011).

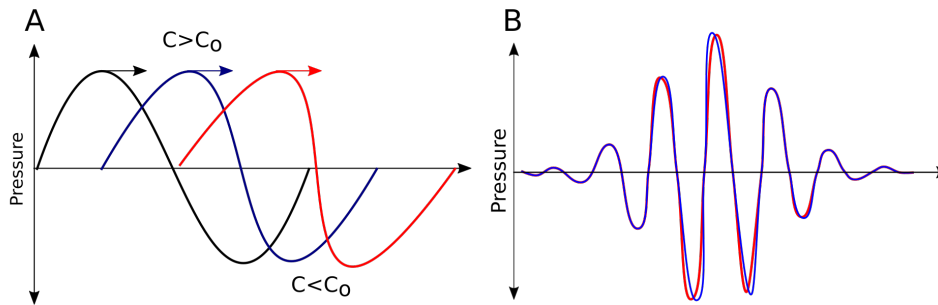


Figure 10. Tissue harmonic generation caused by the faster propagation of the wave's higher pressure portion and slower traveling velocity of the lower pressure portion due to the higher density of the medium (A). Distortion of the acoustic pulse during propagation within the tissue; the red line represents the pulse at 0 cm and the blue line at 10 cm (B). Images adapted from Powers *et al.* (Powers and Kremkau 2011) and Eckersley *et al.* (Eckersley, Tang et al. 2007).

The employment of UCA presents the advantage to provide ultrasound second harmonic imaging of superficial structures or deep organs. For UCA harmonic detection, special ultrasound set-ups to receive twice the emitted frequency and distinct pulse sequences, such as pulse inversion (PI) or amplitude modulation (AM) are employed to effectively segregate the signals from the tissue and permit specific UCA echo detection (Eckersley, Tang et al. 2007). The second harmonic imaging combined with UCA is extremely utilized in echocardiography to suppress artifacts produced during the cardiac muscle motion and also in the visualization of micron-sized vessels with slow blood flow, undetectable in conventional B-mode imaging (Camarozano 2013).

In the case of PI, two inversed ultrasonic pulses are separately transmitted, – both containing enough energy to cause nonlinear UCA oscillation – scattered and received by the transducer; the signals arising from the tissue are only at the fundamental frequency and are therefore cancelled once added. Only the harmonic frequencies emitted by the UCA are preserved, allowing segregation from tissue echoes.

A distinct approach for selective harmonic relies in amplitude modulation (AM), which involves the emission of two separately ultrasonic pulses with different intensities – only one provides enough energy to produce nonlinear UCA oscillation. The linear signals arising from tissue reflection are cancelled after amplification – by a factor equal to the ratio among the two emitted pulses – of the weaker echo

occasioned by lower MI and subtraction with the stronger echo. Nevertheless, the UCA echo generated by the higher MI pulse also possess harmonic frequencies, which are preserved after the subtraction of the fundamental frequencies (Eckersley, Tang et al. 2007).

The PI and AM methodologies might also be combined (PIAM), increasing the sensitivity of nonlinear UCA detection for lower MI to reduce disruption and clutter caused by nonlinear ultrasound propagation through the tissue. This approach transmits two pulses, in which one possess half the amplitude and is inverted relative to the other (Couture, Bannouf et al. 2009).

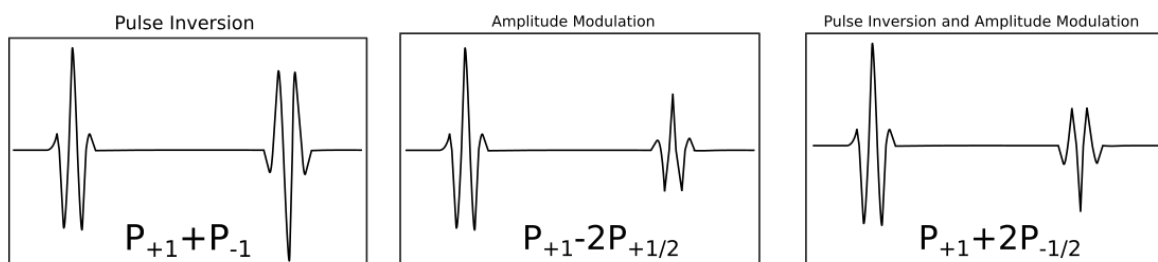


Figure 11. Pulse sequences utilized in harmonic imaging. Pulse inversion (left), Amplitude modulation (center) and Pulse inversion and amplitude modulation (right). Adapted from Eckersley *et al.* (Eckersley, Chin et al. 2005).

1.3.3 Therapeutic ultrasound

The clinical applicability of ultrasound is, however, not only restricted to diagnostic purposes. Distinct therapeutic modalities that utilizes acoustic intensities of several orders of magnitude greater than conventional diagnostic ultrasound are currently described and many are intensively clinically explored, such as stimulation of the immune response, brain blood barrier opening, tumor necrosis induction, hemostatic stimulation in surgical procedures, reduction of swelling and edema and also applications in lithotripsy as well as enhanced drug delivery (Kennedy 2005). Specifically, therapeutic ultrasound provides a precise spatial and temporal focalization of the transmitted thermal and mechanical energy, thus, stimulating only targeted tissues while maintaining the viability of adjacent healthy tissues (Duncanson, Arriaga et al. 2014).

In focused ultrasound (FUS), a transducer is positioned in contact with the skin over the targeted area and the acoustic energy is transmitted relative to the

focal volume. The sound beam is directed harmlessly across the skin and intervening tissues towards the target tumor to avoid any damage to anterior structures – the acoustic intensity is sufficiently low near the transducer. It's only at the beam focus that the energy level is great enough to cause a sufficient temperature increase for instantaneous cell death. These characteristics have generate a burst of minimally invasive treatments of several solid tumors, benign and malignant, including those of prostate, liver, breast, kidney, bone and pancreas (Kennedy 2005).

The ultrasound intensity might vary according to the desired therapeutic effect and the lesion depth; for example, intensities of 1 W/cm^2 during 10 minutes are normally employed in physical therapy to increase local blood flow and reduce edemas in connective tissue; conversely, tumor ablation therapies utilizes intensities higher than 1000 W/cm^2 for 1-3 seconds. Tumor treatment by ablation usually involves the creation of a discrete sequence of small lesion in the cancerous tissue to effectively induce the necrosis of large tumor volumes (Figure 12) (Bailey, Khokhlova et al. 2003). Additionally, the treatment might be applied more than once without increasing the risk of metastasis or serious side effects (Kennedy 2005).

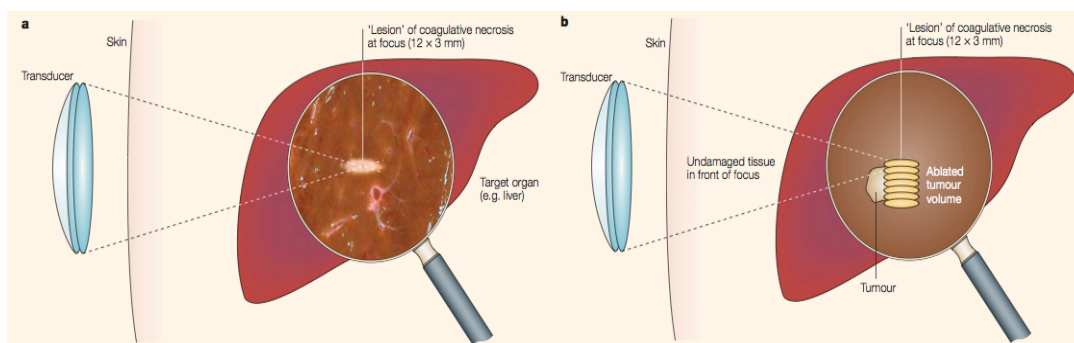


Figure 12. An extracorporeal ultrasonic beam is focused to the targeted tumor area in the liver (A). Schematic representation of sequential single lesions caused by focused ultrasound to achieve tumor ablation (B). Adapted from Kennedy *et al.* (Kennedy 2005).

The mechanism of tissue damage induced by FUS is due to a simultaneous conversion of mechanical energy into heat and also inertial cavitation. Increasing the local temperature above 56°C for at least 1 second is enough to promote cell death through coagulative necrosis. FUS generates local temperatures above 80°C for brief time periods (You, Wang et al. 2016). Tissues that possess higher ultrasound

absorption coefficients, such as bones, experience increased temperatures compared with those of low coefficients (e.g. muscles).

At high acoustic intensity, the waveform distortion causes a rapid absorption of higher harmonics, increasing the temperature at the focal area (Figure 13). This phenomenon may initiate the necrosis sooner than linear acoustic beams. If the derived nonlinear heating is significant, it may accelerate bubble formation and thus, induce tissue damage by inertial cavitation. In fact, bubbles are able to increase the temperature by several mechanisms: (i) the energy of bubble oscillation is damped due to viscosity and thermal conductivity, (ii) higher harmonics are scattered due to the nonlinear oscillatory behavior which leads to increased energy absorption by tissues, (iii) inertial collapse that creates shock waves, microjets and free radicals (Bailey, Khokhlova et al. 2003).

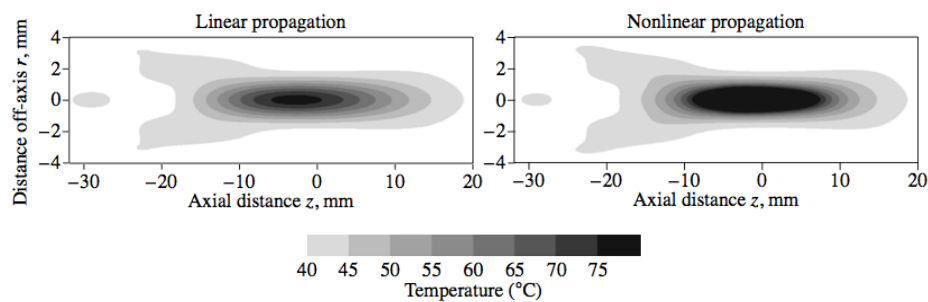


Figure 13. Numerical simulations of temperature elevation in linear and nonlinear acoustics. Adapted from Bailey *et al.* (Bailey, Khokhlova et al. 2003).

However, as ultrasound suffers attenuation during its course through tissues, the acoustic intensity is significantly reduced if the targeted area is localized in deep tissues (Boissenot 2015). As a result, the FUS efficiency to induce necrosis of deep-seated, large volume and abundant blood supplied tumors is lowered; by modifying ultrasonic parameters, such as power or duty cycle, undesired heating to intermediary tissues might occur and lead to unknown adverse events to normal tissue (Kennedy 2005). Nevertheless, FUS therapy might be synergistically enhanced by the use of intravascular micro or nano-sized drug-carriers (e.g. ultrasound contrast agents).

2. References

Abdalkader, R., S. Kawakami, J. Unga, R. Suzuki, K. Maruyama, F. Yamashita and M. Hashida (2015). "Evaluation of the potential of doxorubicin loaded microbubbles as a theranostic modality using a murine tumor model." Acta Biomaterialia **19**: 112-118.

Ahmadi, F., I. V. McLoughlin, S. Chauhan and G. ter-Haar (2012). "Bio-effects and safety of low-intensity, low-frequency ultrasonic exposure." Progress in Biophysics and Molecular Biology **108**(3): 119-138.

Ahmed, N., H. Fessi and A. Elaissari (2012). "Theranostic applications of nanoparticles in cancer." Drug Discovery Today **17**(17-18): 928-934.

Anderson, E. M. T., G. E. (2000). "A seminar on k-space applied to medical ultrasound." (1).

Bailey, M. R., V. A. Khokhlova, O. A. Sapozhnikov, S. G. Kargl and L. A. Crum (2003). "Physical mechanisms of the therapeutic effect of ultrasound (a review)." Acoustical Physics **49**(4): 369-388.

Bardhan, R., S. Lal, A. Joshi and N. J. Halas (2011). "Theranostic Nanoshells: From Probe Design to Imaging and Treatment of Cancer." Accounts of Chemical Research **44**(10): 936-946.

Bezagu, M., C. Errico, V. Chaulot-Talmon, F. Monti, M. Tanter, P. Tabeling, J. Cossy, S. Arseniyadis and O. Couture (2014). "High spatiotemporal control of spontaneous reactions using ultrasound-triggered composite droplets." J Am Chem Soc **136**(20): 7205-7208.

Boissenot, T. (2015). Ciblage de principes actifs par ultrasons en cancerologie, Paris Sud.

Boissenot, T., A. Bordat, E. Fattal and N. Tsapis (2016). "Ultrasound-triggered drug delivery for cancer treatment using drug delivery systems: From theoretical considerations to practical applications." Journal of Controlled Release **241**: 144-163.

Calliada, F., R. Campani, O. Bottinelli, A. Bozzini and M. G. Sommaruga (1998). "Ultrasound contrast agents: Basic principles." European Journal of Radiology **27**, **Supplement 2**: S157-S160.

Camarozano, A. C. W., L. H. (2013). Ecocardiografia de Estresse e Contraste, Revinter.

Choi, K. Y., H. Chung, K. H. Min, H. Y. Yoon, K. Kim, J. H. Park, I. C. Kwon and S. Y. Jeong (2010). "Self-assembled hyaluronic acid nanoparticles for active tumor targeting." Biomaterials **31**(1): 106-114.

Clark, A. J., D. T. Wiley, J. E. Zuckerman, P. Webster, J. Chao, J. Lin, Y. Yen and M. E. Davis (2016). "CRLX101 nanoparticles localize in human tumors and not in adjacent, nonneoplastic tissue after intravenous dosing." Proceedings of the National Academy of Sciences of the United States of America **113**(14): 3850-3854.

Cosgrove, D. (2006). "Ultrasound contrast agents: An overview." European Journal of Radiology **60**: 324-330.

Couture, O. (2007). Ultrasound echoes from targeted contrast agents, Toronto.

Couture, O., S. Bannouf, G. Montaldo, J.-F. Aubry, M. Fink and M. Tanter (2009). "Ultrafast Imaging of Ultrasound Contrast Agents." Ultrasound in Medicine & Biology **35**(11): 1908-1916.

Deelman, L. E., A. E. Declèves, J. J. Rychak and K. Sharma (2010). "Targeted renal therapies through microbubbles and ultrasound." Advanced Drug Delivery Reviews **62**: 1369-1377.

Dewey, W. C. (2009). "Arrhenius relationships from the molecule and cell to the clinic." Int J Hyperthermia **25**: 3-20.

Diaz-Lopez, R., D. Libong, N. Tsapis, E. Fattal and P. Chaminade (2008). "Quantification of pegylated phospholipids decorating polymeric microcapsules of perfluorooctyl bromide by reverse phase HPLC with a charged aerosol detector." J Pharm Biomed Anal **48**(3): 702-707.

Diaz-Lopez, R., N. Tsapis and E. Fattal (2010). "Liquid Perfluorocarbons as Contrast Agents for Ultrasonography and F-19-MRI." Pharmaceutical Research **27**(1): 1-16.

Ding, H. and F. Wu (2012). "Image guided biodistribution and pharmacokinetic studies of theranostics." Theranostics **2**(11): 1040-1053.

Diou, O., N. Tsapis, C. Giraudeau, J. Valette, C. Gueutin, F. Bourasset, S. Zanna, C. Vauthier and E. Fattal (2012). "Long-circulating perfluorooctyl bromide nanocapsules for tumor imaging by (fMRI)-F-19." Biomaterials **33**(22): 5593-5602.

Dozono, H., S. Yanazume, H. Nakamura, T. Etrych, P. Chytil, K. Ulbrich, J. Fang, T. Arimura, T. Douchi, H. Kobayashi, M. Ikoma and H. Maeda (2016). "HPMA Copolymer-Conjugated Pirarubicin in Multimodal Treatment of a Patient with Stage IV Prostate Cancer and Extensive Lung and Bone Metastases." Targeted Oncology **11**(1): 101-106.

Dube, D. H. and C. R. Bertozzi (2005). "Glycans in cancer and inflammation--potential for therapeutics and diagnostics." Nat Rev Drug Discov **4**(6): 477-488.

Duncanson, W. J., L. R. Arriaga, W. L. Ung, J. A. Kopechek, T. M. Porter and D. A. Weitz (2014). "Microfluidic Fabrication of Perfluorohexane-Shelled Double Emulsions for Controlled Loading and Acoustic-Triggered Release of Hydrophilic Agents." Langmuir **30**(46): 13765-13770.

Eckersley, R. J., C. T. Chin and P. N. Burns (2005). "Optimising phase and amplitude modulation schemes for imaging microbubble contrast agents at low acoustic power." Ultrasound in Medicine & Biology **31**(2): 213-219.

Eckersley, R. J., M.-X. Tang, K. Chetty and J. V. Hajnal (2007). "Microbubble Contrast Agent Detection Using Binary Coded Pulses." Ultrasound in Medicine & Biology **33**(11): 1787-1795.

Frenkel, V. (2008). "Ultrasound mediated delivery of drugs and genes to solid tumors." Adv Drug Deliv Rev **60**(10): 1193-1208.

Funkhouser, J. (2002). " Reintroducing pharma: Theranostic revolution." Curr. Drug Discovery **2**.

Gramiak, R., P. M. Shah and D. H. Kramer (1969). "Ultrasound cardiography: contrast studies in anatomy and function." Radiology **92**(5): 939-948.

Hernot, S. and A. L. Klibanov (2008). "Microbubbles in ultrasound-triggered drug and gene delivery." Advanced Drug Delivery Reviews **60**(10): 1153-1166.

Illing, R. O., J. E. Kennedy, F. Wu, G. R. ter Haar, A. S. Protheroe, P. J. Friend, F. V. Gleeson, D. W. Cranston, R. R. Phillips and M. R. Middleton (2005). "The safety and feasibility of extracorporeal high-intensity focused ultrasound (HIFU) for the treatment of liver and kidney tumours in a Western population." Br J Cancer **93**(8): 890-895.

Iyer, A. K., G. Khaled, J. Fang and H. Maeda (2006). "Exploiting the enhanced permeability and retention effect for tumor targeting." Drug Discovery Today **11**(17-18): 812-818.

Iyer, A. K., G. Khaled, J. Fang and H. Maeda (2006). "Exploiting the enhanced permeability and retention effect for tumor targeting." Drug Discov Today **11**(17-18): 812-818.

Jafari, S., O. Diou, J. Mamou, G. Renault, E. Fattal, N. Tsapis and S. L. Bridal (2014). "High-frequency (20 to 40 MHz) acoustic response of liquid-filled nanocapsules." IEEE Trans Ultrason Ferroelectr Freq Control **61**(1): 5-15.

Jeong, H.-S., H. Hwang, P.-S. Oh, E.-M. Kim, T. K. Lee, M. Kim, H. S. Kim, S. T. Lim, M.-H. Sohn and H.-J. Jeong (2016). "Effect of High-Intensity Focused Ultrasound on Drug Release from Doxorubicin-Loaded PEGylated Liposomes and Therapeutic Effect in Colorectal Cancer Murine Models." Ultrasound in Medicine & Biology **42**(4): 947-955.

Jeong, K., C. S. Kang, Y. Kim, Y.-D. Lee, I. C. Kwon and S. Kim (2016). "Development of highly efficient nanocarrier-mediated delivery approaches for cancer therapy." Cancer Letters **374**(1): 31-43.

Jo, S. D., S. H. Ku, Y. Y. Won, S. H. Kim and I. C. Kwon (2016). "Targeted Nanotheranostics for Future Personalized Medicine: Recent Progress in Cancer Therapy." Theranostics **6**(9): 1362-1377.

Kelkar, S. S. and T. M. Reineke (2011). "Theranostics: combining imaging and therapy." Bioconjug Chem **22**(10): 1879-1903.

Kennedy, J. E. (2005). "High-intensity focused ultrasound in the treatment of solid tumours." Nat Rev Cancer **5**(4): 321-327.

Kobayashi, H. and P. L. Choyke (2016). "Super enhanced permeability and retention (SUPR) effects in tumors following near infrared photoimmunotherapy." Nanoscale.

Kobayashi, H., K. Sano, T. Nakajima, K. Sato and P. L. Choyke (2014). "Photoimmunotherapy (PIT) combined with a nanosized cancer agent successfully treated heterogenous antigen-expressing tumors based on super-enhanced permeability and retention (SUPR) effect." Cancer Research **74**(19).

Lammers, T., S. Aime, W. E. Hennink, G. Storm and F. Kiessling (2011). "Theranostic Nanomedicine." Accounts of Chemical Research **44**(10): 1029-1038.

Leguerney, I., J.-Y. Scoazec, N. Gadot, N. Robin, F. Pénault-Llorca, S. Victorin and N. Lassau (2015). "Molecular Ultrasound Imaging Using Contrast Agents Targeting Endoglin, Vascular Endothelial Growth Factor Receptor 2 and Integrin." Ultrasound in Medicine & Biology **41**(1): 197-207.

Lentacker, I., I. De Cock, R. Deckers, S. C. De Smedt and C. T. W. Moonen (2014). "Understanding ultrasound induced sonoporation: Definitions and underlying mechanisms." Advanced Drug Delivery Reviews **72**: 49-64.

Lentacker, I., B. Geers, J. Demeester, S. C. De Smedt and N. N. Sanders (2009). "Design and Evaluation of Doxorubicin-containing Microbubbles for Ultrasound-triggered Doxorubicin Delivery: Cytotoxicity and Mechanisms Involved." Mol Ther **18**(1): 101-108.

Liang, X., J. Gao, L. Jiang, J. Luo, L. Jing, X. Li, Y. Jin and Z. Dai (2015). "Nanohybrid Liposomal Cerasomes with Good Physiological Stability and Rapid

Temperature Responsiveness for High Intensity Focused Ultrasound Triggered Local Chemotherapy of Cancer." ACS Nano **9**(2): 1280-1293.

Maeda, H. (2015). "Toward a full understanding of the EPR effect in primary and metastatic tumors as well as issues related to its heterogeneity." Advanced Drug Delivery Reviews **91**: 3-6.

Maeda, H., J. Wu, T. Sawa, Y. Matsumura and K. Hori (2000). "Tumor vascular permeability and the EPR effect in macromolecular therapeutics: a review." Journal of Controlled Release **65**(1-2): 271-284.

Matsumura, Y. and H. Maeda (1986). "A New Concept for Macromolecular Therapeutics in Cancer Chemotherapy: Mechanism of Tumoritropic Accumulation of Proteins and the Antitumor Agent Smancs." Cancer Research **46**(12 Part 1): 6387-6392.

Mitragotri, S. (2005). "Healing sound: the use of ultrasound in drug delivery and other therapeutic applications." Nat Rev Drug Discov **4**(3): 255-260.

Mousnier, L., N. Huang, E. Morvan, E. Fattal and N. Tsapis (2014). "Influence of polymer end-chemistry on the morphology of perfluorohexane polymeric microcapsules intended as ultrasound contrast agents." Int J Pharm **471**(1-2): 10-17.

Mura, S. and P. Couvreur (2012). "Nanotheranostics for personalized medicine." Adv Drug Deliv Rev **64**(13): 1394-1416.

Orellana, C. (2003). "Global action against cancer." Lancet Oncology **4**(7): 389-389.

Otto, C. (2000). Principles of echocardiographic image acquisition and Doppler analysis. Textbook of Clinical Ecocardiography., WB Saunders.

Pisani, E., E. Fattal, J. Paris, C. Ringard, V. Rosilio and N. Tsapis (2008). "Surfactant dependent morphology of polymeric capsules of perfluorooctyl bromide: influence of polymer adsorption at the dichloromethane-water interface." J Colloid Interface Sci **326**(1): 66-71.

Pisani, E., C. Ringard, V. Nicolas, E. Raphael, V. Rosilio, L. Moine, E. Fattal and N. Tsapis (2009). "Tuning microcapsules surface morphology using blends of homo- and copolymers of PLGA and PLGA-PEG." Soft Matter **5**(16): 3054-3060.

Pisani, E., N. Tsapis, J. Paris, V. Nicolas, L. Cattel and E. Fattal (2006). "Polymeric nano/microcapsules of liquid perfluorocarbons for ultrasonic imaging: physical characterization." Langmuir **22**(9): 4397-4402.

Postema, M., A. van Wamel, C. T. Lancée and N. de Jong "Ultrasound-induced encapsulated microbubble phenomena." Ultrasound in Medicine and Biology **30**(6): 827-840.

Powers, J. and F. Kremkau (2011). "Medical ultrasound systems." Interface Focus **1**(4): 477-489.

Raisinghani, A., P. Rafter, P. Phillips, M. A. Vannan and A. N. DeMaria (2004). "Microbubble contrast agents for echocardiography: rationale, composition, ultrasound interactions, and safety." Cardiol Clin **22**: 171-180.

Rayleigh (1947). "Luminous phenomena in oxygen." Nature **159**(4049): 777.

Rychak, J. J. and A. L. Klibanov (2014). "Nucleic acid delivery with microbubbles and ultrasound." Advanced Drug Delivery Reviews **72**: 82-93.

Sharma, S. (2014). "Nanotheranostics in evidence based personalized medicine." Curr Drug Targets **15**(10): 915-930.

Shung, K. (2015). "Diagnostic Ultrasound: Imaging and Blood Flow Measurements." **2**.

Strebhardt, K. and A. Ullrich (2008). "Paul Ehrlich's magic bullet concept: 100 years of progress." Nat Rev Cancer **8**(6): 473-480.

Tennant, D. A., R. V. Duran and E. Gottlieb (2010). "Targeting metabolic transformation for cancer therapy." Nature Reviews Cancer **10**(4): 267-277.

van de Ven, A. L., P. Kim, O. H. Haley, J. R. Fakhoury, G. Adriani, J. Schmulen, P. Moloney, F. Hussain, M. Ferrari, X. Liu, S.-H. Yun and P. Decuzzi (2012). "Rapid tumorotropic accumulation of systemically injected platelet particles and their biodistribution." Journal of Controlled Release **158**(1): 148-155.

Xie, A., M. D. Wu, G. Cigarroa, J. T. Belcik, A. Ammi, F. Moccetti and J. R. Lindner (2016). "Influence of DNA-Microbubble Coupling on Contrast Ultrasound-Mediated Gene Transfection in Muscle and Liver." Journal of the American Society of Echocardiography **29**(8): 812-818.

Yang, H., W. Cai, L. Xu, X. Lv, Y. Qiao, P. Li, H. Wu, Y. Yang, L. Zhang and Y. Duan (2015). "Nanobubble-Affibody: Novel ultrasound contrast agents for targeted molecular ultrasound imaging of tumor." Biomaterials **37**: 279-288.

You, Y. F., Z. G. Wang, H. T. Ran, Y. Y. Zheng, D. Wang, J. S. Xu, Z. B. Wang, Y. Chen and P. Li (2016). "Nanoparticle-enhanced synergistic HIFU ablation and transarterial chemoembolization for efficient cancer therapy." Nanoscale **8**(7): 4324-4339.

Zhang, K., H. Chen, F. Li, Q. Wang, S. Zheng, H. Xu, M. Ma, X. Jia, Y. Chen, J. Mou, X. Wang and J. Shi (2014). "A continuous tri-phase transition effect for HIFU-mediated intravenous drug delivery." Biomaterials **35**(22): 5875-5885.

Zhang, K., P. Li, H. Chen, X. Bo, X. Li and H. Xu (2016). "Continuous Cavitation Designed for Enhancing Radiofrequency Ablation via a Special Radiofrequency Solidoid Vaporization Process." ACS Nano **10**(2): 2549-2558.

Zheng, S., Z. Jin, J. Han, S. Cho, V. D. Nguyen, S. Y. Ko, J.-O. Park and S. Park (2016). "Preparation of HIFU-triggered tumor-targeted hyaluronic acid micelles for controlled drug release and enhanced cellular uptake." Colloids and Surfaces B: Biointerfaces **143**: 27-36.

Objectives

Theranostic systems especially designed to perform multi-modal imaging and release encapsulated payloads in response to external stimuli present an unparalleled potential to increase the current chemotherapy effectiveness. Therefore, the goal of this thesis is to develop theranostic micro and nano-sized agents based on gaseous and liquid perfluorocarbon cores sensitive to ultrasonic pulses for imaging and solid tumor therapy. Distinct approaches for system construction and technical difficulties will be described in the different sections of this thesis.

In the third chapter, the interfacial coating of gaseous-core microvesicles by chitosan is described (Figure 1.1). The biopolymer is employed as a suitable platform for anchoring of therapeutic agents, such as DNA or siRNA, which might be more effectively transfected into cells during ultrasound-induced sonoporation. This section describes the system assembly, exploring the interactive effect of phospholipids and chitosan by surface sensitive techniques and highlights the polysaccharide potential to reduce the fast diffusibility of the gas component, a common drawback of UCAs.

The fourth and fifth chapters are devoted to the development and structural investigation of nano and microcapsules containing a liquid perfluorocarbon core. In these two sections, the synthesis and employment of end-group fluorinated polylactide polymers is described with the intent to increase the fluorine-fluorine interaction of shell and core components (Figure 1.2). As the nanocapsules are able to passively target tumor tissues by the EPR effect, the acoustic response is thoroughly investigated as well as the effects generated by distinct lengths of the fluorinated group.

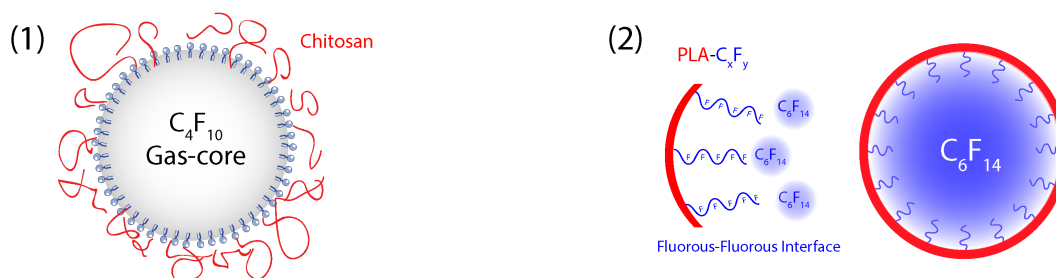


Figure 1. Schematic illustration of microvesicles coated with chitosan (1) and fluorinated polymeric capsules (2) developed in this thesis.

Chapter 2

Gaseous-core microvesicles coated with chitosan

The polysaccharide chitosan is successfully utilized as intravascular vector for proteins or nucleic acids (DNA and siRNA) for its ability in stabilizing charged active molecules. Also, many studies have shown that chitosan-decorated liposomes presented reduced flocculation and decreased toxic effects caused by phospholipids. Hence, we have explored chitosan's characteristics to improve the stability of perfluorocarbon gas-core microvesicles and generate microvesicles with theranostic potential. The conceived system presents the ability of responding to ultrasonic pulses, acting as real-time imaging contrast agents. Once insonified with higher acoustic pressures, entrapped nucleic acids or drugs might be released from the chitosan layer, profiting from cavitation and jet-streams to increase its permeability into cells.

The system design was based on the interactivity of chitosan and the phospholipid DSPC as assessed by surface sensitive techniques – FTIR, QCM, AFM and SFE. Initially, an irreversible adhesion between the polymer and the phospholipid was observed. This system was then translated into microvesicles containing a gas-core of decafluorobutane. The presence of chitosan coating was verified by fluorescence microscopy, employing FITC-labeled chitosan. Further results display the biopolymer's effectiveness in modifying the DSPC phase transition event, also reducing the rate of decafluorobutane diffusibility compared to plain samples. Finally, the ultrasonic response showed a persistent *in vitro* acoustic response. As a result, the design, assemble and characterization of a potential theranostic candidate is reported.

Chitosan-coated microvesicles: effect of polysaccharide-phospholipid affinity on decafluorobutane dissolution

Carbohydrate Polymers 153 (2016) 169-175

Guilherme F. Picheth^{a,b}, Cleverton L. Pirich^a, Larissa A. dos Santos^a, Ana C. Camarozano^c,

Maria Rita Sierakowski^a, Fernanda M. Ocampos^d, Andersson Barison^d, Gabriel A.

Kaminski^{a,b}, Roberto Pontarolo^b, Rilton Alves de Freitas^{a*}

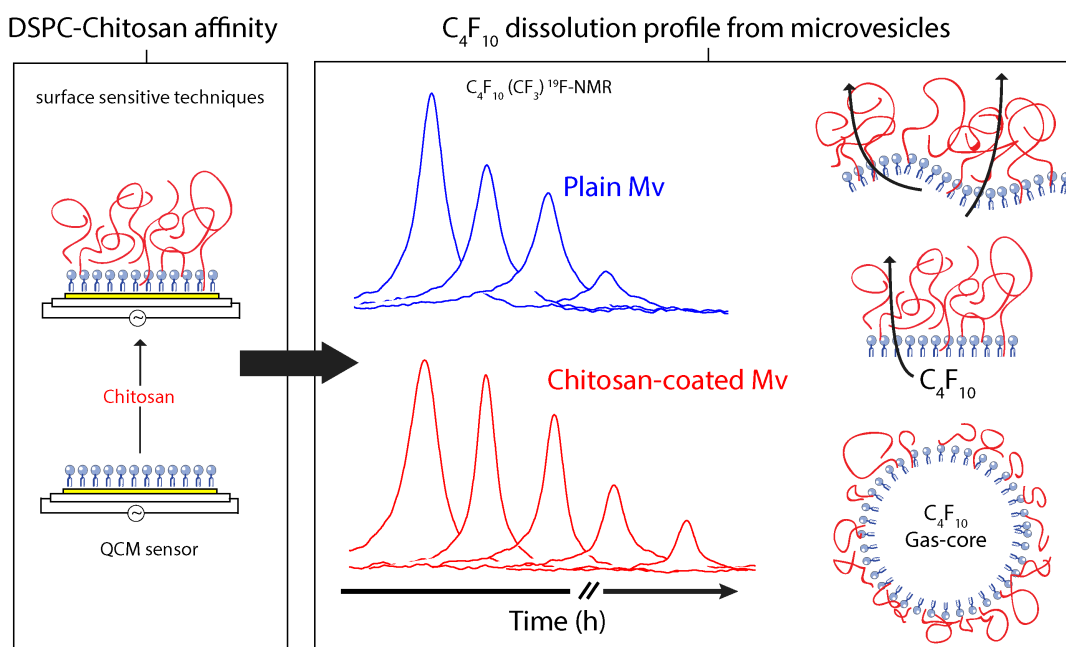
^a Biopol, Chemistry Department, Federal University of Paraná, 81531-980. Curitiba, PR, Brazil.

^b CEB, Pharmacy Department, Federal University of Paraná, 80210-170. Curitiba, PR, Brazil.

^c Medicine Department, Federal University of Paraná, 80060-240. Curitiba, PR, Brazil.

^d NMR center, Federal University of Paraná, 81531-980. Curitiba, PR, Brazil.

Graphical Abstract



Keywords

Chitosan, microvesicles, decafluorobutane, phospholipids, ultrasound

Abstract

The stability of perfluorinated microvesicles is mainly determined by the presence of interfacial materials and their ability to hinder the gas component diffusibility into the bloodstream. The goal of this study is to increase the persistence of the gaseous-core by introducing chitosan-coated 1,2-distearoyl-sn-glycero-3-phosphocholine (DSPC) microvesicles, reducing gas diffusion from microvesicles, and increasing for a long time ultrasonic signals. Our hypothesis was based on the irreversible adhesion of chitosan towards DSPC head groups observed in thin-films models. This affinity enhanced the stabilization of gaseous-core microvesicles, in which the polysaccharide effectively reduced the phospholipid phase transition enthalpy from $383 \pm 5.5 \text{ J.mg}^{-1}$ for plain to $150 \pm 9.7 \text{ J.mg}^{-1}$ for chitosan-coated microvesicles, providing a more stable structure that diminished the gaseous component lost and provided the persistence of intense ^{19}F -NMR signals after 48 h, twice as long compared to plain samples. As a result, stronger and long-lasting ultrasonic signals were produced by the more stable chitosan-containing microvesicles, thus, presenting great potential to increase the diagnostic and therapeutic applications of perfluorocarbon carries.

1. Introduction

Lipid-coated microvesicles containing a perfluorocarbon gas core are widely employed as ultrasound contrast agents (UCA) in clinical imaging and targeted-release systems of therapeutic agents (Ferrara, Borden et al. 2009) (Abdalkader, Kawakami et al. 2015). Although UCA utilization is recommended in several cardiology assays, the current gas-filled microvesicles generation exhibits low gas permeation resistance and short circulation lifetime (Wilson and Burns 2010, Garg, Thomas et al. 2013). These limitations are mainly determined by the interactions performed by the shell components that must overcome perturbations and hinder the dissolution of the gaseous core into the bloodstream (Kwan and Borden 2012).

The improvement of UCA shell resistance by the association of biopolymers with phospholipids presents great prospects; such strategy allows the formation of a composite interface, adding the structural integrity of polymeric backbones to the amphiphilic character of lipids, thereby forming a shell with the potential to prolong the gaseous core diffusion (Cheow and Hadinoto 2011). In particular, anchored or adsorbed biopolymers on lipid-derived UCA often cause the increase of surface rigidity and resistance to external stresses (Ratanabanangkoon, Gropper et al. 2003).

Recently, biopolymers gained attention for effectiveness in lipid stabilization for their ability to interact electrostatically, as well as hydrophobically, reducing flocculation and toxic effects caused by phospholipids (Manca, Sinico et al. 2012); (Manca, Sinico et al. 2012). Cationic phospholipids are related to induce a series of toxic effects as evaluated *in vivo* and *in vitro*, such as complement activation, cytotoxicity towards macrophages and DNA damage in distinct tissues (Filion and Phillips 1997) (Knudsen, Northeved et al. 2015). However, cellular destabilization may also occur due to transfer of cationic lipids from the liposome into the plasma membrane (Soenen, Brisson et al. 2009). Among the different biopolymers, chitosan is a linear polysaccharide composed of β -N-acetyl-D-glucosamine and β -D-glucosamine units bonded (1 \rightarrow 4) which is extensively utilized as a pharmaceutical excipient due to its biocompatibility, biodegradability and ability to increase the circulation half-life of several pharmaceutical formulations (Baldrick 2010); (Sheng, Liu et al. 2009).

Although polyethylene glycol (PEG) functionalized-lipids, commonly utilized in UCA, reduces particle aggregation and opsonization (Owens and Peppas 2006), they are unable to act as a strong barrier to avoid gas dissolution for long periods of time (Borden and Longo 2002). Therefore, the length of the phospholipid acyl chain and the low diffusibility of the gas in aqueous media are the main responsible to maintain the microvesicles and the gaseous component stability. However, rapid gas diffusion is observed *in vitro* and *in vivo*, which hinders its imaging performance and clinical use. In this work, we report the impact of chitosan to interact with 1,2-distearoyl-sn-glycero-3-phosphocholine (DSPC) and enhance the UCA shell resistance against the decafluorobutane gas dissolution. The use of chitosan is based on its potential to reduce lipid relaxation (e.g. lateral diffusion) (Baumgart and Offenhausser 2003) and therefore, maintain a stiff structure that diminishes phospholipid instabilities, such as buckling and folding mechanisms over time (Lozano and Longo 2009); (Garg, Thomas et al. 2013).

Here, we present a detailed description of DSPC-chitosan affinity by simulated bidimensional models thoroughly analyzed by infrared, quartz crystal microbalance, tensiometry and atomic force microscopy. A comparative study of plain and chitosan coated microvesicles was performed by microcalorimetry and the gas dissolution was quantified using ^{19}F -NMR analysis. The *in vitro* ultrasonic response is also presented for both systems.

2. Materials and methods

2.1 Chemicals

Chitosan was obtained from Purifarma (São Paulo, Brazil). Hexanethiol, diiodomethane, chloroform, Fluorescein isothiocyanate, deuterated water, glycerol, propylene glycol, acetic acid, trifluoroacetic acid and hydrochloridric acid were obtained from Sigma Chemical Co. (Missouri, USA). Sulfuric acid and hydrogen peroxide were purchased from Dinâmica (São Paulo, Brazil). Agarose was purchased from Pronadisa (Madrid, Spain). Ultrapure water was obtained from MilliQ system and the cellulose ester filtration membranes of 0.45 μm from Millipore (Massachusetts, USA). 1,2-distearoyl-sn-glycero-3-phosphocholine (DSPC) was obtained from Lipoid (Ludwigshafen, Germany) and the decafluorobutane gas was purchased from Synquest Laboratories (Florida, USA).

Chitosan was previously purified as described by Recillas *et al.* (2009) and solubilized in 0.5 mol.L⁻¹ acetic acid (1 mg.mL⁻¹) (Rinaudo 2006). The deacetylation degree of chitosan was 82 wt.%, weight-average molar-mass (M_w) of 87.8×10^3 g.mol⁻¹ and ζ -potential of $+26.8 \pm 3.1$ mV at pH 3. The polymer characterisation was performed as published elsewhere (Picheth, Sierakowski *et al.* 2014).

2.2 Quartz Crystal Microbalance (QCM)

The interaction between the chitosan and DSPC was assessed by quartz crystal microbalance (QCM) (SRS, Stanford Research Systems, Sunnyvale, USA) using the static cell mode. At-cut gold QCM (Ti/Cr 5 MHz SRS) crystal sensors were previously cleaned by immersion in a H₂O₂: H₂SO₄ (1:3 v/v) solution for 5 minutes and rinsed with ultrapure water. The QCM sensors were modified with hexanethiol (Morita, Nukui *et al.* 2006) and then 100 $\mu\text{g.mL}^{-1}$ DSPC was deposited as previously described (Kaminski, Sierakowski *et al.* 2016). The modified crystals were then immersed in chitosan solution (1 mg.mL⁻¹ pH 3) for 10 minutes and subsequently washed with ultrapure water. All experiments were performed in triplicate.

2.3 Infrared Spectroscopy

Infrared spectra (IR) were recorded using the QCM gold crystals as substrates for sample deposition on a Bruker Vertex 70 spectrometer (Bruker Co., Billerica, USA) equipped with an attenuated total reflection (ATR) probe. All IR spectra were obtained from by averaging 16 scans with a resolution of 4 cm^{-1} in the range of $4000\text{-}400\text{ cm}^{-1}$.

2.4 Atomic Force Microscopy

Atomic force microscopy (AFM) from samples deposited onto QCM gold quartz crystals were obtained in air using an Agilent microscope (Agilent Technologies, Santa Clara, USA) and analysed by Pico Image software (Agilent Technologies, Santa Clara, USA). Tapping mode images were obtained with Vistaprobes[®] (Nanoscience Instruments, Inc., Phoenix, USA) silicon tips (nominal spring constant of 48 N/m and resonance frequency of $\sim 180\text{ kHz}$) by scanning an area of $4.0\text{ }\mu\text{m} \times 4.0\text{ }\mu\text{m}$.

2.5 Contact Angle Analysis

Contact angle (CA) analyses (DataPhysics OCA 15 Plus tensiometer, Filderstadt, Germany) were performed on surfaces deposited onto QCM gold crystals using the sessile drop method on a DataPhysics OCA 15 Plus tensiometer. All measurements were obtained at 25°C using a $500\text{ }\mu\text{L}$ Hamilton syringe (Bonaduz, Switzerland) with the delivery of $1\text{ }\mu\text{L}$ ultrapure water and diiodomethane ($>99.5\%$) drops onto the QCM crystal-coated surface. The CA determinations were performed with SCA 20 DataPhysics software (Filderstadt, Germany). Each CA value was the average of at least 3 drops of liquid per surface. The surface free energy (SFE) and its components (polar and dispersive) were calculated by the Owens and Wendt equation (Eq. 1 and 2) (Rotta, Ozorio et al. 2009):

$$\gamma_S^{Tot} = \gamma_S^d + \gamma_S^p, \quad Eq.1$$

$$\gamma_L(1 + \cos \theta) = 2 \left(\sqrt{\gamma_S^d \gamma_L^d} + \sqrt{\gamma_S^p \gamma_L^p} \right), \quad Eq.2$$

where θ is the contact angle, γ_L is the surface tension of the liquid, segregated in dispersive and polar contributions (γ_L^d and γ_L^p) (Fan and Lee 2008), γ_S^{Tot} , γ_S^d and γ_S^p are the total surface tension, dispersive and polar components for the solid, respectively.

2.6 Microvesicles preparation

The microvesicles containing chitosan were prepared by the reverse phase- evaporation method as described by Mertins et al. (2005) with modifications. Briefly, 20 mg of DSPC were transferred to a 50 mL round bottom flask and dissolved in 9 mL of chloroform solution containing 1 mL of methanol and 500 μL of chitosan (1 $\text{mg}\cdot\text{mL}^{-1}$) solution. The mixed-system was sonicated in a probe disruptor (Sonics Vibra Cell SM0220, Misonix, New York, USA) with 30% amplitude for 15 s in an ice bath. The solvent was eliminated under reduced pressure at 30°C, yielding a viscous organogel. Afterwards, the solution was hydrated with 10 mL of phosphate buffer saline (0.1 $\text{mol}\cdot\text{L}^{-1}$, pH 7.4) containing 10% v/v of glycerol and propylene glycol – with the intent to reduce the microvesicle’s floatation velocity (Kaya, Gregory V et al. 2009) – at 80°C, temperature higher than DSPC phase transition temperature (~60°C), ensuring a homogeneous phospholipid hydration, with constant stirring for 1 h (Castangia, Manca et al. 2013) (Manca, Zaru et al. 2013). The mixture was then submitted to 3 cycles of sonication of 30 s with 30% amplitude. Next, the decafluorobutane gas was incorporated through a three-way valve mixture system and the solution was sonicated at the liquid-gas interface with 40% amplitude for 10 s in an ice bath.

2.7 Fluorescence Microscopy

For fluorescence microscopy experiments, chitosan was conjugated with fluorescein isothiocyanate (FITC) (Quemeneur, Rammal et al. 2007). Briefly, 500 mg of purified chitosan was dissolved in 50 mL of HCl (0.1 $\text{mol}\cdot\text{L}^{-1}$). Next, 12.5 mL of FITC solution (1 $\text{mg}\cdot\text{mL}^{-1}$) in methanol was added and stirred for 3h at room temperature. The solution was neutralized with NaOH (1 $\text{mol}\cdot\text{L}^{-1}$), centrifuged for 10 minutes at 1300 x g and washed with ethanol 70% v/v. The product was dried in a 40°C oven protect from light for 2 days.

The microvesicles containing FITC-labeled chitosan were formulated under light protection and observed in an Olympus BX4TF fluorescence microscope. All samples were excited at 495 nm and visualized at 519 nm.

2.8 Differential Scanning Calorimetry

Differential Scanning Calorimeter (DSC) experiments were performed on a Setaram Micro DSC III (Setaram, France) microcalorimeter under 10 bar flow of nitrogen atmosphere using 1 cm³ vessels from 20 to 100 °C with a heating and cooling rate of 0.5°C.min⁻¹. The data were collected with the Setsoft 2000 software and all results are represented as the second heating-cooling ramp (thermal history). Microvesicles solution (800 µL) prepared with and without chitosan coating were submitted to analysis.

2.9 Decafluorobutane quantification – ¹⁹F-NMR

The decafluorobutane dissolution from the microvesicles was followed by ¹⁹F Nuclear Magnetic Resonance (NMR). All spectra were acquired in D₂O at 310 K on a Bruker AVANCE III NMR spectrometer operating at 9.4 Tesla, observing ¹⁹F at 376.45 MHz, equipped with a 5-mm multinuclear inverse detection probe. For this, the X-channel from pre-amplifier was connected to the hydrogen channel on the probe and was tuned to ¹⁹F frequency, once it is closest to the hydrogen NMR frequency than to the other X-channel nuclei frequencies. The spectra were acquired with 90° pulse excitation, 64K data points, recycle delay of 1 s, averaging 32 scans on a spectral width of 86.24 ppm. All the chemical shifts are given in ppm related to TFA as external reference. The samples were stored at 25°C in a capless vial, homogenised and 500 µL were transferred to a 5-mm NMR tube for evaluation. All analyses were conducted in triplicate.

2.10 In vitro Ultrasound

Gel phantoms were produced according to Böhmer et al. (2010). Briefly, ultrapure water was heated to 70 °C and 10% *wt.* of agarose D-1 Medium EEO (Pronadisa, Madrid, Spain) was added under slow stirring. The system was maintained under vacuum for 1h and left at 4 °C during 18h to cool down. A total of 500 µL of microvesicles was added to each well before imaging. The phantoms were placed over an acoustic absorber support. Imaging was performed by a commercially available ultrasound system (GE Healthcare, USA) equipped with a 1.5-3.1 MHz transducer (Vivid 7 Dimension, GE Healthcare, USA). All images were obtained in B-mode with a low persistence and mechanical index (MI) of 0.1.

3. Results and Discussion

3.1 Phospholipid-chitosan interaction

The process of microvesicle assemble was based in a multi-step method (Mertins, Schneider et al. 2010) to allow chitosan association with the phospholipid layer. The process occurred by (i) formation of a water-in-oil like emulsion in acidic pH, (ii) solvent evaporation, resulting in a reversed micelle organogel, (iii) hydration with PBS buffer pH 7.4 and (iv) decafluorobutane incorporation to generate microvesicles.

Initially (steps *i* and *ii*), a system comprising an acidic pH is characterized by a positively charged chitosan –pka of 6.5 (Domard 1987) – which contributes to disrupt the phospholipid organization in the organic solvent (Fresta, Ricci et al. 2000) and allows the polysaccharide accommodation into pre-formed DSPC layers (Pavinatto, Pavinatto et al. 2013). After the formation of the DSPC-chitosan complex, the organogel was resuspended in PBS pH 7.4 and the microvesicles with decafluorobutane were formed by sonication (steps *iii* to *iv*). To confirm an efficient DSPC – chitosan interaction during the formation of microvesicles, thin films of the phospholipid were deposited on top of At-cut gold QCM crystals previously coated with hexanethiol, thus, simulating the available interface for polysaccharide adsorption. Four distinct surface-sensitive techniques were employed to assess an effective chitosan deposition: IR, QCM, AFM and SFE. The exact same crystal was analyzed by all techniques after the deposition and rinsing of each layer corresponding to the system interface.

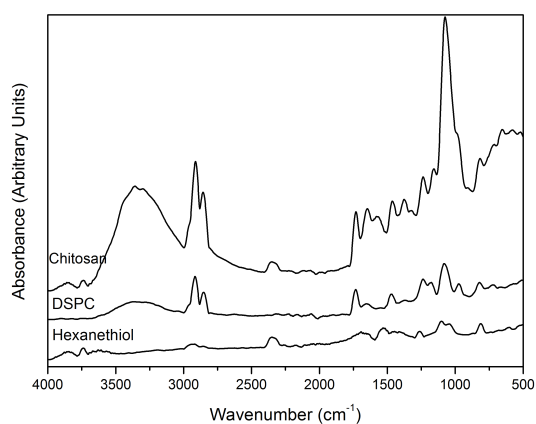


Figure 1. IR spectra for QCM crystals subsequently coated with hexanethiol, DSPC and chitosan.

An ordered and interfacial DSPC head group orientation was provided by a previously deposited layer of hexanethiol (Meuse, Niaura et al. 1998). The IR spectra revealed the hexanethiol coverage over the crystal surface (**Figure 1**) by the presence of symmetric and asymmetric bands correspondent to $-\text{CH}_2-$ stretching frequencies at 2853 cm^{-1} and 2929 cm^{-1} , respectively (Holmberg and Korgel 2010). As expected, low SFE values (**Table 1**), mainly from the dispersive contribution were disclosed, indicating that the hydrophobic segments were ordered to the interface.

The DSPC IR spectra revealed intensity bands at 2848 cm^{-1} and 2908 cm^{-1} (CH_2 stretching) as well as at 1734 cm^{-1} and 1240 cm^{-1} for $\text{C}=\text{O}$ and PO_2 groups, respectively (Sahin, Bilge et al. 2013). The phospholipid polar group orientation was verified by the increase at SFE values and the polar component of the surface. Such results confirmed the availability of DSPC polar groups on the air-interface.

After chitosan deposition, the IR spectra revealed bands at 3293 cm^{-1} (O-H and N-H stretch), 1645 cm^{-1} (amide I), 1575 cm^{-1} (N-H bending for amine and amide II respectively) and the skeletal vibration of C-O stretch at 2050 cm^{-1} that demonstrate the polysaccharide deposition onto DSPC. Moreover, the chitosan-coated surfaces exhibited similar SFE values to the previous layer, also dominated by the polar contribution, which imply that the DSPC head groups still contribute to increase the interfacial free energy.

Table 1: Contact angle (θ) and SFE values (γ_s^{Tot}) segregated into dispersive (γ_s^d) and polar (γ_s^p) components for crystals covered with hexanethiol, DSPC and chitosan.

Sample	θ ($^\circ$)		$\text{mJ}\cdot\text{m}^{-2}$		
	H_2O	CH_2I_2	γ_s^{Tot}	γ_s^d	γ_s^p
Hexanethiol	77.8 ± 4.1	68.1 ± 3.2	29.4 ± 2.1	17.4 ± 0.5	12 ± 2.0
DSPC	18.4 ± 2.0	65.4 ± 1.6	69.7 ± 1.7	11.2 ± 1.7	58 ± 1.5
Chitosan	32.4 ± 4.4	77.6 ± 3.5	64.3 ± 2.0	6.95 ± 1.2	57 ± 3.0

where θ indicate the contact angle in degrees.

γ_s^{Tot} , γ_s^d and γ_s^p represents the total surface tension, dispersive and polar components for the samples, respectively.

The system assembly and DSPC-chitosan interaction was also followed by AFM that initially exhibited homogeneous deposited hexanethiol layers onto the crystals surface as shown in **Figure 2**. After DSPC deposition, the images revealed

irregular surfaces containing nodular structures that demonstrate an effective and disorganized phospholipid coating.

Phase contrast images exhibited a shift of the phase angle from $1.2 \pm 1.0^\circ$ for DSPC films to $9.0 \pm 0.5^\circ$ after chitosan adsorption. As the phase AFM images offer a measurement of the surface composition – in the case of non-uniform samples (Scott & Bhushan, 2003) – its profile reflects a contrast of the viscous energy dissipation across the surface. Therefore, once chitosan is adsorbed onto DSPC, the increased phase angle shift is related to an augmented local viscoelasticity and/or difference composition (Silva, Sierakowski et al. 2016) – in agreement with QCM frequency shift of -105 ± 15 Hz caused by chitosan. Polymer deposition was also accompanied by an increased roughness that confirmed an effective chitosan adsorption; these results are in agreement with Zaru et al. (2009) that observed irreversible chitosan adherence to DSPC-formed liposomes.

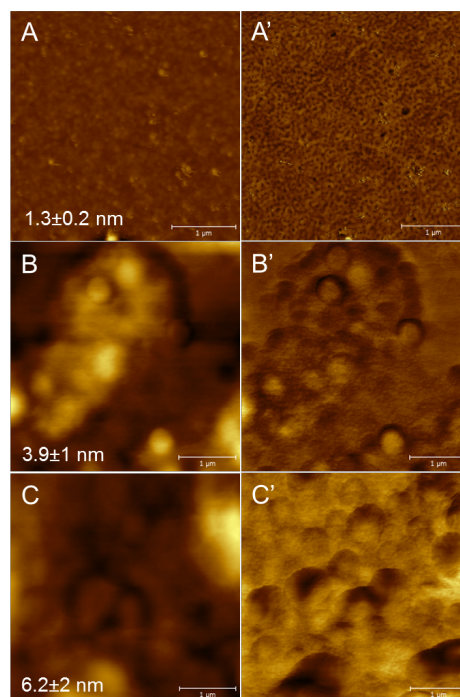


Figure 2. AFM $4 \times 4 \mu\text{m}$ topography (A-C) and phase images (A'-C') for hexanethiol (A/A'), DSPC (B/B') and DSPC coated with chitosan (C/C'). The surface mean roughness is indicated for each topography image.

3.2 *In vitro* stability of microvesicles

After confirming the affinity of chitosan and DSPC in simulated bidimensional models, the impact of the composite shell on the behavior of microvesicles containing decafluorobutane was evaluated. Initially, fluorescence microscopy images verified the presence of FITC-labeled chitosan effectively coating the phospholipid layer as shown in **Figure 3**. All samples presented an effective diameter inferior to 10 μm , thus, potentially able to circulate through the microvasculature. Plain and chitosan-coated samples were designated as Mv and MvC, respectively.

A DSC study of Mv and MvC samples showed a single endothermic event at $54.1 \pm 0.2^\circ\text{C}$ during the heating cycle, corresponding to the phospholipid gel to liquid crystalline transition (**Figure 3**) (Sahin, Bilge et al. 2013). However, the transition enthalpy decreases substantially with the presence of chitosan: from $383.9 \pm 5.5 \text{ kJ}\cdot\text{mol}^{-1}$ for Mv to $150 \pm 9.7 \text{ kJ}\cdot\text{mol}^{-1}$ for MvC due to reduction of the number of DSPC molecules undergoing phase transition. Similar results were obtained by Fang et al. (2001) that reported diminished DPPC cohesive interactions with increasing chitosan molar fractions; and also by Mertins et al. (2009) that evidenced the increased energy requirement to phosphatidylcholine liposomes containing chitosan to overcome the phase-transition. This 2.9 fold reduction in the surfactant chain melting enthalpy also indicates that the unmelted chains might be interacting with chitosan acetyl groups' backbones, demonstrating that the polysaccharide was effectively introduced into the DSPC layer. The chitosan M_w might also enhance the hydrophobic interactions between both materials due to its low steric hindrance that allows the polymer to accommodate into the DSPC chains as discussed by Pavinatto et al. (2013) by DMPC model monolayers. The presence of chitosan in an intercalated configuration with the DSPC membrane might reduce phospholipid overlapping as well as diminish the attractive forces between the phospholipid hydrophobic regions, thereby, preventing decafluorobutane loss.

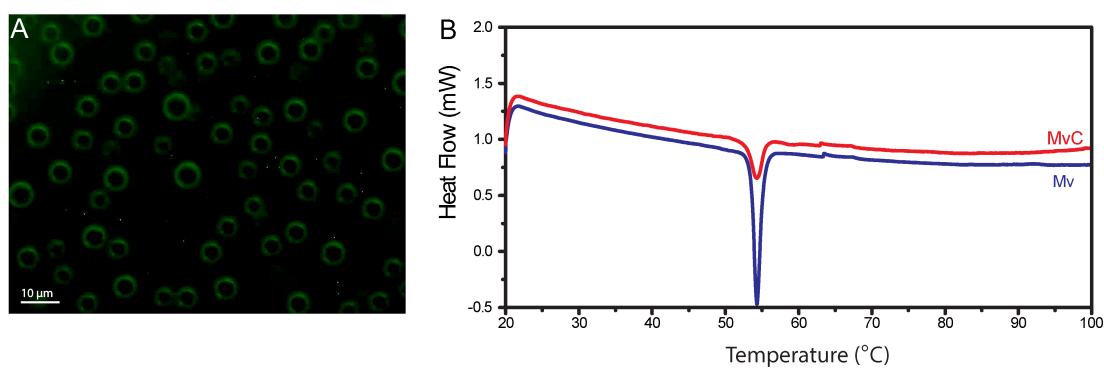


Figure 3. Fluorescence microscopy image of FITC-labeled chitosan coated microvesicles (A) and DSC heating curve for chitosan-containing microvesicles (red line) and plain microvesicles (blue line) (B).

The gas-core dissolution profile was followed along the time by ^{19}F NMR; all C_4F_{10} spectra showed two signals, at -85.7 and -131.13 ppm, assigned to CF_3 and CF_2 , respectively, according to Rodriguez-Rojo et al. (2013). Concentrated solutions of plain and chitosan-coated microvesicles were prepared and stored at room temperature in capless vials; independent $500\ \mu\text{L}$ aliquots were withdrawn at specific time intervals, diluted in D_2O and analyzed at 37°C to mimic *in vivo* temperature. The relative content of C_4F_{10} was calculated in respect to the CF_3 resonance integral.

Initially, a fast C_4F_{10} diffusion process was observed for both samples, highlighting the lack of efficiency of both interfaces to maintain high gaseous contents for prolonged periods (**Figure 4**) - this effect is mainly related to a decreased interactivity of the shell components, generating gaps along the gas-liquid interface that allow C_4F_{10} efflux, oxygen influx and a consequent size growth (Borden and Longo 2002) (Dalvi and Joshi 2015).

A significant reduction of decafluorobutane diffusion rate was observed after 2h, in which the samples containing chitosan displayed higher C_4F_{10} contents: $52\pm 0.5\%$ for Mv and $63\pm 0.2\%$ for MvC at 2h. The subsequent decay profile exhibited higher amounts of fluorinated gas in all analyzed time intervals for MvC, persisting until 48h in which the ^{19}F signals were still present in the NMR spectra only for microvesicles coated with the biopolymer, suggesting that the distinct architectural DSPC packing induced by chitosan offered more resistant interfaces against C_4F_{10} dissolution. These results indicate that the intercalated disposal of chitosan-DSPC

maintained more rigid and cohesive phospholipid organizations along the time and prevented surface deformations by DSPC overlapping.

In general, the presence of chitosan hindered the formation of a gas-liquid interface and, ultimately, provided a reduction on microvesicles gas permeability. Although the impact of chitosan in the resultant surface tension and Laplace pressure towards the decafluorobutane core as well as shell elasticity behavior in gaseous environments still need to be elucidated, this new composite interface was effective in reducing the C_4F_{10} dissolution dynamics compared to a commonly employed phospholipid shell. Similar composite monolayers of phospholipid mixture intercalated with doxorubicin were also effective in reducing perfluoropropane (C_3F_8) lost along the time, with dependency on drug rate incorporation into the shell (Abdalkader, Kawakami et al. 2015).

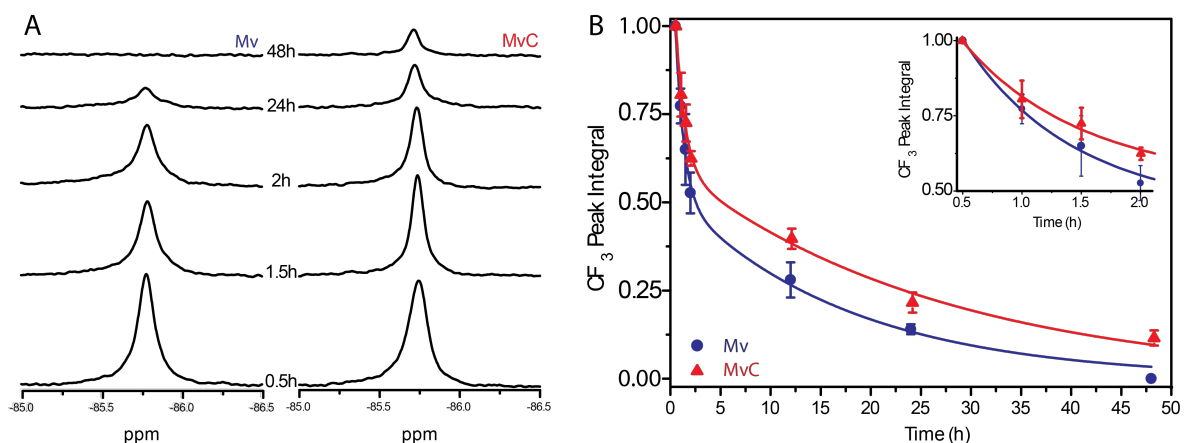


Figure 4. ^{19}F NMR spectra showing CF_3 resonance of C_4F_{10} at distinct time intervals for plain (Mv) and chitosan-coated microvesicles (MvC) (A); comparison of CF_3 peak integrals along the time (B).

The influence of chitosan in the microvesicle's acoustic response was evaluated by *in vitro* agarose phantoms with a standard clinical scanner and ultrasonic imaging conditions – B-mode and MI=0.1. An effective response was visualized for all samples after 0.5h of C_4F_{10} inclusion under insonification as shown in **Figure 5**.

Ultrapure water was employed as control group and exhibited any significant signals. The signal-to-noise ratio (SNR) was analyzed in distinct time intervals after sample preparation. At 0.5h both samples presented a SNR of 35 ± 5.0 dB, however,

after 24h the intensity decreased to 20 ± 2.0 dB for Mv and 30 ± 1.0 dB for MvC, thus, confirming the reduced gas-core content found by ^{19}F NMR assays. As a result, the presence of chitosan allowed an efficient shell compressibility and elasticity, also preserving the acoustic response for prolonged periods compared to DSPC microvesicles.

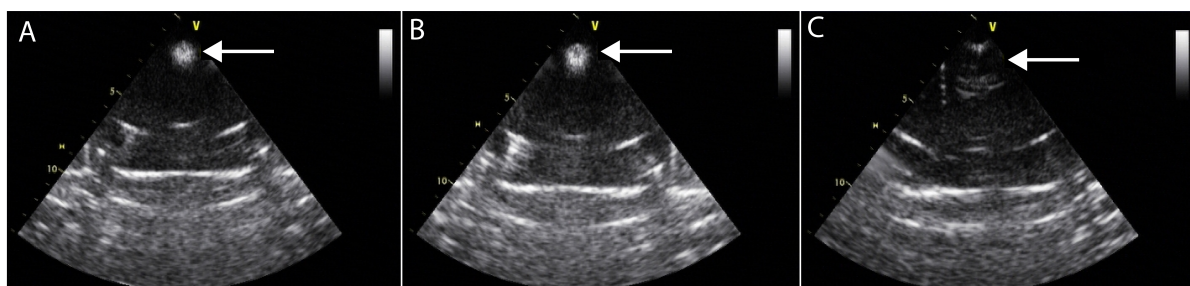


Figure 5. B-mode ultrasound images of freshly prepared plain (A) and chitosan-coated (B) microvesicles compared to ultrapure water as negative control (C). The correspondent region of interest for all samples is indicated by the white arrow.

4. Conclusion

An effective affinity was observed between DSPC and chitosan in simulated bidimensional thin film models. Such interactivity was translated into chitosan-coated microvesicles entrapping a gaseous C_4F_{10} core, reducing the phospholipid phase-transition and suggesting a more stable configuration formed by a DSPC layer intercalated with polymeric domains. Chitosan-coated microvesicles effectively reduced the gaseous component lost and exhibited intense signals after 48 hours, twice as long compared to uncoated samples; in addition, the ultrasonic response maintained intense signals for prolonged periods, thus, exhibiting the potential of the composite interface to increase the circulation persistence into the bloodstream and also enhance the shelf stability of C_4F_{10} microvesicles.

5. Acknowledgements

The authors are grateful to CAPES, CNPq, Finep, Fundação Araucária, Rede Nanobiotec and UFPR for financial support and fellowships. We are also grateful to Mr. César Baron for all of his contributions to this work.

6. References

Abdalkader, R., Kawakami, S., Unga, J., Suzuki, R., Maruyama, K., Yamashita, F., & Hashida, M. (2015). Evaluation of the potential of doxorubicin loaded microbubbles as a theranostic modality using a murine tumor model. *Acta Biomaterialia*, 19, 112-118.

Baldrick, P. (2010). The safety of chitosan as a pharmaceutical excipient. *Regulatory Toxicology and Pharmacology*, 56(3), 290-299.

Baumgart, T., & Offenhausser, A. (2003). Polysaccharide-supported planar bilayer lipid model membranes. *Langmuir*, 19(5), 1730-1737.

Borden, M. A., & Longo, M. L. (2002). Dissolution behavior of lipid monolayer-coated, air-filled microbubbles: Effect of lipid hydrophobic chain length. *Langmuir*, 18(24), 9225-9233.

Castangia, I., Manca, M. L., Matricardi, P., Sinico, C., Lampis, S., Fernández-Busquets, X., Fadda, A. M., & Manconi, M. (2013). Effect of diclofenac and glycol intercalation on structural assembly of phospholipid lamellar vesicles. *International Journal of Pharmaceutics*, 456(1), 1-9.

Cheow, W. S., & Hadinoto, K. (2011). Factors affecting drug encapsulation and stability of lipid-polymer hybrid nanoparticles. *Colloids and Surfaces B-Biointerfaces*, 85(2), 214-220.

Dalvi, S. V., & Joshi, J. R. (2015). Modeling of microbubble dissolution in aqueous medium. *Journal of Colloid and Interface Science*, 437, 259-269.

Domard, A. (1987). Ph and Cd Measurements on a Fully Deacetylated Chitosan - Application to Cu-li-Polymer Interactions. *International Journal of Biological Macromolecules*, 9(2), 98-104.

Fan, C. W., & Lee, S. C. (2008). Effects in surface free energy of sputter-deposited NbN_x films. *Materials Chemistry and Physics*, 107(2-3), 334-338.

Ferrara, K. W., Borden, M. A., & Zhang, H. (2009). Lipid-Shelled Vehicles: Engineering for Ultrasound Molecular Imaging and Drug Delivery. *Accounts of Chemical Research*, 42(7), 881-892.

Filion, M. C., & Phillips, N. C. (1997). Toxicity and immunomodulatory activity of liposomal vectors formulated with cationic lipids toward immune effector cells. *Biochimica et Biophysica Acta (BBA) - Biomembranes*, 1329(2), 345-356.

Fresta, M., Ricci, M., Rossi, C., Furneri, P. M., & Puglisi, G. (2000). Antimicrobial nonapeptide leucinostatin A-dependent effects on the physical properties of phospholipid model membranes. *Journal of Colloid and Interface Science*, *226*(2), 222-230.

Garg, S., Thomas, A. A., & Borden, M. A. (2013). The effect of lipid monolayer in-plane rigidity on in vivo microbubble circulation persistence. *Biomaterials*, *34*(28), 6862-6870.

Holmberg, V. C., & Korgel, B. A. (2010). Corrosion Resistance of Thiol- and Alkene-Passivated Germanium Nanowires. *Chemistry of Materials*, *22*(12), 3698-3703.

Kaminski, G. A. T., Sierakowski, M. R., Pontarolo, R., Santos, L. A. d., & Freitas, R. A. d. (2016). Layer-by-layer polysaccharide-coated liposomes for sustained delivery of epidermal growth factor. *Carbohydrate Polymers*, *140*, 129-135.

Kaya, M., Gregory V, T. S., & Dayton, P. A. (2009). Changes in Lipid-Encapsulated Microbubble Population During Continuous Infusion and Methods to Maintain Consistency. *Ultrasound in Medicine & Biology*, *35*(10), 1748-1755.

Knudsen, K. B., Northeved, H., Kumar Ek, P., Permin, A., Gjetting, T., Andresen, T. L., Larsen, S., Wegener, K. M., Lykkesfeldt, J., Jantzen, K., Loft, S., Møller, P., & Roursgaard, M. (2015). In vivo toxicity of cationic micelles and liposomes. *Nanomedicine: Nanotechnology, Biology and Medicine*, *11*(2), 467-477.

Kwan, J. J., & Borden, M. A. (2012). Lipid monolayer dilatational mechanics during microbubble gas exchange (vol 8, pg 4756, 2012). *Soft Matter*, *8*(48), 12144-12144.

Lozano, M. M., & Longo, M. L. (2009). Complex formation and other phase transformations mapped in saturated phosphatidylcholine/DSPE-PEG2000 monolayers. *Soft Matter*, *5*(9), 1822-1834.

Manca, M. L., Sinico, C., Maccioni, A. M., Diez, O., Fadda, A. M., & Manconi, M. (2012). Composition influence on pulmonary delivery of rifampicin liposomes. *Pharmaceutics*, *4*(4), 590-606.

Manca, M. L., Zaru, M., Manconi, M., Lai, F., Valenti, D., Sinico, C., & Fadda, A. M. (2013). Glycosomes: A new tool for effective dermal and transdermal drug delivery. *International Journal of Pharmaceutics*, *455*(1-2), 66-74.

Mertins, O., Schneider, P. H., Pohlmann, A. R., & da Silveira, N. P. (2010). Interaction between phospholipids bilayer and chitosan in liposomes investigated by ³¹P NMR spectroscopy. *Colloids Surf B Biointerfaces*, *75*(1), 294-299.

Meuse, C. W., Niaura, G., Lewis, M. L., & Plant, A. L. (1998). Assessing the molecular structure of alkanethiol monolayers in hybrid bilayer membranes with vibrational spectroscopies. *Langmuir*, *14*(7), 1604-1611.

Morita, S., Nukui, M., & Kuboi, R. (2006). Immobilization of liposomes onto quartz crystal microbalance to detect interaction between liposomes and proteins. *J Colloid Interface Sci*, 298(2), 672-678.

Owens, D. E., & Peppas, N. A. (2006). Opsonization, biodistribution, and pharmacokinetics of polymeric nanoparticles. *International Journal of Pharmaceutics*, 307(1), 93-102.

Pavinatto, A., Pavinatto, F. J., Deleuzuk, J. A. D., Nobre, T. M., Souza, A. L., Campana-Filho, S. P., & Oliveira, O. N. (2013). Low molecular-weight chitosans are stronger biomembrane model perturbants. *Colloids and Surfaces B-Biointerfaces*, 104, 48-53.

Picheth, G. F., Sierakowski, M. R., Woehl, M. A., Ono, L., Cofre, A. R., Vanin, L. P., Pontarolo, R., & De Freitas, R. A. (2014). Lysozyme-triggered epidermal growth factor release from bacterial cellulose membranes controlled by smart nanostructured films. *J Pharm Sci*, 103(12), 3958-3965.

Quemeneur, F., Rammal, A., Rinaudo, M., & Pepin-Donat, B. (2007). Large and giant vesicles "Decorated" with chitosan: Effects of pH, salt or glucose stress, and surface adhesion. *Biomacromolecules*, 8(8), 2512-2519.

Ratanabanangkoon, P., Gropper, M., Merkel, R., Sackmann, E., & Gast, A. P. (2003). Mechanics of streptavidin-coated giant lipid bilayer vesicles: A micropipet study. *Langmuir*, 19(4), 1054-1062.

Rinaudo, M. (2006). Chitin and chitosan: Properties and applications. *Progress in Polymer Science*, 31(7), 603-632.

Rotta, J., Ozorio, R. A., Kehrwald, A. M., Barra, G. M. D., Amboni, R. D. D. C., & Barreto, P. L. M. (2009). Parameters of color, transparency, water solubility, wettability and surface free energy of chitosan/hydroxypropylmethylcellulose (HPMC) films plasticized with sorbitol. *Materials Science & Engineering C-Biomimetic and Supramolecular Systems*, 29(2), 619-623.

Sahin, I., Bilge, D., Kazanci, N., & Severcan, F. (2013). Concentration-dependent effect of melatonin on DSPC membrane. *Journal of Molecular Structure*, 1052, 183-188.

Sheng, Y., Liu, C. S., Yuan, Y., Tao, X. Y., Yang, F., Shan, X. Q., Zhou, H. J., & Xu, F. (2009). Long-circulating polymeric nanoparticles bearing a combinatorial coating of PEG and water-soluble chitosan. *Biomaterials*, 30(12), 2340-2348.

Silva, R. d., Sierakowski, M. R., Bassani, H. P., Zawadzki, S. F., Pirich, C. L., Ono, L., & de Freitas, R. A. (2016). Hydrophilicity improvement of mercerized bacterial cellulose films by polyethylene glycol graft. *International Journal of Biological Macromolecules*, 86, 599-605.

Soenen, S. J. H., Brisson, A. R., & De Cuyper, M. (2009). Addressing the problem of cationic lipid-mediated toxicity: The magnetoliposome model. *Biomaterials*, 30(22), 3691-3701.

Wilson, S. R., & Burns, P. N. (2010). Microbubble-enhanced US in Body Imaging: What Role? *Radiology*, 257(1), 24-39.

Chapter 3

Synthesis of fluorinated polymers for nanocapsule formulation

Although the gaseous-core microvesicles functionalized with chitosan display an interesting theranostic potential, its size range impairs passive accumulation by the EPR effect since they are too large to permeate into the tumor fenestrated vasculature. Therefore, the second section of this thesis is dedicated to the development of theranostic materials at the nanoscale, able to passively target solid tumors. The system design was based on the entrapment of a liquid perfluorocarbon, perfluorohexane (PFH), which presents a low boiling point and vapor pressure (56°C and 29 kPa) and, thus, act as a sensitive probe to mechanical and pressure variations of ultrasonic pulses. Ultimately, the irradiation of intense acoustics pressures might vaporize the perfluorocarbon core and release co-stabilized therapeutic agents only at the ultrasound focal point.

However, the fluorophilic character of fully fluorinated liquids imparts optimal encapsulation rates of PFH into biocompatible polymers, phospholipids or tensoactives shells. As a result, drug-release triggered by the acoustic vaporization of perfluorocarbons is limited by the poor wettability of fluorinated interfaces within hydrophobic or hydrophilic stabilizing materials. The fluorous – fluorous interaction of PFH and polymer shells is therefore explored in this section with the intent to increase the molecular recognition of the fluorinated liquid to provide enhanced ultrasonic sensitivity (Figure 1). In this study, the impact of PFH encapsulation into nanocapsules formulated with PLA presenting distinct lengths of linear fluorinated chains (PLA-C₃F₇, C₆F₁₃, C₈F₁₇, C₁₁F₂₃ and C₁₃F₂₇) is compared to a non-fluorinated polymer (PLA-C₆H₁₃). Distinct parameters such as morphology, cytotoxicity and acoustic response are investigated.

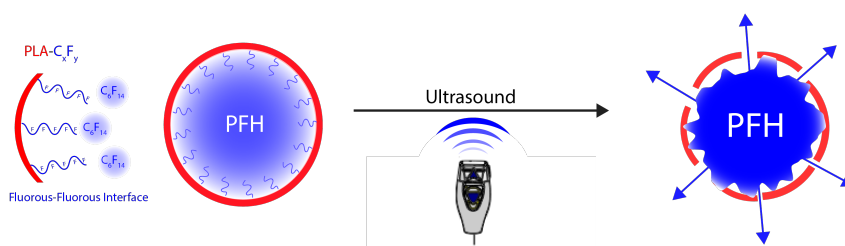


Figure 1. Schematic representation of the nanocapsules formulated with fluorinated polymers before and after the exposure to ultrasound.

End-group fluorination of polylactide enhances the echogenicity of nanocapsules

Guilherme Picheth^{a,d}, Sophie Houvenagel^a, Camille Dejean^b, Olivier Couture^c, Rilton Freitas^d, Laurence Moine^a, Nicolas Tsapis^{a*}

^a Institut Galien Paris-Sud, CNRS, Univ. Paris-Sud, Université Paris-Saclay, 92296 Châtenay-Malabry, France.

^b BioCIS, CNRS, Univ. Paris-Sud, Université Paris-Saclay, 92296 Châtenay-Malabry, France.

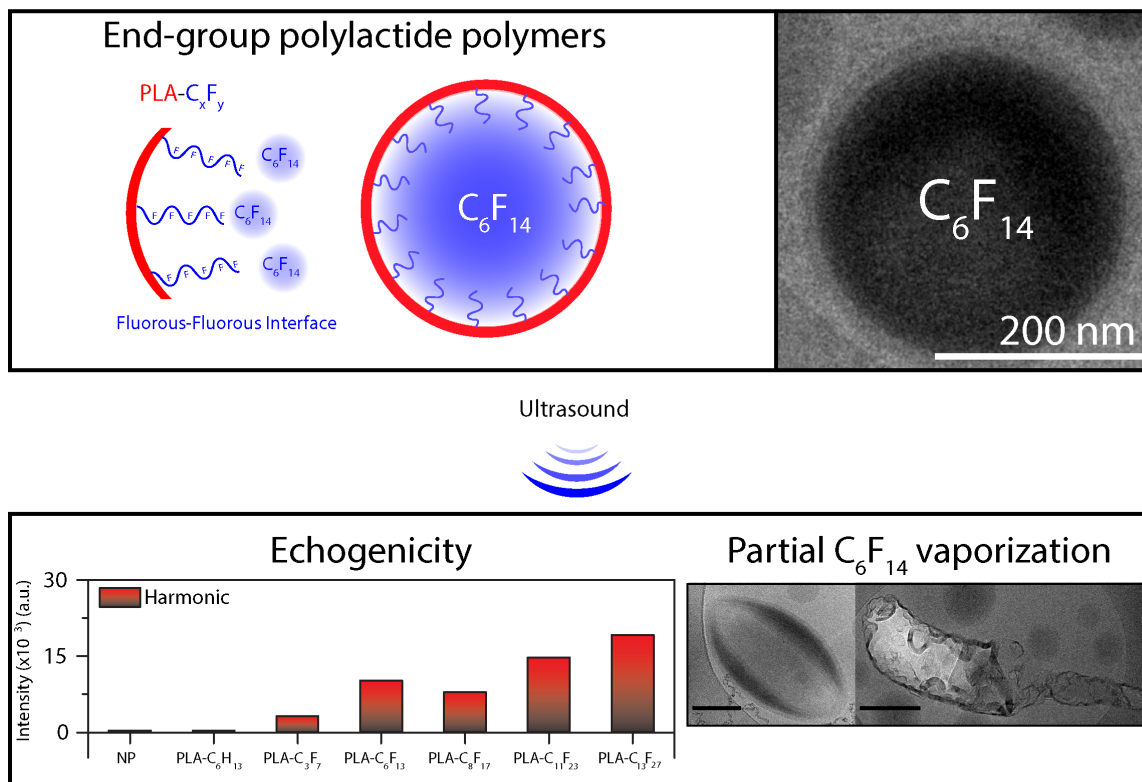
^c Institut Langevin, ESPCI Paris, CNRS (UMR 7587), INSERM (U979), Paris, France

^d Biopol, Chemistry Department, Federal University of Paraná, 81531-980. Curitiba, PR, Brazil.

* Corresponding author at: Institut Galien Paris-Sud, CNRS, Univ. Paris-Sud, Université Paris-Saclay, 92296 Châtenay-Malabry, France Tel.: +33 146835813. E-mail address: nicolas.tsapis@u-psud.fr (Nicolas Tsapis).

Keywords: Nanocapsules, perfluorohexane, fluorinated polymers, ultrasound imaging, focused ultrasound, fluororous interaction

Graphical abstract



Abstract

End-group fluorinated polylactide (PLA) polymers were synthesized and employed to improve the encapsulation of perfluorohexane (PFH) into nanocapsules. PLA polymers containing five distinct lengths of fluorinated (from C₃F₇ to C₁₃F₂₇) and non-fluorinated (C₆H₁₃) end-groups were synthesized by ring-opening polymerization of D,L-lactide. Cryo-Transmission Electron Microscopy confirmed PFH entrapment as core of spherical 150 nm nanocapsules and ¹⁹F nuclear magnetic resonance revealed that those formulated with fluorinated polymers increased two-fold the encapsulation efficiency of PFH compared with non-fluorinated derivatives. The echogenicity produced by the fluorinated-shelled nanocapsules was 10-fold higher than those formulated with non-fluorinated polymers or nanoparticles devoid of a perfluorocarbon core for both fundamental and harmonic ultrasound imaging modalities. In addition, acoustic drop vaporization of PFH was successfully attained by focused ultrasound as observed by fragmented or disrupted morphologies in many samples. Altogether, our results demonstrate the potential of end-group fluorinated PLA to enhance the entrapment of PFH and increase the acoustic sensitivity of nanocapsules to ultrasound.

1. Introduction

Ultrasound contrast agents (UCAs) are efficient intravascular echo-enhancers currently indispensable to safe and accurate diagnosis of many diseases, including kidney cysts (Chang, Chong et al. 2016), acute myocardial ischemia (Kaul and Ito 2004) and solid tumors (Emilio, Fabrizio et al. 2004). All the commercially available UCAs, such as Definity[®] and Sonovue[®], are microbubbles constituted by a perfluorinated gaseous-core stabilized by a monolayer of phospholipids (Borden, Martinez et al. 2006). Unfortunately, the imaging and therapeutic applications of such materials are severely limited by (1) their inherent micrometer size range that prevents extravasation into solid tumors, (2) the fast-diffusing gas component, responsible for a relatively short half-life in the bloodstream (~60s) (Dalvi and Joshi 2015) and (3) the difficulty to load high drug doses into microbubbles (Geers, Lentacker et al. 2011).

To overcome these limitations, research has focused on nanosystems that can be more stable, loaded with maximized drug contents and are able to diffuse beyond the vascular compartment. Since nanobubbles are difficult to stabilize, the strategy has consisted in encapsulating liquid perfluorocarbons (PFCs) (Cosco, Fattal et al. 2015). Although interesting, this approach leads to a strong reduction of the echogenicity of such UCAs arising from size reduction and the replacement of the gas core by a liquid one. To provide strong and long-lasting ultrasonic echoes, liquid PFCs of high vapor pressure, such as perfluorohexane (PFH) or perfluoropentane, have been selected for their ability to experience a liquid-to-gas transition once exposed to high acoustic pressures (Duncanson, Arriaga et al. 2014). During this phenomenon – known as acoustic drop vaporization (ADV) – the PFC vapor phase may be stabilized by a polymeric shell of poly(lactide-co-glycolide) (PLGA) or poly(lactide) (PLA) and undergo oscillations around an equilibrium radius, which enhances the ultrasound scattering intensity of nanometric systems by several orders of magnitude (Guédra and Coulouvrat 2015) (Rapoport, Nam et al. 2011).

As previously reported, PFC-containing nanocapsules can preserve their integrity and initial diameter after intravenous administration and passively accumulate in tumor tissues through the enhanced permeability and retention effect (EPR) (Maeda 2012) (Diou, Tsapis et al. 2012). This property can be additionally used to trigger the release of a co-encapsulated drug by focused ultrasound (FUS)

by local PFC cavitation/vaporization followed by capsule shell rupture and subsequent drug release (Singh, Hussein et al. 2012). This strategy is currently investigated to deliver higher drug concentrations in the tumor vicinity and increase the chemotherapy efficacy while avoiding unwanted toxicity to healthy cells (Clark, Wiley et al. 2016). As FUS is clinically employed to ablate and eradicate tumor cells, particularly in prostate (Uchida, Tomonaga et al. 2015) and hepatocellular carcinomas (You, Wang et al. 2016), ultrasound represents an ideal trigger for drug delivery because it is a non-invasive technique, safe to adjacent tissues and provides a precise spatiotemporal control over the thermal and mechanical energy dissipation (Bezagu, Errico et al. 2014) 2014).

These applications are promising but require first the efficient encapsulation of low boiling point PFCs. However, the entrapment of liquid PFCs such as PFH into polymeric nanosystems is a challenging process due to their fluorophilic character and high vapor pressure (Pisani, Fattal et al. 2008) (Mousnier, Huang et al. 2014). Perfluorinated compounds are usually immiscible with hydrophilic or hydrophobic solvents due to favored interactions between fluorinated domains (Koda, Terashima et al. 2014). Accordingly, perfluorinated liquids tend to phase-separate, resulting in low encapsulation efficiencies – 3-9% in nano-sized formulations (Srinivas, Cruz et al. 2010) (Li, Wang et al. 2014) – which represents a limitation for ultrasound imaging and ultrasound-triggered drug delivery. To promote better PFH encapsulation into nanocapsules, we have synthesized PLA polymers containing linear fluorinated end-groups of distinct lengths. The presence of the fluorinated moiety is expected to increase PFH encapsulation efficiency by playing on fluorophilic-fluorophilic interactions. Polymer synthesis, nanocapsule formulation and characterization are reported. Finally, nanocapsule echogenicity and ability to be destroyed by focused ultrasound is evaluated.

2. Materials and Methods

2.1 Materials

D,L-lactide was purchased from Polysciences (Germany) and perfluorohexane (purity>98%) was acquired from Alfa Aesar (Germany). 1-hexanol Acros Organics (Belgium), 2,2,3,3,4,4-Heptafluoro-1-butanol, 1H,1H Perfluoro-1-heptanol, 1H,1H Perfluoro-1-nonanol, 1H,1H Perfluoro-1-dodecanol and 1H,1H Perfluoro-1-tetradecanol were acquired from Fluorochem (United Kingdom). Acetone, tetrahydrofuran (THF) and dichloromethane were purchased from Carlo Erba Reactifs (France), chloroform and diethyl ether from VWR (France). Stannous octoate, sodium cholate, trifluoroacetic acid (TFA) and polyvinyl alcohol (PVA) were provided by Sigma-Aldrich (France). The ultrapure water was produced by a Millipore Synergy 185 apparatus coupled with a RiOs5TM (Millipore, France) with a resistivity of 18.2 M Ω cm. The NMR sample tubes and coaxial inserts were obtained from CortecNet (France).

2.2 Polymer Synthesis

All fluorinated (PLA-C₃F₇, PLA-C₆F₁₃, PLA-C₈F₁₇, PLA-C₁₁F₂₃ and PLA-C₁₃F₂₇) and non-fluorinated (PLA-C₆H₁₃) derivatives of polylactide polymers were synthesized by ring opening polymerization (ROP) with the presence of stannous octoate as catalyst (Singh, Naskar et al. 2011) (Giuntoli, Rosi et al. 2012). All glassware and stir bars were flame-dried and cooled under argon flow. Briefly, in a 10 mL Schlenck tube equipped with a magnetic stir-bar, the D,L-lactide (10.4 mmol, 1.5g) and corresponding initiator (0.075 mmol) – 1-hexanol for PLA-C₆H₁₃, 2,2,3,3,4,4-Heptafluoro-1-butanol for PLA-C₃F₇, 1H,1H Perfluoro-1-heptanol for PLA-C₆F₁₃, 1H,1H Perfluoro-1-nonanol for PLA-C₈F₁₇, 1H,1H Perfluoro-1-dodecanol for PLA-C₁₁F₂₃ or 1H,1H Perfluoro-1-tetradecanol for PLA-C₁₃F₂₇ – were added to the flask under argon flow. The tube was sealed with a rubber cap and a stannous octoate solution (0.05 mmol, 20 mg) dissolved in 2 mL of dried toluene was added through the septum. The tube was purged with argon for 0.5h and the polymerization reaction was conducted with continuous stirring at 130°C for 55 minutes in an oil bath under argon flow. The reaction was quenched by immersing the flask in a cold water bath. Afterwards, the solvent was evaporated under reduced pressure for 1h

and the material was dissolved in 5 mL of chloroform. The product was purified by precipitation as previously described (Diou, Fattal et al. 2014): all polymers were precipitated into cold diethyl ether (80 mL), next, PLA-C₆H₁₃ was dissolved into THF (5mL), whereas the fluorinated polymers were dissolved in acetone (20 mL) and precipitated again in ultrapure water (150 mL). The samples were freeze-dried for 24h and a white powder was obtained. Lactide conversion $\geq 95\%$ (¹H-NMR). ¹H-NMR [400 MHz, CDCl₃, 25°C] **PLA-C₆H₁₃**: δ_H 5.10-5.28 (PLA-CHCH₃COO-), 1.52-1.61 (-CCH₃), 0.88-0.92 (-CH₂CH₃). **PLA-C₃F₇**, **PLA-C₆F₁₃**, **PLA-C₈F₁₇**, **PLA-C₁₁F₂₃** and **PLA-C₁₃F₂₇**: δ_H 5.10-5.28 (PLA-CHCH₃COO-), 4.50-4.70 (-OCH₂CF₂-), 1.52-1.61 (-CCH₃). ¹⁹F-NMR [200 MHz, CDCl₃, 25°C] **PLA-C₃F₇**: δ_F -78.9 to -79.05 (-CF₃), -118.5 to -119 (-CH₂CF₂-) and -125.7 to 125.8 (-CF₂CF₂CF₃); **PLA-C₆F₁₃**, **PLA-C₈F₁₇**, **PLA-C₁₁F₂₃** and **PLA-C₁₃F₂₇**: ¹⁹F-NMR [400 MHz, CDCl₃, 25°C]: δ_F -78.8 to -79.05 (-CF₃), -117.6 to -117.9 (-CH₂CF₂), -120.0 to -120.6 (-CF₂CF₂CF₃), -120.7 to -121.2 (-CH₂CF₂CF₂), -121.2 to -121.6 (-CH₂CF₂CF₂CF₂) and -124.0 to -124.5 (-CF₂CF₃).

2.3 Characterization

All polymers were characterized by size exclusion chromatography (SEC) in chloroform at 30°C with a flow rate of 1 mL.min⁻¹ by two columns (PL-gel 5 μ m MIXED-D 300 x 7.5 mm) calibrated against a curve based on poly(methyl methacrylate) standards (PMMA, Polymer Laboratories, Varian Inc.). The system was coupled to a refractive index detector (Spectrasystem RI-150, Thermo Electro Corp.). ¹H and ¹⁹F-NMR spectra were obtained on a Bruker Avance 400 MHz in CDCl₃ at room temperature.

2.4 Differential Scanning Calorimetry (DSC)

All polymers were sealed in aluminum pans (50 μ L) and placed in a DSC apparatus (DSC Q1000, TA Instruments). All analyses were conducted under nitrogen flow (20 mL.min⁻¹) in a temperature range between 20 and 70°C at a heat and cooling rate of 20°C.min⁻¹.

2.5 Nanocapsules Formulation

Nanocapsules were prepared by the emulsion-evaporation technique, as previously described with modifications (Diou, Tsapis et al. 2012). Briefly, 50 mg of polymer was dissolved in 2 mL of chloroform in a 50 mL glass flask that was sealed with a rubber cap. Next, 30 μL of PFH was introduced through the septum with constant stirring, and the media was emulsified with 10 mL of sodium cholate 1.5% (w/w) at 4°C in a vortex for 1 min. The mixture was then submitted to probe sonication (Branson digital sonifier, France) at 30% of maximal power for 1 min over ice. The solvent was evaporated by magnetic stirring at 300 RPM during 4h in a thermostated bath at 20°C. The samples were then filtered on 0.45 μm PVDF filters (Whatman) and incubated with PVA 1% w/w for 5 days at 4°C. Finally, they were centrifuged at 27.240 g (Optima LE-80K Ultracentrifuge Beckman Coulter, France) during 1h at 4°C and the pellet was resuspended in 5 mL of ultrapure water to yield a final polymer concentration of 25 $\text{mg}\cdot\text{mL}^{-1}$.

2.6 Size and ζ -potential

The hydrodynamic diameter, polydispersity index (Pdl) and zeta potential of nanocapsules were measured using a Zetasizer Nano ZS (Malvern, France) at 20°C. All suspensions were diluted 1:10 in ultrapure water for size measurements and 1 mM NaCl for zeta potential measurements.

2.7 Electron Microscopy

Scanning electron microscopy was performed using a Merlin 6040 (Carl Zeiss, Germany) operating at 3 kV. The nanocapsules were deposited on carbon conductive double-sided tape (Euro-medex, France) and dried at room temperature. Afterwards, they were coated with a palladium–platinum layer of about 3 nm using a Cressington sputter-coater 208HR with a rotary-planetary-tilt stage, fitted with an MTM-20 thickness controller. Transmission electron microscopy (TEM) images were obtained in a JEOL 1400 (Jeol Ltd, USA) operating at 80 kV. All nanocapsules suspensions were diluted to a final concentration of 1 mg/mL polymer in ultrapure water and a 5 μL droplet was deposited on a glow discharged carbon-coated 200

mesh grid. Negative staining was performed using 2% phosphotungstic acid (w/v). All images were acquired with an Orius camera (Gatan Inc, USA).

Cryo-Transmission Electron Microscopy (Cryo-TEM) images were performed using a JEOL 1400 TEM/STEM operating at 120 kV. NC suspensions at 50 mg.mL⁻¹ polymer were deposited (5 µL) on a glow discharged carbon grid (Lacey 200 mesh), automatically blotted for 5 s and plunged into liquid ethane at -175°C by a grid plunge freezer (Leica EM GP). The samples were kept in liquid nitrogen until analysis. Next, they were transferred to a pre-cooled cryo-TEM holder (Gatan 914) and observed under 10 pA/cm² of luminosity, 2 s of exposition and -2 µm of defocus. All images were acquired with a US1000XP camera (Gatan Inc, USA).

2.8 PFH encapsulation efficiency

For PFH quantification, 500 µL of NC suspension was transferred to NMR tubes loaded with a stem coaxial insert containing TFA in D₂O (12 µmol.mL⁻¹) as external standard (Henderson 2002). Freeze-dried samples were also analyzed; 1 mL of unpurified nanocapsule suspension was freeze-dried during 24h employing an Alpha-1-2 LD apparatus (Christ, France). Afterwards, they were hermetically sealed with a rubber cap and stored at -20°C until analysis. A total volume of 1 mL of chloroform then was introduced into the sealed tube by a needle, the suspension was vortexed (5 cycles of 30 seconds) and centrifuged at 0°C for 10 minutes at 1000 RPM. The organic solution was collected in a cold room at 4°C and introduced into an NMR tube loaded with the stem coaxial insert containing TFA in D₂O (12 µmol.mL⁻¹). All spectra were obtained by a Bruker Avance 300 (400 MHz) operating at 4°C. The total amount of encapsulated PFH was determined after integrating the peak at -81.2 ppm, corresponding to the PFH CF₃ group, normalized by the TFA peak area at -76.5 ppm based on a PFH calibration curve in chloroform.

2.9 Cell viability

The cytotoxicity of all NCs was evaluated in two distinct cell lines. Human endothelial umbilical vein cells (HUVEC) were cultivated in DMEM supplemented with 50 U.mL⁻¹ of penicillin, 50 U.mL⁻¹ of streptomycin and 10% FBS. Murine macrophage-monocytes (J774.A1 cell line) were cultivated in RPMI 1640 medium

supplemented with 50 U.mL⁻¹ of penicillin, 50 U.mL⁻¹ of streptomycin and 10% heat inactivated FBS. All cells were cultivated at 37°C at 5% CO₂ in a humidified atmosphere; they were splitted twice a week by trypsinisation for HUVEC and scraping for J774.A1. To assess the *in vitro* cytotoxicity, the MTT assay employed (Gerlier and Thomasset 1986). A total volume of 100 µL of the cells suspension was seeded into 96 well plates (TPP, Switzerland) at a concentration of 8x10³ cells/well or 2x10³ cells/well for 24 and 72h of incubation, respectively. The cells were pre-incubated for 24h and 100 µL of a serial dilution of NCs (1.0x10⁻³ to 10 mg.mL⁻¹) was added to the medium. After 24 or 72h of incubation, 20 µL of 0.5 mg.mL⁻¹ MTT (3-(4,5-dimethylthiazol-2-yl)-2,5-diphenyltetrazolium bromide) (Sigma, France) was added to each well. The medium was then aspirated and replaced by 200 µL of mL dimethylsulfoxide (ACS grade, BioBasic Inc, France). The absorbance [A] was measured with a microplate reader (LAB Systems Original Multiscan MS, Finland) at 570 nm and the cell viability was calculated according to eq. 1, where [A]_{control} corresponds to the absorbance of untreated control cells:

$$\frac{[A]_{test}}{[A]_{control}} \times 100, Eq. 1$$

2.10 *In vitro* Ultrasound Characterization

Ultrasound images were acquired in a degassed water bath maintained at 37°C equipped with acoustic absorbing rubber. All NC were previously degassed and 0.8 mL were transferred to a silicone tube to a final 50 mg.mL⁻¹ suspension. Suspensions of Sonovue[®] 0.1%, PVA 0.7% and nanoparticles (NP) produced with PLA-C₈F₁₇ (without PFH) were used as controls. *In vitro* ultrasound imaging experiments were performed using a programmable ultrasound scanner with a 5 MHz probe with 192 elements (Figure 1). Images were obtained using an ultrafast B-mode sequence (Couture, Bannouf et al. 2009) at 0.1 MPa peak negative pressure. Conventional B-mode (0.1 MPa) and harmonic (10V, executed by pulse inversion and amplitude modulation) images were initially performed for each sample independently. Finally, a disruption pulse was emitted (70V, ~5 MPa peak negative pressure) and the imaging process was repeated, with 65 B-mode images for the total 140 ms pulse sequence. Ultrafast images were acquired at a frame rate of 100 Hz and all data was transferred to a computer for analysis at Matlab (Mathworks,

Natick, MA, USA). The backscattered intensity of the samples was obtained by averaging the power of the first and last image of the video in the region-of-interest (the silicone tube). The resulting intensities were subtracted by the backscattered intensity obtained with the tube filled with ultra-pure water.

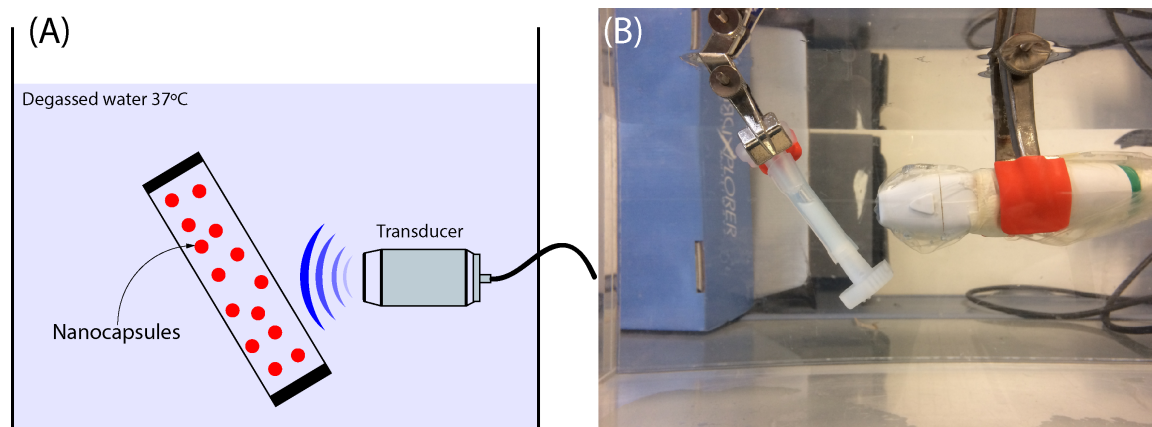


Figure 1: Schematic representation (A) and real view (B) of the US set-up.

2.11 Focused Ultrasound

Focused ultrasound experiments were performed to assess the ability to destroy NCs. 100 μL of 5 $\text{mg}\cdot\text{mL}^{-1}$ NC suspension were transferred to a 96 well microplate (OptiCell[®]) that was placed in a support positioned at the center of the chamber. A 2.25 MHz transducer (SuperSonic Imagine, Aix-en-Provence, AFG3101C) was focused (38 mm $f/d=1$) separately at each microplate well and single bursts of 5 cycles of 100 ms were transmitted by a waveform generator and amplified to 12.3 MPa peak-negative pressure by a radio frequency amplifier (Bezagu, Errico et al. 2014).

3. Results and discussion

3.1 Synthesis and characterization of fluorinated polymers

Poly(lactide) polymers functionalized with either alkyl or fluorinated end-groups of five distinct lengths were synthesized by ring opening polymerization of D,L-lactide. The end-groups are composed of linear carbon chains substituted by fluorine or hydrogen atoms; thus, the synthesized polymers were designated according to the terminal group chemistry and length of fluorinated unit as PLA-C₆H₁₃, PLA-C₃F₇, PLA-C₆F₁₃, PLA-C₈F₁₇, PLA-C₁₁F₂₃ and PLA-C₁₃F₂₇.

All synthesis products were initially characterized by the presence of the lactide signals at 1.60 and 5.23 ppm and the new ester linkage performed with the fluorinated or alkylated alcohol initiators by ¹H-NMR (**Figure 2A**). As previously observed by Böhmer *et al.*, all the fluorinated polymers exhibited a significant shift of the -CH₂O- signal compared with the correspondent initiator from 4.1 ppm to 4.52 and 4.72 ppm, indicating that the chemical environment of those groups were severely influenced by the PLA backbone as well as by the adjacent CF₂ units (Böhmer, Schroeders *et al.* 2006). Accordingly, the -CH₂O- intensity was splitted into two signals with multiplicity of two triplets due to the strong coupling with both fluorine atoms and the geminal proton in the same order of magnitude (~13 Hz), which confirmed the synthesis of fluorinated PLA polymers. Also, the fluorinated derivatives exhibited a shift of the -CF₂CH₂- signals while other CF₂ and CF₃ (-78.9 to -79.0 ppm) resonances were similar to each specific precursor as displayed in the ¹⁹F spectra (**Figure 2B**). The formation of the non-fluorinated derivative, PLA-C₆H₁₃, was verified by the -CH₂O- signal shift from 3.60 to 4.14 ppm of the initiator.

As shown Table 2, a relative good agreement between the experimental masses determined by SEC and the molecular weight targeted at 20 000 g.mol⁻¹ for all the derivatives was observed. The M_n was also determined by ¹H-NMR analysis on the basis of the integration ratio of peak at 5.23 ppm (methine proton of lactide) and 4.52 - 4.72 ppm (methylene protons adjacent to the CF chain) (**Figure 2A**). Slightly lower M_n were calculated than using SEC, around 18 000 g.mol⁻¹, which may be attributed to the dissimilarity of polymer conformation with poly(methyl methacrylate) standards.

The end-modified polymers were also characterized by DSC. They all displayed the same glass-transition temperature (T_g) around 50 to 52°C, similar to

unmodified PLA polymers of similar molecular weight (**Table 1**) (Chen, Chueh et al. 2003) (Giuntoli, 2011). Hence, the small molecular weight end-group caused any impact on the T_g of high molecular weight polylactide.

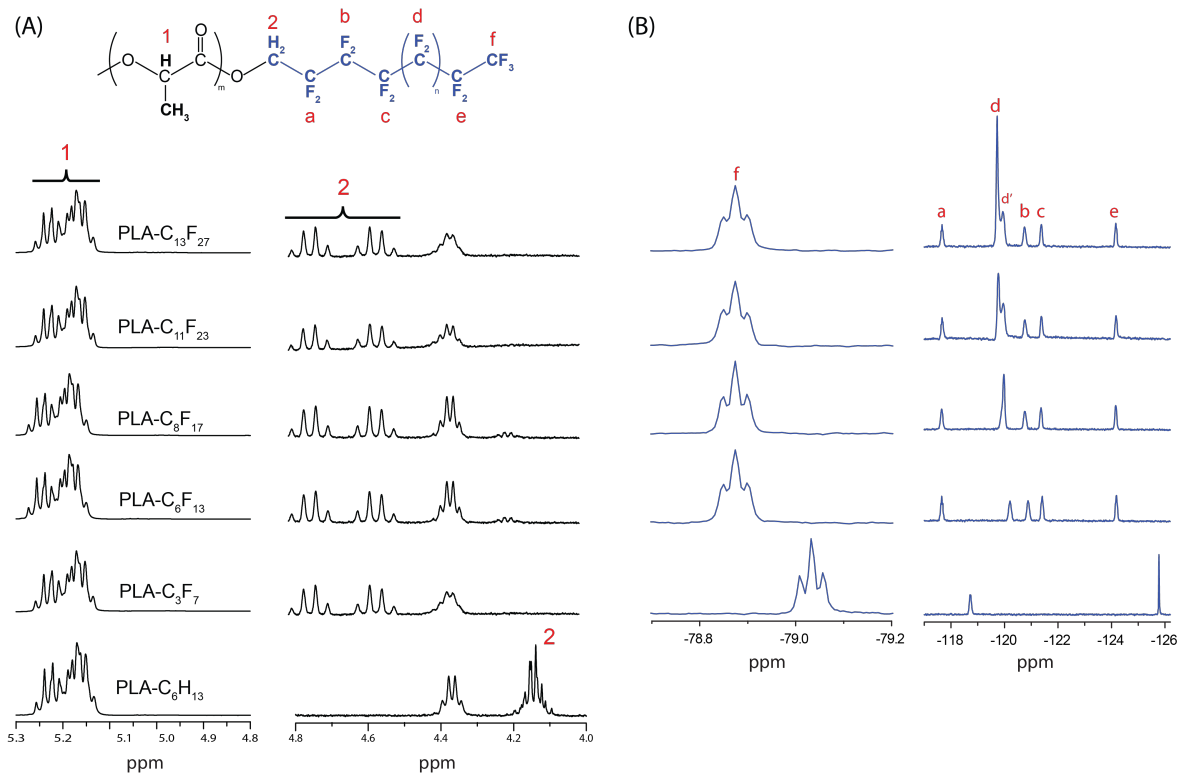


Figure 2. ^1H -NMR spectra of all synthesized polymers with enlargement of the correspondent lactide and ester linkage signals (A). Magnified CF_3 and CF_2 regions in the ^{19}F spectra for PLA-C₃F₇, PLA-C₆F₁₃, PLA-C₈F₁₇, PLA-C₁₁F₂₃ and PLA-C₁₃F₂₇ (B). The ^1H and ^{19}F peak assignment are indicated in the insert. All samples were dissolved in CDCl_3 .

Table 1. Average number molecular weight (M_n) obtained by SEC/ ^1H -NMR, dispersity and glass-transition temperature (T_g) of all synthesized polymers.

Polymer	M_n^{SEC} (g.mol ⁻¹)	Dispersity (\mathcal{D})	M_n^{NMR} (g.mol ⁻¹)	T_g (°C)
PLA-C ₆ H ₁₃	21 000	1.3	20 700	52
PLA-C ₃ F ₇	22 000	1.4	15 000	52
PLA-C ₆ F ₁₃	24 000	1.4	16 600	50
PLA-C ₈ F ₁₇	24 000	1.4	19 600	53
PLA-C ₁₁ F ₂₃	21 000	1.3	18 100	52
PLA-C ₁₃ F ₂₇	22 000	1.4	18 300	53

3.2 PFH Nanocapsules

Fully fluorinated liquid perfluorocarbons usually display high vapor pressure values - 29.1 kPa at 25°C for PFH (Singh, Hussein et al. 2012) - and restricted solubility in organic solvents due to their fluorophilic character (West, Hallett et al. 2004). As a result, most of their content phase separates and evaporates during the formulation of related nano or microdroplets, reducing the PFC encapsulation efficacy (Pisani, Fattal et al. 2008)(Mousnier, 2014). Therefore, fluorinated end-groups with distinct lengths were introduced into the PLA structure to promote “fluorous – fluorous” interactions between the polymer and liquid perfluorocarbons to enhance PFH encapsulation into nanocapsules. The features of NC formulated with fluorinated polymers, such as morphology, size, surface charge and PFH encapsulation efficiency were compared with samples produced with the non-fluorinated polymer PLA-C₆H₁₃.

Initial characterizations demonstrated that all NC were spherical with smooth surfaces as shown by TEM and SEM images (**Figure 3**). The Z-average size was around 150 nm – in agreement with electron microscopy observations – with a negative ζ -potential around -8 mV regardless of end-group chemistry or fluorinated length as displayed in **Table 2**.

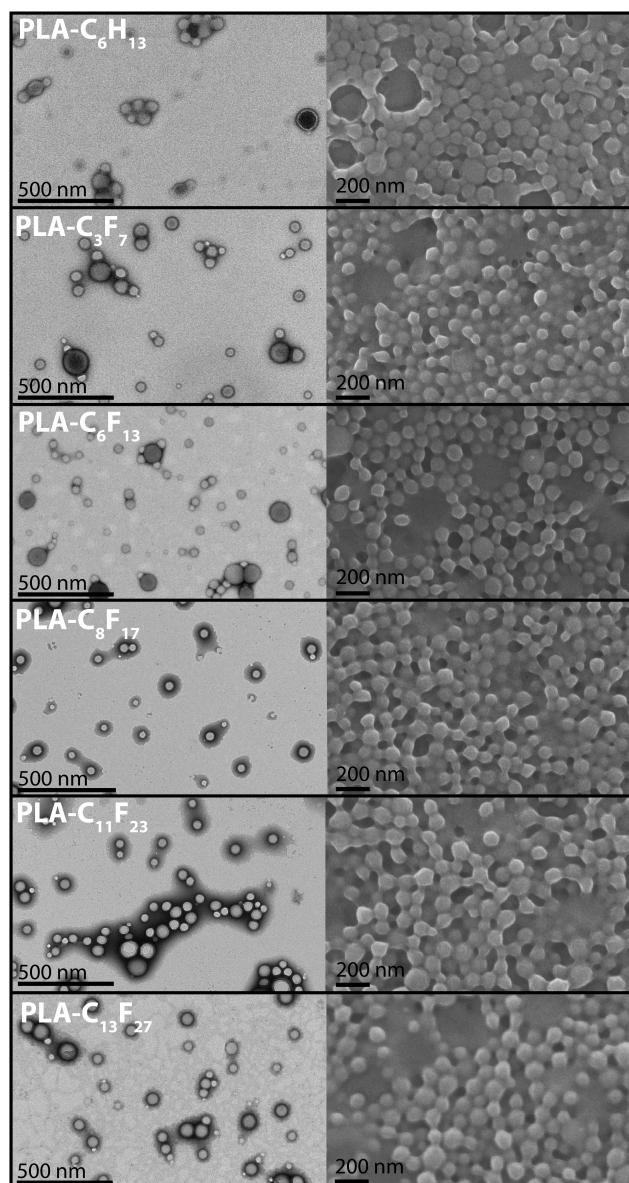


Figure 3. Transmission (left) and scanning electron microscopy images (right) for nanocapsules formulated with fluorinated and non-fluorinated polymers.

Table 2. Z-average size, ζ -potential and polydispersity index for nanocapsules formulated with fluorinated and non-fluorinated polymers.

Sample	Size \pm SD (nm)	Pdl	ζ -potential (mV)
PLA-C ₆ H ₁₃	153 \pm 2.0	0.12 \pm 0.01	-7.7 \pm 0.8
PLA-C ₃ F ₇	152 \pm 1.2	0.11 \pm 0.02	-9.0 \pm 0.5
PLA-C ₆ F ₁₃	158 \pm 1.3	0.10 \pm 0.01	-9.0 \pm 0.7
PLA-C ₈ F ₁₇	156 \pm 1.6	0.14 \pm 0.01	-7.8 \pm 0.5
PLA-C ₁₁ F ₂₃	156 \pm 0.6	0.12 \pm 0.02	-7.4 \pm 0.1
PLA-C ₁₃ F ₂₇	153 \pm 1.5	0.10 \pm 0.01	-8.0 \pm 0.9

Entrapped PFH was effectively visualized by Cryo-TEM images, revealing spherical core-shell morphologies constituted by thin polymeric layers engulfing the electron dense perfluorocarbon as shown in **Figure 4** for PLA-C₆H₁₃, PLA-C₃F₇, PLA-C₈F₁₇ and PLA-C₁₃F₂₇. All samples displayed capsules containing distinct amounts of PFH, exhibiting dark cores with a wide intensity range and also presented apparently unloaded polymeric nanoparticles, an indication of inhomogeneous encapsulation (Figure S4). Moreover, no morphological distinction among polymer end-group chemistry or F-length was observed.

Some capsules also presented a predominant light interior or bright spots inside the perfluorocarbon phase as show by the white arrows in Figure 4; such areas might be related to the freezing process, creating low PFH densities inside the capsules – due to the formation of frozen PFH drops – that generated correspondent void and lighter regions in the PFC phase. After exposure to the electron beam radiation, a PFH phase-transition – partial melting or sublimation – might favor the observation of less bright areas in the NC (Figure S5). Those observations are consistent with Lattin *et al.* that reported the increased frequency of bright nanoemulsion droplets for the lower boiling point perfluoropentane (Bp=29°C) in comparison with perfluorohexane (Bp=56°C) and perfluoroheptane (Bp=82°C) (Lattin, Belnap et al. 2012).

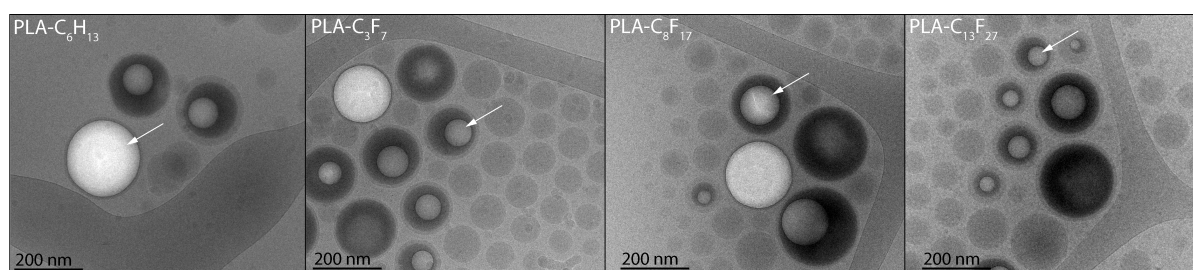


Figure 4. Cryo-TEM images of nanocapsules formulated with fluorinated PLA-C₃F₇, PLA-C₈F₁₇ and PLA-C₁₃F₂₇ as well as non-fluorinated PLA-C₆H₁₃ polymers.

The total entrapped PFH was then quantified for NC in suspension and after freeze-drying by ¹⁹F-NMR. The samples prepared with the non-fluorinated polymer exhibited an encapsulation efficiency of 9.2±0.1% for suspensions and 4.0±0.5% after freeze drying, in agreement with results obtained for nanocapsules formulated with regular PLGA polymers (Srinivas, Cruz et al. 2010). All NC formulated with F-polymers showed a 2-fold increase in the total perfluorohexane encapsulation

compared to PLA-C₆H₁₃ as exhibited in **Figure 5**. A 15±1.0% of PFH encapsulation efficiency for suspensions and 9.5±0.8% plateau for freeze-dried samples was reached, although without significant difference as a function of fluorinated chain length. Obviously, the freeze-drying process induced the loss of non-encapsulated PFH nanodroplets, as previously observed for PFOB NCs (Diou, Brûlet et al. 2016). These results suggest a preferential interaction between fluorinated polymers and PFH, independently of the fluorinated end-chain length, reducing the PFH loss during solvent evaporation and increasing the final encapsulation efficiency. Nonetheless, the PFH solubility and volatility still prevents higher encapsulation. Comparatively, mPEG-polycaprolactone polymers containing terminal C₃F₇ groups were also successful in enhancing of PFH entrapment into NCs around ~15% as reported by Li *et al.* (Li, Wang et al. 2014).

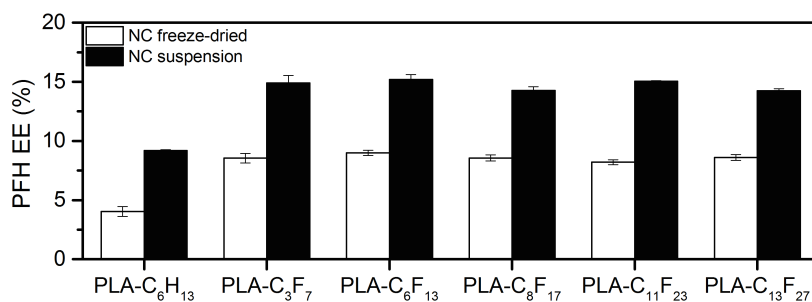


Figure 5. Perfluorohexane encapsulation efficiency for NCs submitted to freeze-drying (white bars) and in suspension (dark bars).

3.3 *In vitro* cytotoxicity of NCs

Fluorinated-compounds in biomedical devices are usually limited because of their persistence and consequent toxicity in the organism (Riess 2009). Indeed the stable C-F bond hinders an effective enzymatic or metabolic degradation that results in low excretion profiles, especially for linear fluorinated compounds longer than C₇F₁₅ (Zaggia and Ameduri 2012) (Barmentlo, Stel et al. 2015). To assess the *in vitro* impact of fluorinated end-groups with distinct lengths on cellular viability, NCs formulated with fluorinated polymers were incubated with two distinct cell lines, human umbilical vein endothelial (HUVEC) and murine macrophage-like (J774.A1) during 24h or 72h. The MTT assays showed that NCs did not induced modifications in cell mitochondrial activity after 24h or 72h, independently of NC concentration,

end-group chemistry or fluorinated end-group lengths (**Figure 6 top**). For J774.A1, a slight decrease of mitochondrial activity down to 75% was observed for 10 mg/mL NCs after 24h of exposure. After 72h exposure, mitochondrial activity decreased down to 75 and 50% of controls at NC concentrations of 4 and 10 mg/mL, respectively (**Figure 5 bottom**). In both cases, no specific toxicity was induced due to the presence of the fluorinated groups. One should note that the reduction of mitochondrial activity of J774.A1 cells was only observed for very high NC concentrations. In addition, as previously discussed by Reul *et al.*, the distinct profiles for the two cell lines arises from the ability of J774.A1 to internalize faster and to a higher extent NCs than HUVEC (Reul, Tsapis et al. 2012). Although only a limited *in vitro* cytotoxicity was observed, additional *in vivo* studies are required to investigate the effects resulting from the prolonged exposure to NCs.

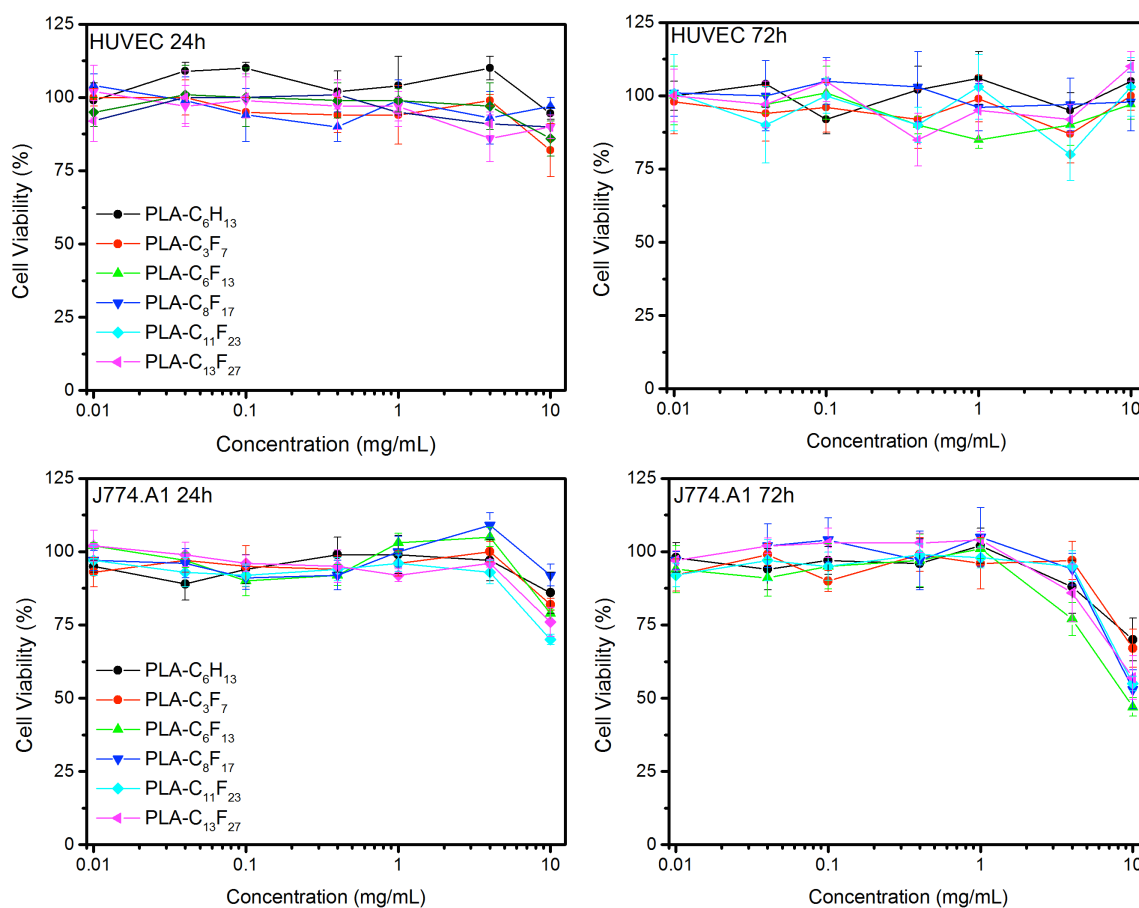


Figure 6. Cell viability as a function of NC concentration for HUVEC (top) and J774.A1 (bottom) at 24h (left) and 72h (right). All results are presented as mean \pm SD.

3.4 *In vitro* Ultrasound imaging

The imaging ability of NCs was evaluated *in vitro* using an ultrafast B-mode imaging system based on compounded plane-wave ultrasound transmissions (Errico, Pierre et al. 2015). All images were obtained with fixed 50 mg.mL^{-1} concentrations of NC at 37°C and compared to the background gray-scale level produced by ultrapure water. At this temperature, the PFH vapor pressure increases to 48.6 kPa – against 29.1 kPa at 25°C – and potentially favors a gas-phase nucleation. Ultrasound images obtained in the fundamental mode displayed a clear contrast enhancement arising from NC formulated with fluorinated polymers (from 1.5×10^4 until 5.5×10^4 arbitrary units, a.u.) compared to those produced with PLA- C_6H_{13} (0.5×10^4 a.u.) (Figure 7). Additionally, the same fluorinated-shelled NCs generated harmonic echoes, enhancing the backscattering intensities from 10-fold to 40-fold higher than PLA- C_6H_{13} . For both ultrasound-imaging modalities, all samples exhibited long-lasting echogenicity of more than 10 minutes. As expected, Sonovue[®] greatly increased the ultrasound contrast compared to all NCs (from 12-fold to 35-fold) in the fundamental and harmonic modes due to its micrometer size and its gaseous core. In absence of PFH, the PLA- C_8F_{17} nanoparticles and PVA solution did not yield any significant signal enhancement.

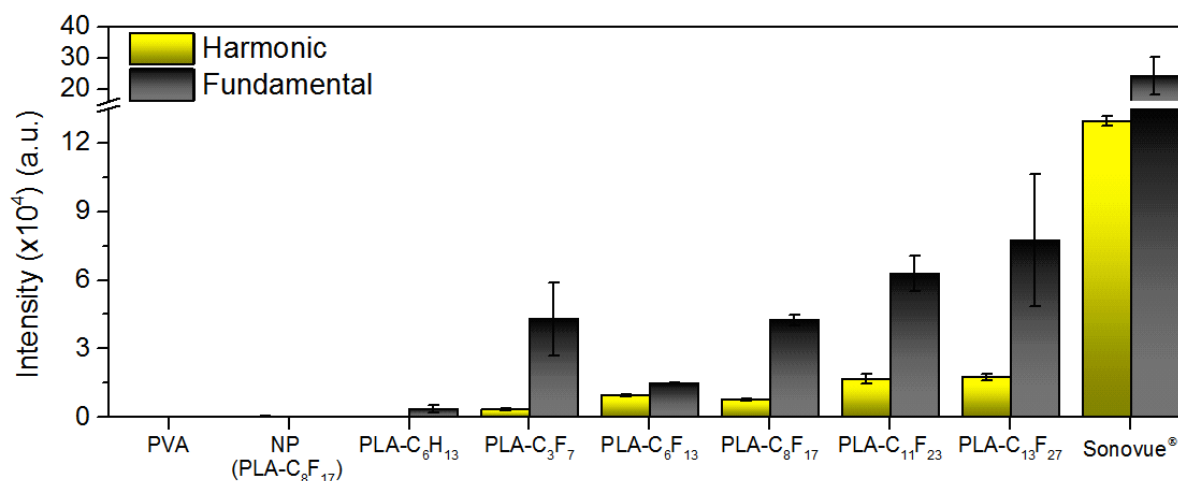


Figure 7. B-mode ultrasound response performed at the fundamental (black bars) and harmonic (white bars) modalities for all nanocapsules.

The acoustic enhancement observed for samples formulated with fluorinated polymers indicate that the total amount of PFH is a key parameter required to

modulate the echogenicity of NCs, given these possess similar sizes. Interestingly, polymers containing longer F-units, such as PLA-C₁₁F₂₃ and PLA-C₁₃F₂₇, exhibited higher backscattering – particularly in harmonic imaging – compared to shorter or non-fluorinated NCs. Such acoustic dependency on F-length might be related to the lack of homogeneity along the fluorine interface and may favor PFH nucleation. In fact, Koda et al. and Cheng et al. reported that partly fluorinated polymers produce structured surfaces with segregation between fluorinated and hydrogenated segments that modifies the interfacial morphology and increases the surface roughness (Koda, Terashima et al. 2015, Cheng, Spraul et al. 2016). The generation of local cavities or fins are related to enhance vapor trapping and may act as a catalyst for PFH bubble nucleation (Choi, David et al. 2016).

At higher acoustic pressures (peak negative pressure ~5 MPa), a clear signal enhancement is observed after 10 pulses for all NCs formulated with fluorinated polymers, indicating that the shell was disrupted. For these samples, the PFH is possibly completely vaporized causing the polymeric shell to shatter and allow the gas-phase to freely vibrate, which momentarily increases the echo. This transitory higher echogenicity then decreases back to the initial echogenicity as the gas bubble is dissolved or destroyed in a similar profile as observed for microbubbles (Couture, Fink et al. 2012).

3.5 PFH vaporization by FUS

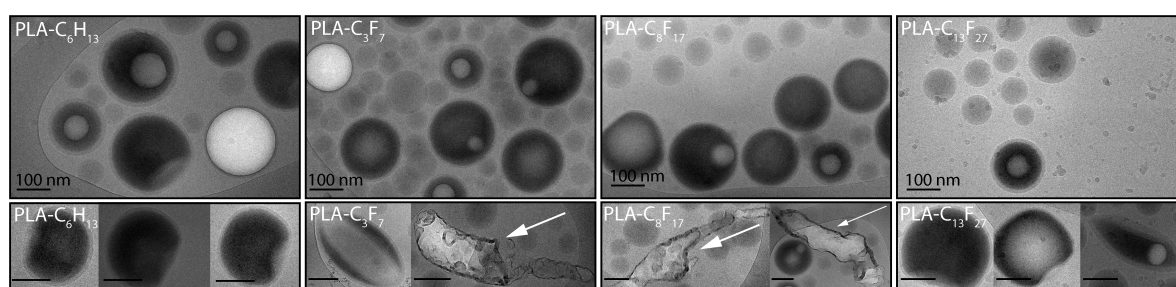


Figure 8. Cryo-TEM images of nanocapsules after FUS exposure. Intact/spherical (top) and buckled and collapsed nanocapsules (bottom) were observed for all samples. All scale bars represent 100 nm. The white arrows indicate nanocapsules that were completely disrupted.

The PFH-loaded NCs present an interesting potential to release chemotherapeutics inside solid tumors after local accumulation driven by the EPR effect. Their great advantage resides on the acoustic-sensitivity of the low boiling

point PFH that can be remotely induced to vaporize by focused ultrasound (FUS) and trigger the release of co-entrapped drug content in the desired location. To evaluate the ability of PFH to undergo acoustic drop vaporization under FUS, the NCs were exposed to acoustic pulses compatible with safe *in vivo* applications and analyzed morphologically by Cryo-TEM (Bezagu, Errico et al. 2014).

All samples displayed a predominant population of spherical and intact NCs with core-shell morphology in all images (**Figure 8 top**). However, a distinct population of capsules that exhibited deformed structures according to polymer end-chemistry were also visualized: samples produced with PLA-C₆H₁₃ exhibited some buckled NCs, suggesting that a partial PFH vaporization occurred and produced only a localized distortion of the polymeric shell. For NCs prepared with fluorinated polymers – PLA-C₃F₇, PLA-C₈F₁₇ and PLA-C₁₃F₂₇ – more intense shell deformations led to a complete morphological change that culminated, in many cases, to a capsule disruption and the observation of debris, some of them at the micrometric size range (white arrows) (**Figure 8 bottom**). It is important to emphasize that the focus of the ultrasonic beam is small compared to the total volume of the samples, a factor that contributed to reduce the number of viewable debris during Cryo-TEM. Although these NCs have probably experienced a more effective gas-phase nucleation caused by the oscillating pressure, further investigations are still required to find the optimal FUS conditions to overcome the Laplace and hydrostatic pressures exerted over PFH as well as the PFC own vapor pressure. The presence of PFH inside several capsules indicates that longer FUS exposition time intervals are still required for homogeneous NC disruption.

Comparatively, corresponding samples were submitted to heating at 60°C for 10 minutes in an oil bath – above the PFH boiling point (56°C). The results showed no morphological discrepancy or size variation compared to the control group (**Figure S5 and S6**), thus suggesting that the ultrasound mechanical effects are required in addition to the thermal ones to promote a more effective vaporization as previously reported (Novell, Al Sabbagh et al. 2015). Additionally, as the temperature in focal area of FUS might become higher than 65°C within 1s (You, Wang et al. 2016), the polymer shell might be above its T_g of 52°C (**Table 2**) – therefore making polymer shell deformation easier.

In summary, entrapping perfluorocarbons into rigid-shelled polymeric layers represent an advantageous strategy to perform imaging and drug-delivery at the

nanoscale. The versatile PLA shell is reported to provide prolonged stability, biocompatibility, mechanical strength and also the suitability to anchor targeting ligands or stealth moieties (Diou, Fattal et al. 2014). In addition, the functional polymeric phase and the perfluorinated core are able to assimilate chemotherapeutics, enabling the NC to act as drug-carrier vehicles intended for tumor treatment (Boissenot, Fattal et al. 2016). Altogether, the higher PFH contents obtained with fluorinated polymers presents the perspective to enhance the imaging quality of NCs, allowing the visualization of inner tumor structures and enhance localized drug-release.

4. Conclusions

We have successfully synthesized polylactide polymers containing fluorinated end-groups of different lengths, from C_3F_7 until $C_{13}F_{27}$ that were formulated into nanocapsules containing a perfluorohexane core. These samples produced any specific *in vitro* cytotoxicity towards HUVEC and J774.A1 cell lines. The employment of fluorinated polymers increased in 2-fold the encapsulation efficiency of perfluorohexane into nanocapsules, though any particular effect related to fluorine chain length was observed. The nanocapsules formulated with fluorinated polymers enhanced the acoustic response compared to PLA- C_6H_{13} in both fundamental and harmonic ultrasound imaging modalities with fluorine chain-length dependency in the mechanism of perfluorohexane nucleation. When submitted to focused ultrasound, the visualization of both intact and debris of nanocapsules, also with end-group dependency, indicate that the perfluorocarbon was partly vaporized. The co-encapsulation of chemotherapeutics for solid tumor therapy is considered to future works.

5. Acknowledgements

This work has been supported by the Région Ile-de-France in the framework of DIM Nano-K and the French National Research Agency (ANR) under grant ANR-10-NANO-06 as part of the “Investissements d’Avenir” program. We have benefited from the facilities and expertise of the Electron Microscopy facilities of Imagerie-Gif, (<http://www.i2bc.paris-saclay.fr/spip.php?article282>) with the precious help of C. Boulogne. This core facility is member of the Infrastructures en Biologie Santé et

Agronomie (IBiSA), and is supported by the French national Research Agency under Investments for the Future programs “France-Biolmaging”. Institut Galien Paris-Sud is a member of the Laboratory of Excellence LERMIT supported by a grant from ANR (ANR-10-LABX-33). We are also thankful to Conselho Nacional de Desenvolvimento Científico e Tecnológico (CNPq) for the financial support and to Prof. Najet Yagoubi and Merhez Sghaier for helping with DSC experiments.

6. References

- Bezagu, M., C. Errico, V. Chaulot-Talmon, F. Monti, M. Tanter, P. Tabeling, J. Cossy, S. Arseniyadis and O. Couture (2014). "High spatiotemporal control of spontaneous reactions using ultrasound-triggered composite droplets." J Am Chem Soc **136**(20): 7205-7208.
- Böhmer, M. R., R. Schroeders, J. A. M. Steenbakkers, S. H. P. M. de Winter, P. A. Duineveld, J. Lub, W. P. M. Nijssen, J. A. Pikkemaat and H. R. Stapert (2006). "Preparation of monodisperse polymer particles and capsules by ink-jet printing." Colloids and Surfaces A: Physicochemical and Engineering Aspects **289**(1–3): 96-104.
- Boissenot, T., E. Fattal, A. Bordat, S. Houvenagel, J. Valette, H. Chacun, C. Gueutin and N. Tsapis (2016). "Paclitaxel-loaded PEGylated nanocapsules of perfluorooctyl bromide as theranostic agents." European Journal of Pharmaceutics and Biopharmaceutics **108**: 136-144.
- Borden, M. A., G. V. Martinez, J. Ricker, N. Tsvetkova, M. Longo, R. J. Gillies, P. A. Dayton and K. W. Ferrara (2006). "Lateral Phase Separation in Lipid-Coated Microbubbles." Langmuir **22**(9): 4291-4297.
- Chang, E. H., W. K. Chong, S. K. Kasoji, P. A. Dayton and W. K. Rathmell (2016). "Management of Indeterminate Cystic Kidney Lesions: Review of Contrast-enhanced Ultrasound as a Diagnostic Tool." Urology **87**: 1-10.
- Clark, A. J., D. T. Wiley, J. E. Zuckerman, P. Webster, J. Chao, J. Lin, Y. Yen and M. E. Davis (2016). "CRLX101 nanoparticles localize in human tumors and not in adjacent, nonneoplastic tissue after intravenous dosing." Proceedings of the National Academy of Sciences of the United States of America **113**(14): 3850-3854.
- Cosco, D., E. Fattal, M. Fresta and N. Tsapis (2015). "Perfluorocarbon-loaded micro and nanosystems for medical imaging: A state of the art." Journal of Fluorine Chemistry **171**: 18-26.
- Couture, O., S. Bannouf, G. Montaldo, J.-F. Aubry, M. Fink and M. Tanter (2009). "Ultrafast Imaging of Ultrasound Contrast Agents." Ultrasound in Medicine & Biology **35**(11): 1908-1916.
- Dalvi, S. V. and J. R. Joshi (2015). "Modeling of microbubble dissolution in aqueous medium." Journal of Colloid and Interface Science **437**: 259-269.
- Diou, O., A. Brûlet, G. Pehau-Arnaudet, E. Morvan, R. Berti, K. Astafyeva, N. Taulier, E. Fattal and N. Tsapis (2016). "PEGylated nanocapsules of perfluorooctyl bromide: Mechanism of formation, influence of polymer concentration on

morphology and mechanical properties." Colloids and Surfaces B: Biointerfaces **146**: 762-769.

Diou, O., N. Tsapis, C. Giraudeau, J. Valette, C. Gueutin, F. Bourasset, S. Zanna, C. Vauthier and E. Fattal (2012). "Long-circulating perfluorooctyl bromide nanocapsules for tumor imaging by ¹⁹F MRI." Biomaterials **33**(22): 5593-5602.

Du, L., Y. Jin, W. Zhou and J. Zhao (2011). "Ultrasound-Triggered Drug Release and Enhanced Anticancer Effect of Doxorubicin-Loaded Poly(D,L-Lactide-Co-Glycolide)-Methoxy-Poly(Ethylene Glycol) Nanodroplets." Ultrasound in Medicine & Biology **37**(8): 1252-1258.

Duncanson, W. J., L. R. Arriaga, W. L. Ung, J. A. Kopechek, T. M. Porter and D. A. Weitz (2014). "Microfluidic Fabrication of Perfluorohexane-Shelled Double Emulsions for Controlled Loading and Acoustic-Triggered Release of Hydrophilic Agents." Langmuir **30**(46): 13765-13770.

Emilio, Q., C. Fabrizio, B. Michele, R. Sandro, G. Lorena, R. Laura and P.-M. Roberto (2004). "Characterization of Focal Liver Lesions with Contrast-specific US Modes and a Sulfur Hexafluoride-filled Microbubble Contrast Agent: Diagnostic Performance and Confidence." Radiology **232**(2): 420-430.

Errico, C., J. Pierre, S. Pezet, Y. Desailly, Z. Lenkei, O. Couture and M. Tanter (2015). "Ultrafast ultrasound localization microscopy for deep super-resolution vascular imaging." Nature **527**(7579): 499-502.

Geers, B., I. Lentacker, N. N. Sanders, J. Demeester, S. Meairs and S. C. De Smedt (2011). "Self-assembled liposome-loaded microbubbles: The missing link for safe and efficient ultrasound triggered drug-delivery." Journal of Controlled Release **152**(2): 249-256.

Giuntoli, G., L. Rosi, M. Frediani, B. Sacchi and P. Frediani (2012). "Fluoro-functionalized PLA polymers as potential water-repellent coating materials for protection of stone." Journal of Applied Polymer Science **125**(4): 3125-3133.

Guédra, M. and F. Coulouvrat (2015). "A model for acoustic vaporization of encapsulated droplets." The Journal of the Acoustical Society of America **138**(6): 3656-3667.

Henderson, T. J. (2002). "Quantitative NMR Spectroscopy Using Coaxial Inserts Containing a Reference Standard: Purity Determinations for Military Nerve Agents." Analytical Chemistry **74**(1): 191-198.

Javadi, M., W. G. Pitt, D. M. Belnap, N. H. Tsosie and J. M. Hartley (2012). "Encapsulating Nanoemulsions Inside eLiposomes for Ultrasonic Drug Delivery." Langmuir **28**(41): 14720-14729.

Kaul, S. and H. Ito (2004). "Microvasculature in Acute Myocardial Ischemia: Part I." Evolving Concepts in Pathophysiology, Diagnosis, and Treatment **109**(2): 146-149.

Li, H., J. Wang, P. Wang, J. Zheng, F. Song, T. Yin, G. Zhou, R. Zheng and C. Zhang (2014). "Phase-transition contrast nanocapsules triggered by low-intensity ultrasound." Chemical Communications **50**(96): 15163-15166.

Maeda, H. (2012). "Vascular permeability in cancer and infection as related to macromolecular drug delivery, with emphasis on the EPR effect for tumor-selective drug targeting." Proceedings of the Japan Academy Series B-Physical and Biological Sciences **88**(3): 53-71.

Mousnier, L., N. Huang, E. Morvan, E. Fattal and N. Tsapis (2014). "Influence of polymer end-chemistry on the morphology of perfluorohexane polymeric microcapsules intended as ultrasound contrast agents." Int J Pharm **471**(1-2): 10-17.

Novell, A., C. Al Sabbagh, J.-M. Escoffre, C. Gaillard, N. Tsapis, E. Fattal and A. Bouakaz (2015). "Focused ultrasound influence on calcein-loaded thermosensitive stealth liposomes." International Journal of Hyperthermia **31**(4): 349-358.

Pisani, E., E. Fattal, J. Paris, C. Ringard, V. Rosilio and N. Tsapis (2008). "Surfactant dependent morphology of polymeric capsules of perfluorooctyl bromide: Influence of polymer adsorption at the dichloromethane-water interface." Journal of Colloid and Interface Science **326**(1): 66-71.

Pisani, E., N. Tsapis, B. Galaz, M. Santin, R. Berti, N. Taulier, E. Kurtisovski, O. Lucidarme, M. Ourevitch, B. T. Doan, J. C. Beloeil, B. Gillet, W. Urbach, S. L. Bridal and E. Fattal (2008). "Perfluorooctyl Bromide Polymeric Capsules as Dual Contrast Agents for Ultrasonography and Magnetic Resonance Imaging." Advanced Functional Materials **18**(19): 2963-2971.

Rapoport, N., K.-H. Nam, R. Gupta, Z. Gao, P. Mohan, A. Payne, N. Todd, X. Liu, T. Kim, J. Shea, C. Scaife, D. L. Parker, E.-K. Jeong and A. M. Kennedy (2011). "Ultrasound-mediated tumor imaging and nanotherapy using drug loaded, block copolymer stabilized perfluorocarbon nanoemulsions." Journal of Controlled Release **153**(1): 4-15.

Singh, A., A. K. Naskar, D. Haynes, M. J. Drews and D. W. Smith (2011). "Synthesis, characterization and surface properties of poly(lactic acid)-perfluoropolyether block copolymers." Polymer International **60**(3): 507-516.

Singh, R., G. A. Hussein and W. G. Pitt (2012). "Phase transitions of nanoemulsions using ultrasound: Experimental observations." Ultrasonics Sonochemistry **19**(5): 1120-1125.

You, Y. F., Z. G. Wang, H. T. Ran, Y. Y. Zheng, D. Wang, J. S. Xu, Z. B. Wang, Y. Chen and P. Li (2016). "Nanoparticle-enhanced synergistic HIFU ablation and

transarterial chemoembolization for efficient cancer therapy." *Nanoscale* **8**(7): 4324-4339.

Supplementary Information

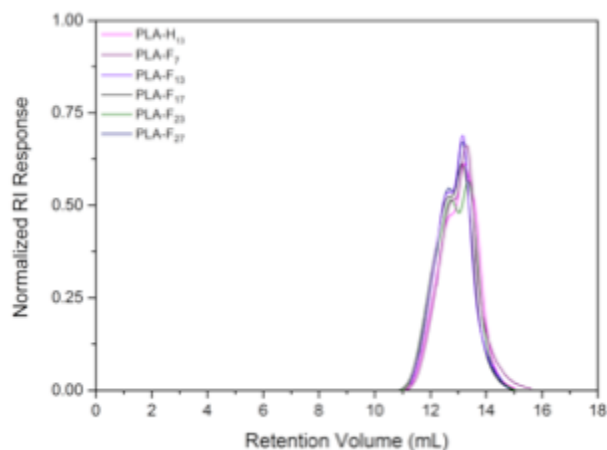


Figure S1. SEC chromatogram of all fluorinated and non-fluorinated polymers. All analysis were performed in chloroform at 40°C.

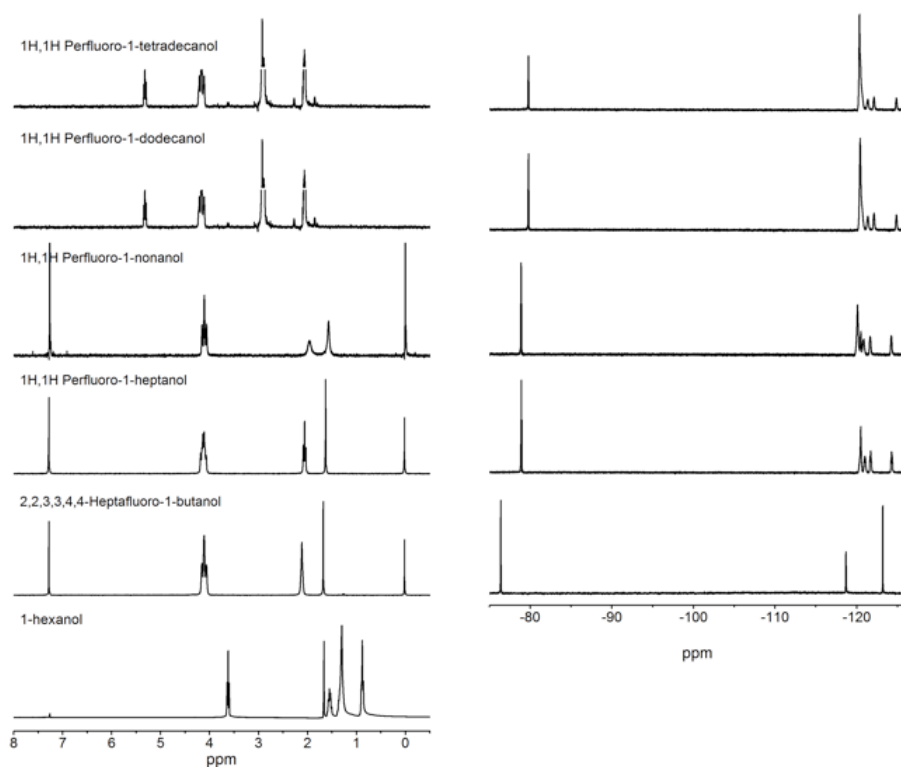


Figure S2. ^1H (left) and ^{19}F -NMR (right) spectra of the initiators utilized for polymer synthesis. All samples were dissolved in CDCl_3 except 1H,1H Perfluoro-1-dodecanol and 1H,1H Perfluoro-1-tetradodecanol that were dissolved in deuterated acetone.

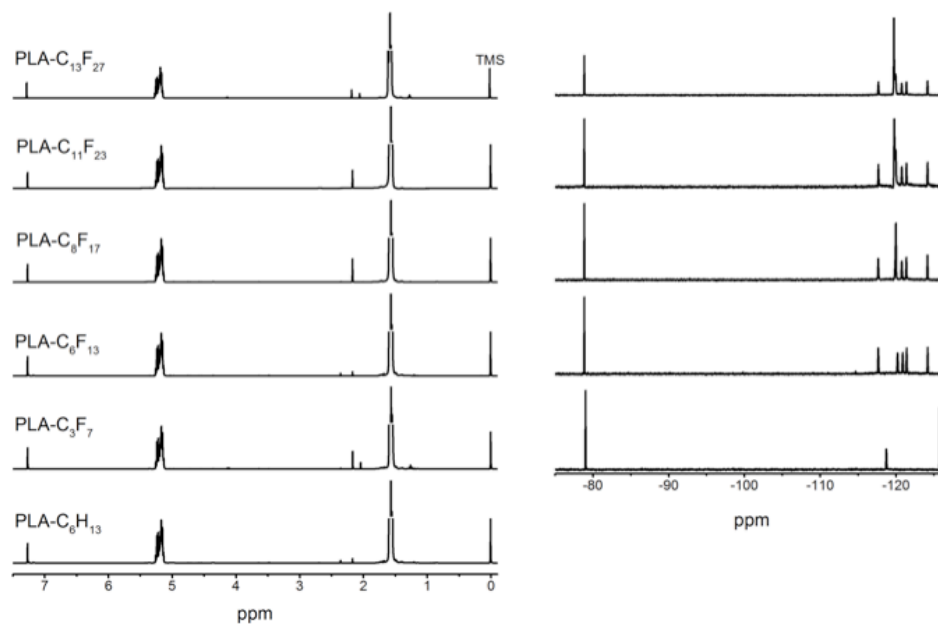


Figure S3. ^1H (left) and ^{19}F -NMR spectra (right) of all synthesized polymers. All samples were dissolved in CDCl_3 .

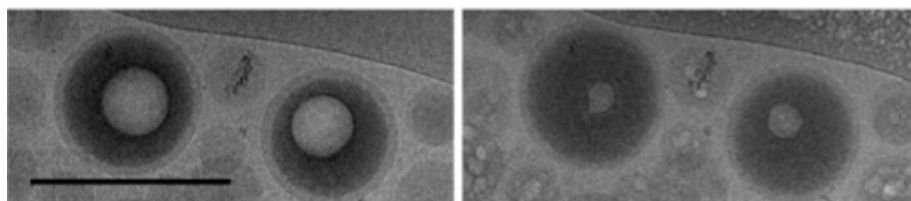


Figure S4. Cryo-TEM images of nanocapsules formulated with $\text{PLA-C}_3\text{F}_7$ before (left) and after prolonged electron beam irradiation (right). Scale bar represents 200 nm.

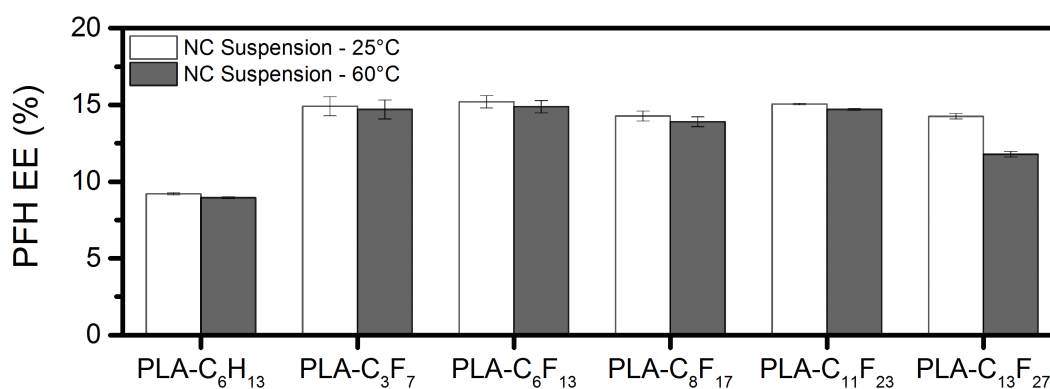


Figure S5. Perfluorohexane encapsulation efficiency for nanocapsules heated up to 60°C for 10 minutes.

Chapter 4

Dynamics and influence of F-polymers over microcapsules

The higher PFH entrapment efficiency as well as the intense acoustic response observed for fluorinated-shelled NC generated the interest in analyzing more deeply the impact of the fluorinated polymers in providing a more favorable interface for interaction with perfluorocarbons. We started our investigations by studying the end-group dynamics by ^{19}F relaxometry in pure solvent solution and comparing its behavior with a PFH containing sample. In addition, we evaluated the impact of fluorinated polymers by analyzing the final morphology assumed by microcapsules (MC) containing PFH. The observed supramolecular architecture was correlated with the segmental end-group dynamics previously observed. Although such MCs are not suitable for intravenous administration due to their inherent low compressibility, the ADV phenomenon was studied for thick-shelled samples, showing that the entrapped PFH is able to overcome the structural resistance offered by the PLA shell when submitted to FUS stimuli.

Influence of fluorinated end-group dynamics on the morphology of microcapsules

Guilherme Picheth^{a,d}, Sophie Houvenagel^a, Leociley Menezes^e, Anderson Barison^e, Camille Dejean^b, Olivier Couture^c, Rilton Freitas^d, Laurence Moine^a, Nicolas Tsapis^{a*}

^a Institut Galien Paris-Sud, CNRS, Univ. Paris-Sud, Université Paris-Saclay, 92296 Châtenay-Malabry, France.

^b BioCIS, CNRS, Univ. Paris-Sud, Université Paris-Saclay, 92296 Châtenay-Malabry, France.

^c Institut Langevin, ESPCI ParisTech, CNRS (UMR 7587), INSERM (U979), Paris, France.

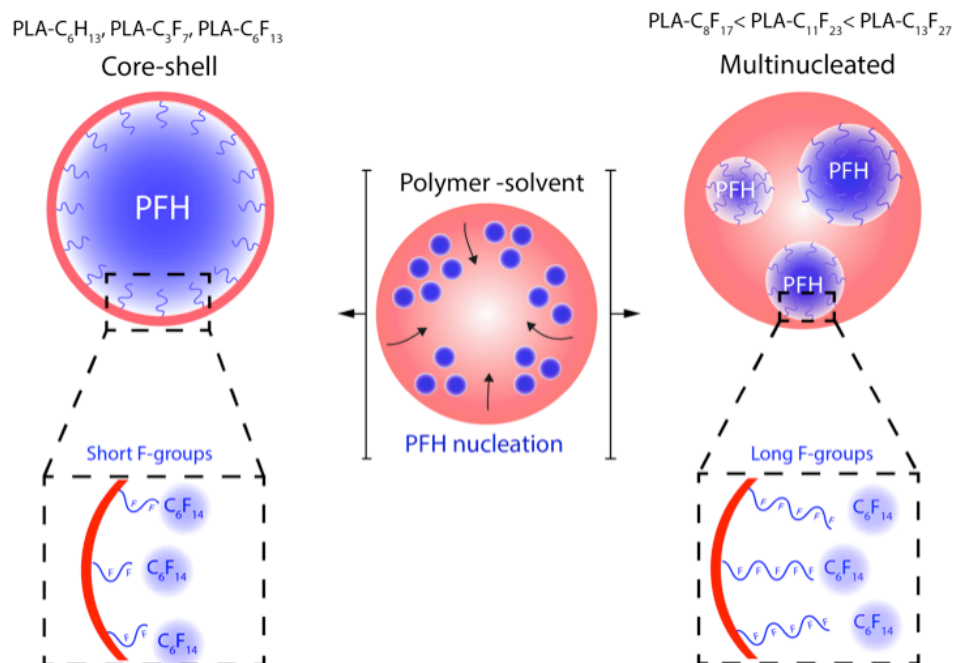
^d Biopol, Chemistry Department, Federal University of Paraná, 81531-980. Curitiba, PR, Brazil.

^e NMR Center, Chemistry Department, Federal University of Paraná, 81531-980. Curitiba, PR, Brazil.

* Corresponding author at: Institut Galien Paris-Sud, CNRS, Univ. Paris-Sud, Université Paris-Saclay, 92296 Châtenay-Malabry, France Tel.: +33 146835813. E-mail address: nicolas.tsapis@u-psud.fr (Nicolas Tsapis).

Keywords: Perfluorocarbon microcapsules, perfluorohexane, fluorinated polymers, focused ultrasound, end-group dynamics, fluorous interaction

Graphical abstract



Abstract

Fully fluorinated compounds are usually characterized for their inherent immiscibility with hydrophobic and lipophobic solvents. This so-called “fluorophilic” character is responsible for low encapsulation efficiencies of low-boiling point perfluorocarbons (PFC) into polymer shelled nano or microcapsules. To enhance the interaction of biodegradable polymers towards PFCs, we synthesized polylactide (PLA) polymers containing five distinct lengths of fluorinated end-groups (from C_3F_7 until $C_{13}F_{27}$). ^{19}F spin-lattice (T_1) and spin-spin relaxation times (T_2) revealed reduced mobility of the fluorinated units with dependency on fluorinated chain length in the order $C_3F_7 > C_8F_{17} > C_{13}F_{27}$. The presence of perfluorohexane (PFH) generated a further decrease on the segmental mobility, indicating a greater extent of fluororous interactions. T_2 analysis of the CF_3 resonance of PLA- C_3F_7 varied from $540 \pm 50 \mu s$ in $CDCl_3$ to $81 \pm 15 \mu s$ after the addition of PFH. Such decrease of dynamic domains altered the morphology of microcapsules ($\sim 4.5 \mu m$) according to polymer concentration and F-group length as observed by confocal microscopy. Comparatively, PLA polymers containing short fluorinated groups (C_3F_7 and C_6F_{13}) generated microcapsules with core-shell morphologies, whereas those formulated with long F-units (C_8F_{17} , $C_{11}F_{23}$ and $C_{13}F_{27}$) favored the formation of multinucleated capsules. Additionally, all microcapsules formulated with fluorinated PLA increased by two-fold the PFH entrapment efficiency compared to non-fluorinated polymers and were successfully vaporized by focused ultrasound (FUS). As a result of performance under ultrasound exposure, the fluorinated-shelled microcapsules appear as promising candidates for chemoembolization triggered by FUS.

1. Introduction

Fully and partly fluorinated compounds are widely explored in the chemical industry and academic research for its inherent immiscibility with hydrophobic and lipophobic solvents. This so-called “fluorophilic” character is responsible for low or “gas like” intermolecular attraction forces which renders a corresponding inertness and biocompatibility for such molecules, features that attracted special attention for a wide range of biomedical applications (Krafft and Riess 2015). In particular, liquid perfluorocarbons (PFCs), such as perfluorohexane (PFH) or perfluorooctyl bromide (PFOB) are described to be minimally absorbed, eliminated from the lungs by evaporation and cause any significant histological, cellular or biochemical disturbance (Shaffer, Foust et al. 1997); therefore, these PFCs are intensively investigated for their potential to act as intravascular contrast agents (Cosco, Fattal et al. 2015).

Recent reports describe the use of capsules containing PFOB to provide *in vivo* ^{19}F -MRI or ultrasound detection and also passively deliver paclitaxel to CT-26 colon cancer cells (Pisani, Tsapis et al. 2008) (Diou, Fattal et al. 2014) (Boissenot, Fattal et al. 2016). Similar formulations utilize the fully fluorinated PFH as active core for its lower boiling point, which configures as a very sensitive probe to undergo liquid-to-gas transition by acoustic and thermal stimuli and allow real-time ultrasonic imaging (Singh, Hussein et al. 2012).

Nonetheless, the entrapment of fully fluorinated PFCs within a polymeric shell is a process that depends on the interfacial properties of the fluorinated liquid, polymer and chosen surfactant (Pisani, Fattal et al. 2008). Mousnier *et al.* showed the impact of polymer end-group chemistry on the final morphology of PFH-containing microcapsules composed by poly(lactide) (PLA) and poly(lactide-co-glycolide) PLGA shells (Mousnier, Huang et al. 2014). As PFH favors selective interactions among fluorophilic domains and induces phase-separation towards conventional macromolecular stabilizing interfaces (Koda, Terashima et al. 2014), we propose the utilization of PLA polymers containing distinct lengths of fluorinated end-groups (PLA- C_xF_y) to generate compartmented and oriented fluorophilic interfaces towards PFH drops. It was previously demonstrated that a wide range of fluorinated end-groups linked to the PLA chain – from C_3F_7 to $\text{C}_{13}\text{F}_{27}$ – augmented

the PFH entrapment into nanocapsules, resulting in more efficient acoustic responses.

In this work, we investigate the influence of linear fluorinated groups of distinct lengths in the formulation of PFH microcapsules (MC). A correlation among end-group dynamics and the final morphology assumed by MC by the solvent-evaporation method is presented. Lower fluorine mobility is disclosed in chloroform, a system that eventually favored the stabilization of multiple PFH drops by long F-chain PLA polymers. These results indicate that long F-chains – $C_8F_{17} > C_{11}F_{23} > C_{13}F_{27}$ – might potentially adsorb more effectively along C_6F_{14} interfaces and tune the polymeric backbone behavior in determined systems, increasing the PFC encapsulation and leading to the formation of more acoustic sensitive MC.

2. Materials and Methods

2.1 Materials

D,L-lactide was purchased from Polysciences (Germany) and perfluorohexane 98+% was acquired from Alfa Aesar (Germany). 1-hexanol was obtained from Acros Organics (Belgium), 2,2,3,3,4,4-Heptafluoro-1-butanol, 1H,1H Perfluoro-1-heptanol, 1H,1H Perfluoro-1-nonanol, 1H,1H Perfluoro-1-dodecanol and 1H,1H Perfluoro-1-tetradecanol were acquired from Fluorochem (United Kingdom). Acetone, tetrahydrofuran (THF) and dichloromethane were purchased from Carlo Erba Reactifs (France), chloroform and diethyl ether from VWR (France). Nile red, stannous octoate, sodium cholate, trifluoroacetic acid (TFA) were provided by Sigma-Aldrich (France). The ultrapure water was produced by a RIOS/Milli-Q system (Millipore, France), with a resistivity of 18.2 M Ω cm. The NMR sample tubes and coaxial inserts were obtained from CortecNet (France).

2.2 Polymer Synthesis

All fluorinated (PLA-C₃F₇, PLA-C₆F₁₃, PLA-C₈F₁₇, PLA-C₁₁F₂₃ and PLA-C₁₃F₂₇) and non-fluorinated (PLA-C₆H₁₃) derivatives of polylactide polymers were synthesized by ring opening polymerization (ROP) with the presence of stannous octoate as catalyst (Singh, Naskar et al. 2011) (Giuntoli, Rosi et al. 2012). All glassware and stir bars were flame-dried and cooled under argon flow. Briefly, in a 10 mL Schlenck tube equipped with a magnetic stir-bar, the D,L-lactide (10.4 mmol, 1.5g) and corresponding initiator (0.075 mmol) – 1-hexanol for PLA-C₆H₁₃, 2,2,3,3,4,4-Heptafluoro-1-butanol for PLA-C₃F₇, 1H,1H Perfluoro-1-heptanol for PLA-C₆F₁₃, 1H,1H Perfluoro-1-nonanol for PLA-C₈F₁₇, 1H,1H Perfluoro-1-dodecanol for PLA-C₁₁F₂₃ or 1H,1H Perfluoro-1-tetradecanol for PLA-C₁₃F₂₇ – were added to the flask under argon flow. The tube was sealed with a rubber cap and a stannous octoate solution (0.05 mmol, 20 mg) dissolved in 2 mL of dried toluene was added through the septum. The tube was purged with argon for 0.5h and the polymerization reaction was conducted with continuous stirring at 130°C for 55 minutes in an oil bath under argon flow. The reaction was quenched by immersing the flask in a cold water bath. Afterwards, the solvent was evaporated under reduced pressure for 1h and the material was dissolved in 5 mL of chloroform. The product was purified by

precipitation as previously described (Diou, Fattal et al. 2014): all polymers were precipitated into cold diethyl ether (80 mL), next, PLA-C₆H₁₃ was dissolved into THF (5mL), whereas the fluorinated polymers were dissolved in acetone (20 mL) and precipitated again in ultrapure water (150 mL). The samples were freeze-dried for 24h and a white powder was obtained. Lactide conversion $\geq 95\%$ (¹H-NMR). ¹H-NMR [400 MHz, CDCl₃, 25°C] **PLA-C₆H₁₃**: δ_{H} 5.10-5.28 (PLA-CHCH₃COO-), 1.52-1.61 (-CCH₃), 0.88-0.92 (-CH₂CH₃). **PLA-C₃F₇**, **PLA-C₆F₁₃**, **PLA-C₈F₁₇**, **PLA-C₁₁F₂₃** and **PLA-C₁₃F₂₇**: δ_{H} 5.10-5.28 (PLA-CHCH₃COO-), 4.50-4.70 (-OCH₂CF₂-), 1.52-1.61 (-CCH₃). ¹⁹F-NMR [400 MHz, CDCl₃, 25°C] **PLA-C₃F₇**: δ_{F} -78.9 to -79.05 (-CF₃), -118.5 to -119 (-CH₂CF₂-) and -125.7 to 125.8 (-CF₂CF₂CF₃); **PLA-C₆F₁₃**, **PLA-C₈F₁₇**, **PLA-C₁₁F₂₃** and **PLA-C₁₃F₂₇**: ¹⁹F-NMR [400 MHz, CDCl₃, 25°C]: δ_{F} -78.8 to -79.05 (-CF₃), -117.6 to -117.9 (-CH₂CF₂), -120.0 to -120.6 (-CF₂CF₂CF₃), -120.7 to -121.2 (-CH₂CF₂CF₂), -121.2 to -121.6 (-CH₂CF₂CF₂CF₂) and -124.0 to -124.5 (-CF₂CF₃).

2.3 Characterization

All polymers were characterized by size exclusion chromatography (SEC) in chloroform at 30°C with a flow rate of 1 mL.min⁻¹ by two columns (PL-gel 5 μ m MIXED-D 300 x 7.5 mm) calibrated against a curve based on poly(methyl methacrylate) standards (PMMA, Polymer Laboratories, Varian Inc.) The system was coupled to a refractive index detector (Spectrasystem RI-150, Thermo Electro Corp.). ¹H and ¹⁹F-NMR spectra were obtained on a Bruker Advance 400 MHz in CDCl₃ at room temperature.

2.4 Interfacial surface tension

The interfacial surface tension was performed in a Tracker tensiometer (Teclis, France). PFH was previously filtrated by a column of aluminum oxide. A constant 2 μ L PFH or sodium cholate drop was formed by a syringe and a G20 stainless steel needle inside an optical glass cuvette containing fixed polymer concentrations of 25 mg.mL⁻¹ in chloroform previously filtered by 0.22 μ m (Millipore). The temperature was kept at 20°C and the interfacial surface tension was

determined from the drop profile employing the Laplace equation and the forces balance between capillarity and gravity.

2.4 ^{19}F -NMR T_1 and T_2 Relaxation

^{19}F Spin-lattice and spin-spin relaxation measurements were performed in CDCl_3 with fixed polymer concentrations of $25 \text{ mg}\cdot\text{mL}^{-1}$. The samples were not degassed. Samples containing $15 \mu\text{L}$ of PFH were also evaluated. All experiments were performed on a Bruker Avance 300 (400 MHz) at 25°C . ^{19}F T_1 was determined by the inversion-recovery pulse sequence ($T_1\text{IR}$). The delay (τ) between the inversion and read-pulse was varied along 16 values from 1 to 22s. The total number of scans was 32, spectral width=100 ppm and relaxation delay=22s. ^{19}F T_2 was measured by the Carr-Purcell-Meiboom-Gill (CPMG) pulse sequence along 20 values of τ , from 0.25 to 1ms. The number of scans was 64, spectral width=100 ppm and relaxation delay=7s. The Relaxation times were obtained by nonlinear least-squares fitting of a mono- exponential function with $r^2 \geq 0.98$ for all samples.

2.6 Microcapsules Formulation

Microcapsules were prepared by the emulsion-evaporation technique, as described before (Mousnier, Huang et al. 2014) with modifications. Briefly, the desired amount of polymer was dissolved into 2 mL of chloroform or dichloromethane in a 50 mL glass flask. Afterwards, $50 \mu\text{L}$ of Nile red ($55 \mu\text{g}\cdot\text{mL}^{-1}$) was added and the flask was sealed with a rubber cap. Next, $30 \mu\text{L}$ of PFH was introduced through the septum with constant stirring and the media was emulsified with 10 mL of sodium cholate 1.5% (w/w) at 4°C . The mixture was submitted to high-speed homogenization at 8.000 RPM using an Ultra-Turrax T25 (IKA) coupled with a SN25-10G dispersing tool in an ice bath for 1 minute. The solvent was removed by rotary evaporation (Büchi) with a 30°C water bath and recirculation chiller at -10°C . A vacuum gradient from 400 to 30 mbar in 7 steps of 5 minutes was employed. Afterwards, the total volume of each sample was completed to 10 mL with ultrapure water.

2.7 Confocal Microscopy

Microcapsules were washed twice with ultrapure water by centrifugation and resuspended in glycerol to minimize motion. All samples were observed in a Zeiss LSM-510 confocal scanning microscope with a 1 mW helium neon laser operating at excitation of 551 nm and 636 nm of emission, Plan Achromat 63X objective (NA 1.40 oil immersion) and pinhole diameter at 71 nm. For thickness and diameter analysis, the images were stacked at 0.42 μm along the z-axis and the measurements were performed in the equatorial plane of each capsule as previously described (Mounier, 2014).

2.8 Scanning Electron Microscopy

Scanning electron microscopy was performed in a Merlin 6040 (Carl Zeiss, Germany) operating at 3 kV. All microcapsules were washed twice with ultrapure water by centrifugation to remove the excess of sodium cholate, deposited on carbon conductive double-sided tape (Euro-medex, France) and dried at room temperature. Afterwards, they were coated with a palladium–platinum layer of about 3 nm using a Cressington sputter-coater 208HR with a rotary-planetary-tilt stage, fitted with an MTM-20 thickness controller.

2.9 PFH encapsulation efficiency by ^{19}F -NMR spectroscopy

For PFH quantification, 1 mL of microcapsules was freeze-dried during 24h employing an Alpha-1-2 LD apparatus (Christ). The flasks were hermetically sealed with a rubber cap and stored at -20°C until analysis. The PHF encapsulation efficiency was determined as described by Diou *et al.* (Diou, Fattal *et al.* 2014): a total volume of 1 mL of chloroform was introduced into the sealed tube by a needle, the suspension was vortexed (5 cycles of 30 seconds) and centrifuged at 0°C for 10 minutes at 5000 rpm. The organic solution was collected in a cold room at 4°C and introduced into an NMR tube that was afterwards loaded with a stem coaxial insert containing TFA in D_2O ($12 \mu\text{mol}\cdot\text{mL}^{-1}$) as external standard (Henderson 2002). All spectra were obtained in a Bruker Avance 300 (400 MHz) operating at 4°C . The total amount of encapsulated PFH was determined after integrating the peak at -81.2

ppm, corresponding to the PFH CF_3 group, normalized by the TFA peak area at -76.5 ppm based on a PFH calibration curve in chloroform.

2.10 Focused ultrasound

Focused ultrasound experiments were performed to assess the ability to destroy NCs. 100 μL of 5 $\text{mg}\cdot\text{mL}^{-1}$ NC suspension were transferred to a 96 well microplate (OptiCell[®]) that was placed in a support positioned at the center of the chamber. A 2.25 MHz transducer (SuperSonic Imagine, Aix-en-Provence, AFG3101C) was focused (38 mm $f/d=1$) separately at each microplate well and single bursts of 5 cycles of 100 ms were transmitted by a waveform generator and amplified to 12.3 MPa peak-negative pressure by a radio frequency amplifier (Bezagu, Errico et al. 2014).

3. Results and Discussion

3.1 Polymers synthesis and characterization

Linear fluorinated units were introduced into the poly(lactide) chains with the intent to increase the cohesion with fluorophilic components and ultimately reduce the dispersive work during the formulation of microdroplets containing immiscible phases by emulsification processes. End-group fluorinated or alkylated polymers were synthesized by ring opening polymerization of D,L-lactide as previously described (Böhmer, Schroeders et al. 2006) (Giuntoli, Rosi et al. 2012). The polylactide main chain is constituted of fixed ~140 repetitive units containing different lengths of fluorinated end-groups. All polymers were designated according to the terminal group chemistry and length of fluorinated unit as PLA-C₆H₁₃, PLA-C₃F₇, PLA-C₆F₁₃, PLA-C₈F₁₇, PLA-C₁₁F₂₃ and PLA-C₁₃F₂₇. They were characterized by ¹H and ¹⁹F-NMR and exhibited similar values with an average molecular weight of 25.000 g.mol⁻¹ as assessed by SEC (Supplementary data).

3.2 Polymers dynamics

Fluorinated liquids are poorly soluble in organic media and, as the solvent evaporates during the microcapsule formation by emulsion/evaporation process, the PFC phase-separates as small insoluble droplets that diffuses towards the center of the drop to reduce the interfacial tension within the solvent-polymer solution (Pisani, Fattal et al. 2008). Once the solvent is eliminated, the polymer precipitates continuously at the interface, generating a rigid shell that engulfs the liquid fluorocarbon. The final morphology depends on many factors, including the interfacial tension among the immiscible phases and the control on solvent evaporation (Torza and Mason 1970) (Watanabe, Kimura et al. 2013) (Li, Dong et al. 2015). Therefore, prior studying the microcapsules formation with these modified polymers, its essential to investigate the behavior of polymer end-group chemistry on the interface between the polymer and the liquid fluorocarbon, PFH.

Interfacial surface tension measurements against a PFH or sodium cholate (SC) phases were conducted at fixed 25 mg.mL⁻¹ polymer concentrations. All samples exhibited an average value of 3.0±1.0 mN.m⁻¹ against PFH and were unable to decrease the surface tension compared to the solvent itself regardless of end-

group chemistry of F-length (**Table 1**). The lack of interfacial adsorption onto PFH might be explained by the mass ratio disparity between the relatively small fluorinated blocks compared to the PLA main chain (C₆ to C₁₃ for fluorinated block vs 140 repetitive units for PLA). Indeed, as the PLA polymers are well solvated in chloroform – Hildebrand parameter (δ_T) of 18.9 MPa^{0.5} for unmodified PLA and 18.7 MPa^{0.5} for CHCl₃ (Agrawal, Saran et al. 2004) – a conformational rearrangement based on the higher solubility of PLA chains within chloroform may conceal the fluorinated group inside the PLA coil, hindering an effective interaction with PFH. Also, any changes on the surface tension value with the sodium cholate interface relative to the solvent were observed and the samples displayed an average of 7.2±0.3 mN.m⁻¹.

Table 1. Interfacial surface tension at the perfluorohexane/polymer in chloroform and polymer/sodium cholate 1.5% interfaces. All polymers were dissolved at fixed 25 mg.mL⁻¹ in chloroform.

Polymer	PFH/polymer interface (mN.m ⁻¹)	Polymer/SC 1.5% interface (mN.m ⁻¹)
PLA-C ₆ H ₁₃	3.0±0.5	7.5±0.2
PLA-C ₃ F ₇	3.0±0.3	7.0±0.1
PLA-C ₆ F ₁₃	3.0±0.5	7.1±0.5
PLA-C ₈ F ₁₇	3.1±0.4	7.1±0.2
PLA-C ₁₁ F ₂₃	3.0±0.3	7.2±0.3
PLA-C ₁₃ F ₂₇	3.1±0.4	7.4±0.1

PFH displayed 3.2±0.3 mN.m⁻¹ in CHCl₃ and 22.5±0.2 mN.m⁻¹ in SC 1.5%.

During the microcapsule formulation by an emulsification process, a polymer rearrangement may be envisaged when the solvent evaporates. This may lead to eventual modification of the polymeric network favoring the formation of rich F-regions, and thus, enhancing the overall entrapment of PFH as previously demonstrated for nanocapsules. Hence, the fluorinated end-groups assume an important role to ameliorate the compartmentalization of PFH droplets in such dynamic media. To evaluate the affinity of the fluorinated chains with PFH in solution – a situation prior to solvent evaporation – we have evaluated the dynamics of three fluorinated polymers, PLA-C₃F₇, PLA-C₈F₁₇ and PLA-C₁₃F₂₇ in CDCl₃ by employing spin-lattice relaxation (T₁) and spin-spin (T₂) measurements (Twum, McCord et al. 2014). The fluorine dynamics assumed in CDCl₃ was probed and compared with a PFH mixed system. The nomenclature and ¹⁹F-NMR peak labeling consists

alphabetically with the position of the fluorinated resonance respective to the PLA chain according to Koda *et al.* (**Figure 1**) (Koda, Terashima et al. 2011).

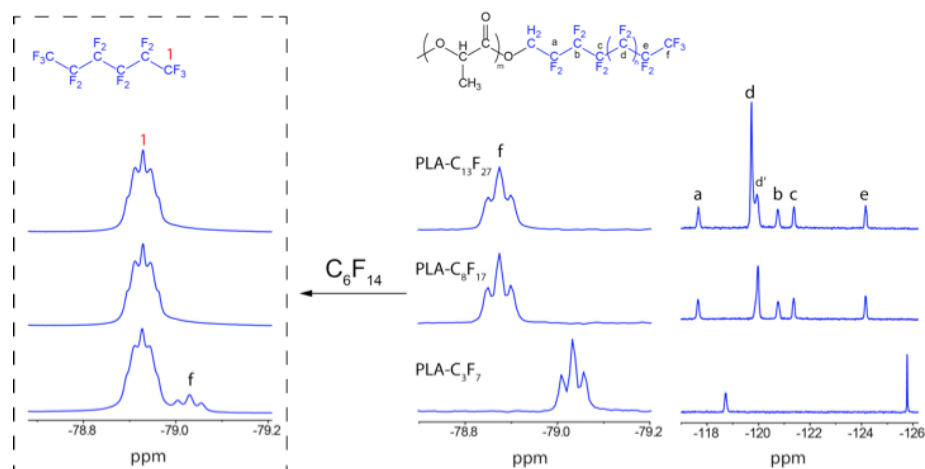


Figure 1. Magnified CF_3 and CF_2 regions of the ^{19}F -NMR spectra for PLA- C_3F_7 , PLA- C_8F_{17} and PLA- $\text{C}_{13}\text{F}_{27}$ in CDCl_3 . The inserts (left) exhibit the CF_3 resonance in a mixed system of polymer and perfluorohexane. ^{19}F peak assignment is indicated in the top.

The mobility of the CF_3 resonance decreased for polymers functionalized with longer fluorinated units in the order $\text{C}_3\text{F}_7 > \text{C}_8\text{F}_{17} > \text{C}_{13}\text{F}_{27}$, exhibiting T_2 values of 540, 210 and 76 μs , respectively (**Table 2**). Such low mobility values were supported by T_1 measurements: CF_3 $T_1 = 1.2\text{s}$ (PLA- C_3F_7), 0.65s (PLA- C_8F_{17}) and 0.45s (PLA- $\text{C}_{13}\text{F}_{27}$). Increasing the F-group length also affected the $^a\text{CF}_2$ nuclei dynamics by decreasing its mobility as observed by T_1 values of 1.29s, 0.63s and 0.46s for PLA- C_3F_7 , PLA- C_8F_{17} and PLA- $\text{C}_{13}\text{F}_{27}$, respectively. The reduction in the local fluorine mobility is related to the strong electronegativity in the C-F bond that generates linear and rigid chain conformations, reducing the segmental mobility along the CF chain (Kadayakkara, Damodaran et al. 2014) (Koda, Terashima et al. 2015).

Table 2. ^{19}F spin-lattice (T_1) and spin-spin relaxation (T_2) values of CF_3 resonances for samples dissolved in deuterated chloroform with and without perfluorohexane. All results are expressed in seconds or microseconds \pm standard deviation of curve fitting.

Sample	T_1 (s)		T_2 (μs)	
	CDCl_3	$\text{CDCl}_3 + \text{PFH}$	CDCl_3	$\text{CDCl}_3 + \text{PFH}$
PLA- C_3F_7	2.08 ± 0.10	3.00 ± 0.06	540 ± 50	81 ± 15
PLA- C_8F_{17}	1.83 ± 0.03	---	210 ± 20	---
PLA- $\text{C}_{13}\text{F}_{27}$	1.74 ± 0.08	---	76 ± 10	---

Afterwards, 15 μL of PFH was added to each polymer solution in order to simulate the system behavior just before emulsification with sodium cholate. Unfortunately, some of the PFH resonances overlapped with the CF_3 polymer signals for PLA- C_8F_{17} and PLA- $\text{C}_{13}\text{F}_{27}$. Only PLA- C_3F_7 exhibited such resonance well segregated from those of PFH because of the smaller electron density, which permitted a resonance shift to lower magnetic fields not coincidentally with PFH (**Figure 1**). The CF_3 signal of PLA- C_3F_7 showed a significant T_2 decrease, disclosing lower mobility as well as enhanced affinity with the perfluorocarbon (**Figure 2**).

According to those results, the introduction of PFH was able to induce a rearrangement of the polymeric organization of PLA- C_3F_7 in CDCl_3 . As the fluorinated units are well exposed in the organic phase, their contact with PFH generates interactions that may lead to the formation of fluorophilic interfaces during the solvent evaporation, a process that might also depends on the length of the polymer fluorinated group. However, this scenario illustrates their behavior only in stable organic solutions; during the solvent-evaporation process in which microcapsules are formulated, transitory and thermodynamically unstable interfaces are created. Therefore, the ability of each fluorinated derivative to better stabilize and retain the PFH as a liquid core was further studied in MC.

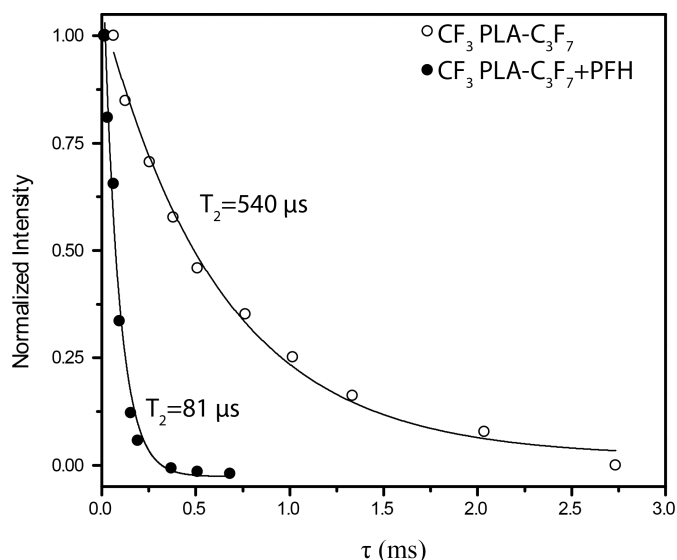


Figure 2. T_2 decay profile for the CF_3 resonance of PLA- C_3F_7 in CDCl_3 without (open circles) and with perfluorohexane (filled circles).

3.3 Solvent Influence on MC formulation

The Impact of the fluorinated end-groups on the final morphology of microcapsules was then studied for all synthesized polymers. All microcapsules were initially formulated with fixed amounts of polymer – 50 mg.

A clear and subtle distinction on MC morphology was observed according to the fluorinated end-group length. In all cases, PLA-C₆H₁₃, PLA-C₃F₇ and PLA-C₆F₁₃ exhibited core-shell morphologies comprising a well centered PFH phase; however, increasing the end-group length to C₈F₁₇, C₁₁F₂₃ and C₁₃F₂₇ generated proportionally higher extents of randomly distributed PFH drops as displayed by the white arrows in **Figures 3 top**. Such samples presented the formation of multinucleated structures. Although all samples were predominately smooth as shown by SEM images in **Figures 3 bottom**, a certain amount of rough shelled microcapsules were also observed in all samples. According to Chung, *et al.*, this morphological variation might be related to the fast evaporation process used, which promoted a polymer concentration gradient towards the interface (Chung, Huang et al. 2001). Also, a partial PFH vaporization during the solvent evaporation step (performed at 30°C) may have caused a volumetric expansion of the MCs and, as the temperature dropped, a subsequent shrinkage altered the continuous spreading of the polymer at the interface. Lebedeva *et al.* has observed a similar behavior for PFH containing microspheres (Lebedeva, Sanders et al. 2016).

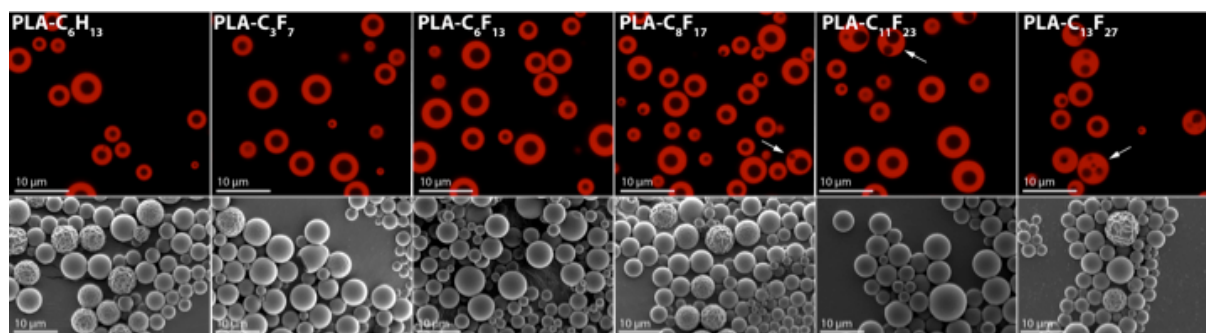


Figure 3. Confocal (top) and scanning electron microscopy (bottom) images of microcapsules. Scale bar represents 10 μm.

As a result, samples prepared with short fluorinated end-groups, PLA-C₃F₇ and PLA-C₆F₁₃ or PLA-C₆H₁₃, presented the formation of core-shell capsules. Only MC formulated with longer fluorine groups, PLA-C₈F₁₇, PLA-C₁₁F₂₃ and PLA-C₁₃F₂₇,

caused the appearance of different morphologies, indicating that the shell precipitates prior to complete PFH nucleation. Thus, the extent of the fluorinated group played an important role in the fluorocarbon stability, suggesting that longer fluorinated chains were able to better interact and restrain the PFH diffusion (as illustrated in **Figure 4**). This observation is in accordance with Koda *et al.* (Koda, Terashima *et al.* 2015), that demonstrated the dependency on F-group length to generate richer fluorophilic environments for enhanced perfluorocarbon stabilization.

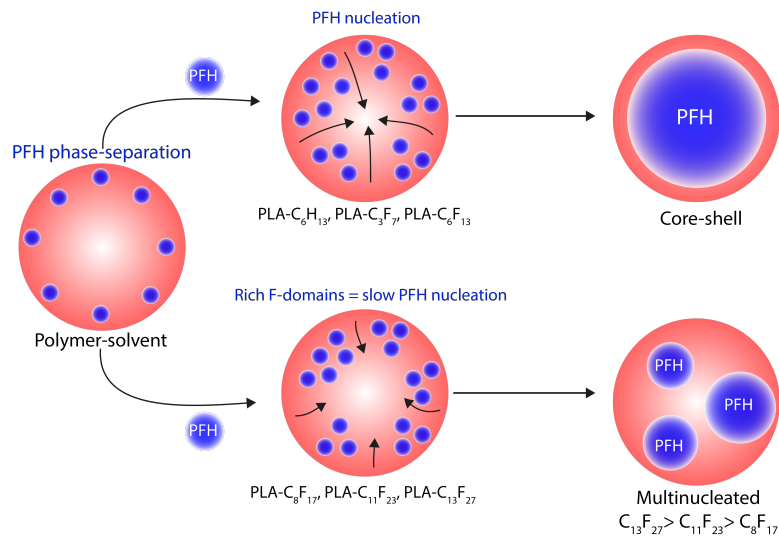


Figure 4. Schematic representation of the perfluorohexane phase-separation and nucleation process in the organic phase constituted by fluorinated polymers of distinct chain lengths.

Therefore, the fluorinated groups generated the formation of more effective fluorophilic domains that are able to interact and, depending on their length, favor a more homogeneous phase-separation and modify the rate of PFH nucleation. For example, although PLA-C₃F₇ effectively interacts with PFH as verified by reduced T₂ values, the perfluorocarbon easily diffuses to the center of the organic drop as observed in the final MC morphology. Instead, in the case of PLA-C₁₃F₂₇, the shell precipitates before the complete fluorocarbon nucleation and causes multiple drops to be deposited inside the rigid polymeric phase. This effect clearly shows that longer fluorinated units generate stronger fluorophilic interfaces within PFH that, according to Rapp *et al.*, are more intense in aqueous system such as SC solutions employed in the formulation (Rapp, Bacher *et al.* 2012).

To further investigate the influence of fluorinated end-groups in PFH stabilization, the total amount of the perfluorocarbon was quantified in freeze-dried MC by ¹⁹F-NMR. Initially, the non-fluorinated polymer, PLA-C₆H₁₃, presented an encapsulation

efficiency of $5.5 \pm 0.1\%$. The employment of fluorinated polymers led to a 2-fold increase in PFH entrapment, attaining $11 \pm 3.0\%$ without any significant distinction based on the length of the fluorinated units. These results evidence their ability to perform preferential interactions with the fluorocarbon and enhance its stabilization inside the organic phase, as displayed in **Figure 5**. Nonetheless, related PLA or PLGA polymers have been recently described to higher amounts of PFH into microcapsules ($\sim 40\%$) (Mousnier, Huang et al. 2014) and such disparity may be related to the fast process of solvent evaporation employed in this work.

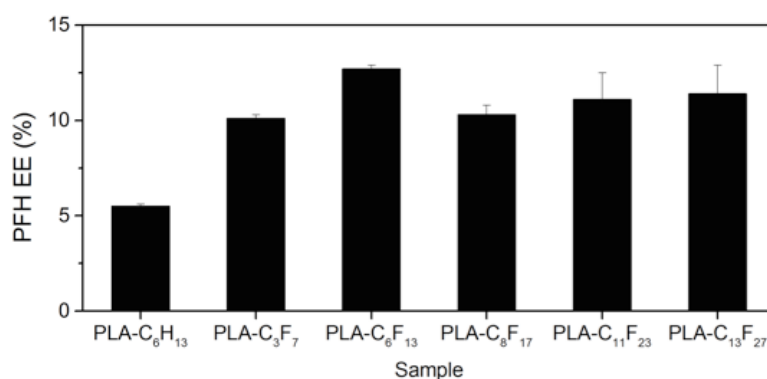


Figure 5. PFH encapsulation efficiency for freeze-dried microcapsules.

3.4 End-group chemistry and F-length influence on MC morphology

To evaluate the end-group chemistry influence in the structure of microcapsules, the samples PLA-C₆H₁₃, PLA-C₃F₇, PLA-C₈F₁₇ and PLA-C₁₃F₂₇ were prepared with varied polymer masses – 12.5, 25, 50 and 100 mg with constant PFH volume of 30 μ L. Initially, the samples prepared with 12.5 mg presented core-shell structures with thin and smooth polymer layers that were predominant for all polymers, independently of end-group chemistry or length as shown in **Figure 6**. The increase of polymer mass to 25 mg altered only the morphology only of MC formulated with PLA-C₁₃F₂₇ to multinucleated capsules ($42 \pm 10\%$) as displayed with white arrows in **Figure 6**. The percentage of such dislocated PFH cores for PLA-C₁₃F₂₇ became more evident for 50 and 100 mg, in which the total amount of multinucleated MC raised from $60 \pm 5\%$ to $91 \pm 3\%$, respectively. The same effect was observed for PLA-C₈F₁₇, as thin-shelled MC are observed in the formulations containing 25 mg and multinucleated morphologies increased from $10 \pm 2\%$ to $56 \pm 7\%$ for 50 and 100 mg, respectively. A similar behavior was observed for MC formulated with the polymer

containing the shortest fluorine end-group, PLA-C₃F₇, as core-shell structures predominated until a polymer mass of 100 mg, in which a total of 45±5% of multinucleated MC were found. In contrast, MC formulated with the non-fluorinated sample, PLA-H₁₃, exhibited core-shell morphologies for all of the tested polymer masses.

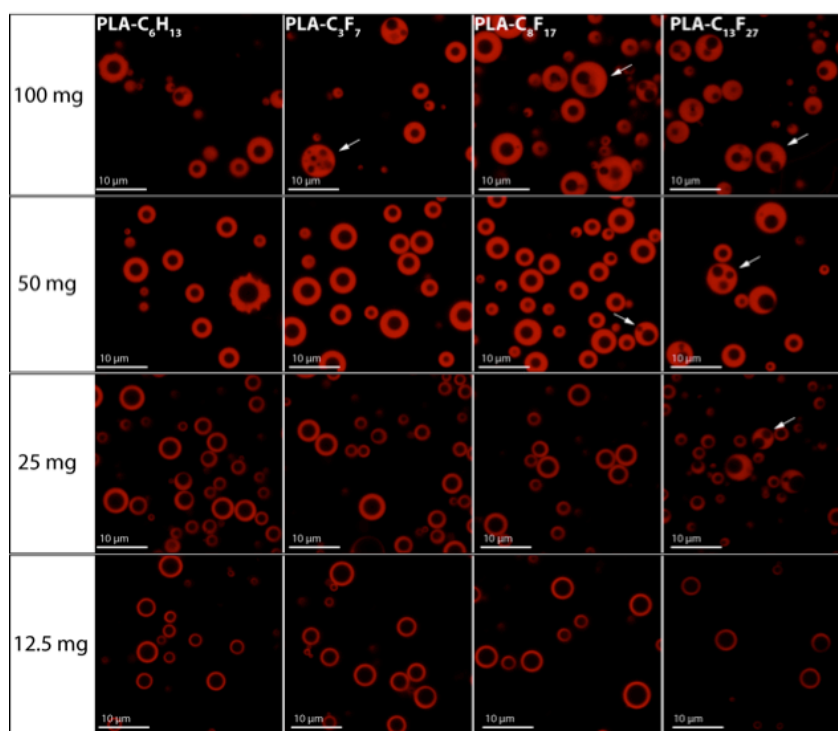


Figure 6. Confocal images of microcapsules formulated in chloroform with non-fluorinated (PLA-C₆H₁₃) and fluorinated (PLA-C₃F₇, PLA-C₈F₁₇ and PLA-C₁₃F₂₇) polymers with varied polymer masses: 100, 50, 25 and 12.5 mg. Scale bar of 10 µm.

A clear effect of the polymer end-group chemistry and fluorinated length was manifested in the capsule's morphology: MC produced with polymers containing F-groups generated the formation of fluorophilic environments that favored PFH wetting when compared to PLA-C₆H₁₃. In addition, the increase in polymer mass favored the formation of richer and stronger fluorophilic domains – in the order of C₃F₇<C₈F₁₇<C₁₃F₂₇ – that altered the polymeric phase dynamics, leading to the formation of binodal boundaries with PFH and reducing its migration rate to the center of the organic drop as previously described.

3.5 MC characterization and ultrasound

The impact of PFH content and capsule's morphology was further evaluated by exposing MC prepared with fixed polymer amounts – 50 mg – to focused ultrasound (FUS). All samples were previously characterized by confocal microscopy according to size and shell thickness as listed in **Table 3**.

Table 3. Size and shell thickness of microcapsules formulated with 50 mg of polymer

Sample	Size (μm)	Shell Thickness (μm)
	Mean \pm SD	Mean \pm SD
PLA-C ₆ H ₁₃	4.2 \pm 1.0	1.0 \pm 0.2
PLA-C ₃ F ₇	4.4 \pm 0.6	1.0 \pm 0.1
PLA-C ₆ F ₁₃	4.8 \pm 1.0	1.1 \pm 0.2
PLA-C ₈ F ₁₇	4.6 \pm 0.8	0.98 \pm 0.1
PLA-C ₁₁ F ₂₃ *	5.2 \pm 1.4	----
PLA-C ₁₃ F ₂₇ *	5.2 \pm 1.0	----

*PLA-F₂₃ and F₂₇ presented more than 50% of multinucleated capsules and thickness values were not measured.

All measurements correspond to observation and analysis of at least 100 microcapsules for each group.

Several PFH droplets were successfully vaporized after the ultrasonic pulse transmission, causing the collapse and fragmentation of the polymeric shell independently of end-group chemistry as shown in **Figure 7**. Nevertheless, MC prepared with the non-fluorinated polymer exhibited a predominant population of intact capsules; in this case, it's probable that the lower PFH content required more intense acoustic pulses to provoke a fast and effective gas-phase nucleation. In contrast, samples formulated with fluorinated polymers displayed a predominant population of ruptured and misshapen capsules. Evidences of shell pores created by the PFH liquid-to-gas transition were found in all samples. Moreover, multinucleated capsules formulated with PLA-C₁₁F₂₃ and PLA-C₁₃F₂₇ offered a larger interfacial area and varied shell thickness that favored the perfluorocarbon vaporization, leading to the formation of several exposed cores. As a result, the employed acoustic pressure – 12.5 MPa – was able to overcome the resistance offered by the thick polymeric shell and provide a sub-pressurized environment that enabled the fluorocarbon to vaporize.

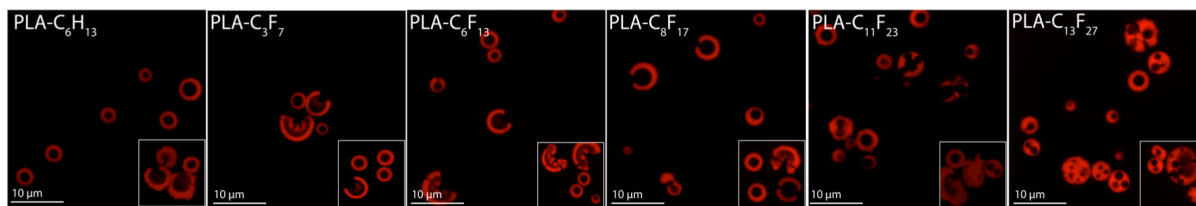


Figure 7. Confocal microscopy images of microcapsules after FUS exposure. The inserts show distinct regions for each sample. Scale bar of 10 μm .

Consequently, the exposure of the capsule's core might be achieved by FUS with dependency on the PFH content and morphology, both induced and controlled by the length fluorinated end-groups. Therefore, those capsules present the potential to promote drug-delivery with submillimetric precision into tissues when irradiated with FUS and improve the localized treatment of a wide variety of diseases. The goal of combining ultrasonic pulses to acoustic-sensitive drug-loaded microcapsules is to increase local drug uptake and ameliorate therapeutical efficiency.

4. Conclusion

We have successfully synthesized and characterized polylactide end-group fluorinated co-polymers for improved fluorophilic-fluorophilic interaction with liquid fluorocarbons. The presence of fluorinated end-groups provided more favorable interfaces with perfluorohexane in organic solution of chloroform with F-group length dependency, as revealed by spin-lattice relaxation measurements. The formation of fluorophilic environments is reflected with improved perfluorohexane encapsulation efficiencies into microcapsules and by modifying the final morphology. Consequently, the microcapsules formulated with fluorinated polymers enabled more effective perfluorocarbon vaporization by high intensity and focused ultrasound and present great potential to be utilized as remotely-triggered drug vehicles.

5. Acknowledgements

This work has been supported by the Région Ile-de-France in the framework of DIM Nano-K and the French National Research Agency (ANR) under grant ANR-10-NANO-06 as part of the "Investissements d'Avenir" program. Institut Galien Paris-Sud is a member of the Laboratory of Excellence LERMIT supported by a grant from

ANR (ANR-10-LABX-33). We are also thankful to Conselho Nacional de Desenvolvimento Científico e Tecnológico (CNPq) for the financial support, to Valerie Nicolas from MIPSIT for helping with confocal experiments and to Prof. Jaísa Soares and Prof. Jens Dittmer for their help with T_1 and T_2 determination.

6. References

Agrawal, A., A. D. Saran, S. S. Rath and A. Khanna (2004). "Constrained nonlinear optimization for solubility parameters of poly(lactic acid) and poly(glycolic acid)—validation and comparison." *Polymer* **45**(25): 8603-8612.

Böhmer, M. R., R. Schroeders, J. A. M. Steenbakkers, S. H. P. M. de Winter, P. A. Duineveld, J. Lub, W. P. M. Nijssen, J. A. Pikkemaat and H. R. Stapert (2006). "Preparation of monodisperse polymer particles and capsules by ink-jet printing." *Colloids and Surfaces A: Physicochemical and Engineering Aspects* **289**(1–3): 96-104.

Boissenot, T., E. Fattal, A. Bordat, S. Houvenagel, J. Valette, H. Chacun, C. Gueutin and N. Tsapis (2016). "Paclitaxel-loaded PEGylated nanocapsules of perfluorooctyl bromide as theranostic agents." *European Journal of Pharmaceutics and Biopharmaceutics* **108**: 136-144.

Chung, T.-W., Y.-Y. Huang and Y.-Z. Liu (2001). "Effects of the rate of solvent evaporation on the characteristics of drug loaded PLLA and PDLLA microspheres." *International Journal of Pharmaceutics* **212**(2): 161-169.

Cosco, D., E. Fattal, M. Fresta and N. Tsapis (2015). "Perfluorocarbon-loaded micro and nanosystems for medical imaging: A state of the art." *Journal of Fluorine Chemistry* **171**: 18-26.

Diou, O., E. Fattal, V. Delplace, N. Mackiewicz, J. Nicolas, S. Meriaux, J. Valette, C. Robic and N. Tsapis (2014). "RGD decoration of PEGylated polyester nanocapsules of perfluorooctyl bromide for tumor imaging: influence of pre or post-functionalization on capsule morphology." *Eur J Pharm Biopharm* **87**(1): 170-177.

Diou, O., E. Fattal, V. Delplace, N. Mackiewicz, J. Nicolas, S. Meriaux, J. Valette, C. Robic and N. Tsapis (2014). "RGD decoration of PEGylated polyester nanocapsules of perfluorooctyl bromide for tumor imaging: Influence of pre or post-functionalization on capsule morphology." *European Journal of Pharmaceutics and Biopharmaceutics* **87**(1): 170-177.

Giuntoli, G., L. Rosi, M. Frediani, B. Sacchi and P. Frediani (2012). "Fluoro-functionalized PLA polymers as potential water-repellent coating materials for protection of stone." Journal of Applied Polymer Science **125**(4): 3125-3133.

Henderson, T. J. (2002). "Quantitative NMR Spectroscopy using coaxial inserts containing a reference standard: Purity determinations for military nerve agents." Analytical Chemistry **74**(1): 191-198.

Kadayakkara, D. K., K. Damodaran, T. K. Hitchens, J. W. M. Bulte and E. T. Ahrens (2014). "F-19 spin-lattice relaxation of perfluoropolyethers: Dependence on temperature and magnetic field strength (7.0-14.1 T)." Journal of Magnetic Resonance **242**: 18-22.

Koda, Y., T. Terashima, A. Nomura, M. Ouchi and M. Sawamoto (2011). "Fluorinated Microgel-Core Star Polymers as Fluorous Compartments for Molecular Recognition." Macromolecules **44**(12): 4574-4578.

Koda, Y., T. Terashima and M. Sawamoto (2015). "Fluorinated microgel star polymers as fluorous nanocapsules for the encapsulation and release of perfluorinated compounds." Polymer Chemistry **6**(31): 5663-5674.

Koda, Y., T. Terashima and M. Sawamoto (2015). "Fluorinated Microgels in Star Polymers: From In-Core Dynamics to Fluorous Encapsulation." Macromolecules **48**(9): 2901-2908.

Krafft, M. P. and J. G. Riess (2015). "Selected physicochemical aspects of poly- and perfluoroalkylated substances relevant to performance, environment and sustainability-Part one." Chemosphere **129**: 4-19.

Lebedeva, N. V., S. N. Sanders, M. Ina, A. P. Zhushma, S. D. Olson, M. Rubinstein and S. S. Sheiko (2016). "Multicore expandable microbubbles: Controlling density and expansion temperature." Polymer **90**: 45-52.

Li, W. X., H. Dong, G. N. Tang, T. Ma and X. D. Cao (2015). "Controllable microfluidic fabrication of Janus and microcapsule particles for drug delivery applications." Rsc Advances **5**(30): 23181-23188.

Mousnier, L., N. Huang, E. Morvan, E. Fattal and N. Tsapis (2014). "Influence of polymer end-chemistry on the morphology of perfluorohexane polymeric microcapsules intended as ultrasound contrast agents." Int J Pharm **471**(1-2): 10-17.

Pisani, E., E. Fattal, J. Paris, C. Ringard, V. Rosilio and N. Tsapis (2008). "Surfactant dependent morphology of polymeric capsules of perfluorooctyl bromide: influence of polymer adsorption at the dichloromethane-water interface." J Colloid Interface Sci **326**(1): 66-71.

Pisani, E., E. Fattal, J. Paris, C. Ringard, V. Rosilio and N. Tsapis (2008). "Surfactant dependent morphology of polymeric capsules of perfluorooctyl bromide: Influence of polymer adsorption at the dichloromethane-water interface." Journal of Colloid and Interface Science **326**(1): 66-71.

Pisani, E., N. Tsapis, B. Galaz, M. Santin, R. Berti, N. Taulier, E. Kurtisovski, O. Lucidarme, M. Ourevitch, B. T. Doan, J. C. Beloeil, B. Gillet, W. Urbach, S. L. Bridal and E. Fattal (2008). "Perfluorooctyl Bromide Polymeric Capsules as Dual Contrast Agents for Ultrasonography and Magnetic Resonance Imaging." Advanced Functional Materials **18**(19): 2963-2971.

Rapp, H. M., S. Bacher, A. Ahrens, W. Rapp, B. Kammerer, G. U. Nienhaus and W. Bannwarth (2012). "Attachment of Proteins to Surfaces by Fluorous-Fluorous Interactions Restoring Their Structure and Activity." Chempluschem **77**(12): 1066-1070.

Shaffer, T. H., R. Foust, 3rd, M. R. Wolfson and T. F. Miller, Jr. (1997). "Analysis of perfluorochemical elimination from the respiratory system." J Appl Physiol (1985) **83**(3): 1033-1040.

Singh, A., A. K. Naskar, D. Haynes, M. J. Drews and D. W. Smith (2011). "Synthesis, characterization and surface properties of poly(lactic acid)-perfluoropolyether block copolymers." Polymer International **60**(3): 507-516.

Singh, R., G. A. Hussein and W. G. Pitt (2012). "Phase transitions of nanoemulsions using ultrasound: Experimental observations." Ultrasonics Sonochemistry **19**(5): 1120-1125.

Torza, S. and S. G. Mason (1970). "Three-phase interactions in shear and electrical fields." Journal of Colloid and Interface Science **33**(1): 67-83.

Twum, E. B., E. F. McCord, D. F. Lyons, P. A. Fox and P. L. Rinaldi (2014). "Characterization of end groups and branching structures in copolymers of vinylidene fluoride with hexafluoropropylene using multidimensional NMR spectroscopy." European Polymer Journal **51**: 136-150.

Watanabe, T., Y. Kimura and T. Ono (2013). "Microfluidic Fabrication of Monodisperse Polylactide Microcapsules with Tunable Structures through Rapid Precipitation." Langmuir **29**(46): 14082-14088.

Supplementary Information

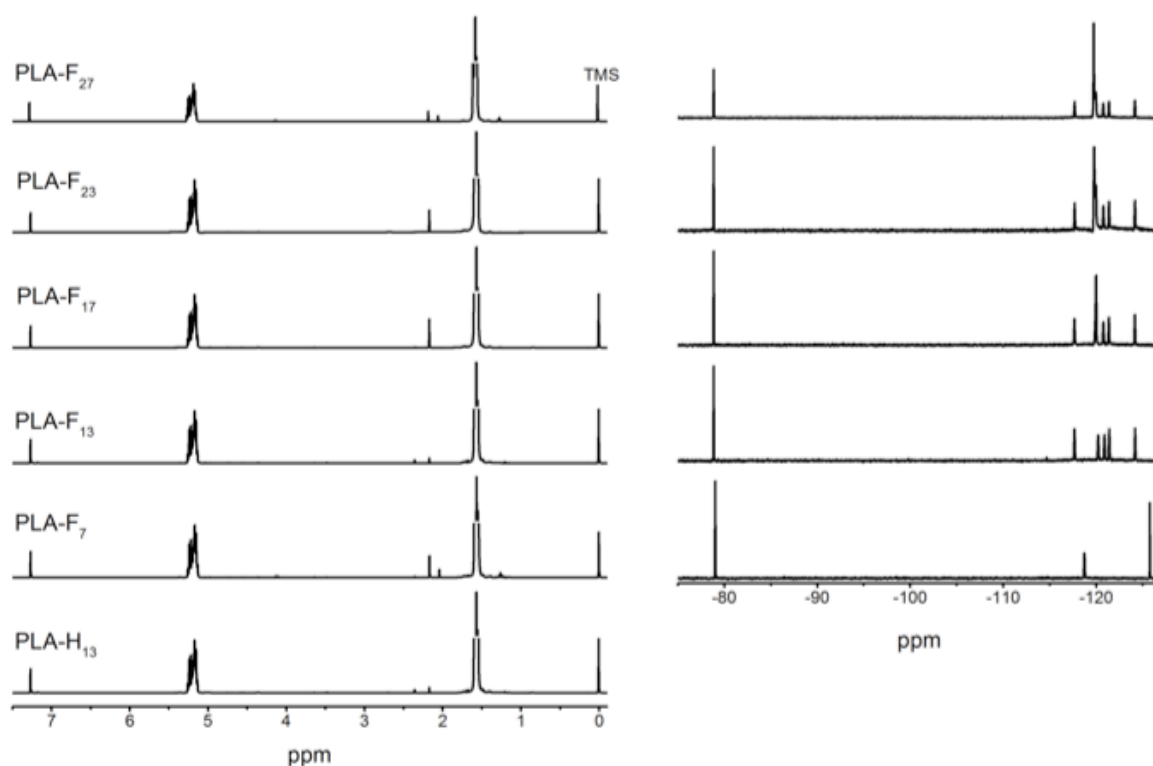


Figure S1. ^1H (left) and ^{19}F -NMR spectra (right) of all synthesized polymers. All samples were dissolved in CDCl_3

Table S1. Average number molecular weight (M_n) obtained by SEC and ^{19}F -NMR and dispersity of all synthesized polymers.

Polymer	M_n SEC $\times 10^3$ ($\text{g}\cdot\text{mol}^{-1}$)	Dispersity \bar{D}	M_n ^{19}F -NMR $\times 10^3$ ($\text{g}\cdot\text{mol}^{-1}$)
PLA-C ₆ H ₁₃	22±1.7	1.4	-----
PLA-C ₃ F ₇	24±2.0	1.4	17±1.0
PLA-C ₆ F ₁₃	26±2.5	1.3	17± 1.2
PLA-C ₈ F ₁₇	27±1.7	1.4	14.5± 2.3
PLA-C ₁₁ F ₂₃	23±2.2	1.3	13± 3.0
PLA-C ₁₃ F ₂₇	24±1.0	1.4	14±2.4

Table S2. Spin-lattice relaxation (T_1) values of correspondent ^{19}F resonances for samples dissolved in deuterated chloroform with and without perfluorohexane. All results are expressed in seconds \pm standard deviation of curve fitting with correspondent r^2 value.

Sample	Resonance	$T_1(\text{s})$			
		CDCl_3	r^2	CDCl_3+PFH	r^2
PLA-C ₃ F ₇	^a CF ₂	1.29±0.03	0.998	1.31±0.05	0.998
	^e CF ₂	1.68±0.03	0.999	2.35±0.10	0.998
	CF ₃	2.08±0.10	0.998	3.00±0.06	0.998
PLA-C ₈ F ₁₇	^a CF ₂	0.63±0.11	0.993	1.68±0.17	0.989
	^b CF ₂	0.86±0.06	0.996	2.65±0.10	0.989
	^c CF ₂	0.61±0.08	0.996	2.44±0.14	0.998
	^d CF ₂	0.70±0.02	0.999	1.05±0.07	0.993
	^e CF ₂	1.21±0.03	0.999	----	----
	CF ₃	1.83±0.03	0.999	----	----
PLA-C ₁₃ F ₂₇	^a CF ₂	0.46±0.17	0.989	1.07±0.12	0.989
	^b CF ₂	1.10±0.11	0.988	2.67±0.13	0.998
	^c CF ₂	0.73±0.13	0.987	2.70±0.23	0.998
	^d CF ₂	0.83±0.12	0.991	1.17±0.13	0.985
	^e CF ₂	1.23±0.15	0.980	----	----
	CF ₃	1.74±0.08	0.996	----	----

Chapter 5

General Discussion

General Discussion

The main goal of this thesis is to develop and characterize distinct theranostic systems comprising both gaseous and liquid perfluorocarbon cores. As fully fluorinated perfluorocarbons are characterized by inertness and are neither hydrophilic nor hydrophobic, their enhanced stabilization into polymer or phospholipid-based systems was considered as a key factor to provide higher imaging quality as well as ultrasonic sensitiveness for triggering drug-release in targeted tissues. In this discussion, the PFC stabilizing strategies utilized are confronted against the approaches described in the literature. Furthermore, the advantages and disadvantages of gas and liquid PFC-filled systems are compared regarding its theranostic potential.

Nonetheless, these two different strategies might be complementary and synergically enhance the effectiveness of chemotherapeutics: as the gas core resonates at the megahertz frequency range, it may provide useful images of cancerous tissues and locally release therapeutics triggered by inertial cavitation. On the other hand, the nanocapsules present the ability to passively accumulate in solid tumors and allow the imaging of the tissue's inner structure, where a focused ultrasound beam may induce the release of drugs, aiming the treatment of deep cancer regions, distant from the healthy vasculature.

1.1 Gas-core microvesicle stabilization and functionalization

The second chapter of this thesis has explored the potential of the polysaccharide chitosan to effectively coat phospholipid-based microvesicles bearing a fluorinated gas core. As previously reported, a consequent response was manifested as more enduring perfluorocarbon persistence with chitosan performing a dual effect, stabilizing the phospholipid barrier and also providing a plausible platform for drug accumulation and release. Finally, an evolution towards the formulation of the current gas-based UCA is proposed. Nevertheless, many factors must still be considered for optimal development and application of such systems.

1.2 Formulation

The prolonged circulation and evasion of the immune system fast clearance is an important issue of study. With the intent to enhance the lifetime of microvesicles in the bloodstream, the fast complement activation must be hindered. Although chitosan of distinct molar masses is reported to enhance the stability of many nanoparticles into the bloodstream, its amines groups are prone to undergo covalent interaction with the C3b fragment and active the complement cascade (Moghimi, Andersen et al. 2011) (Ishak, Awad et al. 2013). To avoid the fast clearance, a partial chitosan modification with PEG chains can be envisioned by offering interesting technological advantages, combining the structural stability of the polysaccharide with the more hydrophilic polymeric brushes. In fact, some studies evidenced the role of covalent and non-covalent PEG-chitosan composites in reducing NP opsonization, phagocyte uptake and enabled specific drug delivery to cells in a weakly acidic environment (Amoozgar, Park et al. 2012) (Corbet, Ragelle et al. 2016). Nonetheless, additional studies would be necessary to ensure the system's furtivity, since PEG moieties might also participate in interactions with proteins and rapidly cause complement activation (Bloustine, Virmani et al. 2006). In addition, increased ratios of PEG are related to reduce the ultrasonic scattered pressure for decreasing the shell viscosity (Cool, Geers et al. 2013, Hosny, Mohamedi et al. 2013).

1.3 Theranostic potential

1.3.1 Ultrasound Imaging

UCA benefit from its micrometer size range and the gas-core ability to resonate within the megahertz range frequency utilized in clinical ultrasound (2-10 MHz) to greatly enhance the scattered echo compared to nanometric agents. As demonstrated with B-mode imaging, the relative compressibility provoked by chitosan onto the phospholipid layer is not significant to alter imaging quality with the 1.5-3.1 MHz range. Comparatively, microcapsules (~6 μm) constituted by rigid PLGA shells and a liquid PFC (PFOB) core display lower elasticity according to the polymeric layer thickness and, consequently, respond with less intense echogenicity (only 15 dB at 50 MHz for 50 $\text{mg}\cdot\text{mL}^{-1}$ samples). Similar results are observed for PFH microcapsules (PLGA/ Fe_3O_4), exhibiting only a minimal B-mode enhancement with dependency on concentration (Pisani, Tsapis et al. 2008) (Sun, Zheng et al. 2012) (Sarrazin, Tsapis et al. 2016). Thereby, the imaging potential of gaseous-core microvesicles is still unmatched compared to liquid PFCs or rigid-polymeric layers.

Unfortunately, UCA exhibits low acoustic response at the nanoscale – as this intensity is relative to the 6th power according to the Rayleigh model (Eq. 7), nanometric materials are poor US scatters – even the ones stabilized by compressible phospholipid shells or gaseous PFCs. For example, Huynh et al. developed porphyrin-phospholipid shelled UCA containing a C_4F_{10} gas core with the ability to shift from a micro to nanometric size dispersion (~3 μm to ~400 nm); As the microvesicles produced intense echoes, the conversion to nanovesicles by 1 MHz (2 $\text{W}\cdot\text{cm}^{-2}$) pulsed US hindered any significant contrast *in vivo* (Huynh, LeungBen et al. 2015). Although some authors describe a successful formulation of intense echogenic nanovesicles several technological advances are still required to achieve stable and US sensitivity as compared to micrometer-range systems. This limitation also prevents fast and cheap triage of the EPR effect heterogeneities to select which patients are more responsive to treatments based on current chemotherapeutics or nanomedicines (Mura and Couvreur 2012).

1.3.2 Drug uptake and release mediated by ultrasound

One of the greatest disadvantages of gas-core UCA relies in the lack of effective compartments for drug accumulation. As a result, many strategies aim the structural modification of surface components to provide additional interfaces for drug intercalation. For instance, Lentacker *et al.* proposed anchoring doxorubicin-loaded liposomes into the surface of C_4F_{10} microbubbles to provide the uptake of higher drug amounts, allow the transport of a wider drug variety, protect them from degradation and permit liposome extravasation into leaky vasculature induced by ultrasound (**Figure 1**) (Lentacker, Geers et al. 2009). Further experiments observed an *in vivo* 3.7-fold increase of drug release 1h after 1 MHz ultrasonic exposure (Cool, Geers et al. 2013).

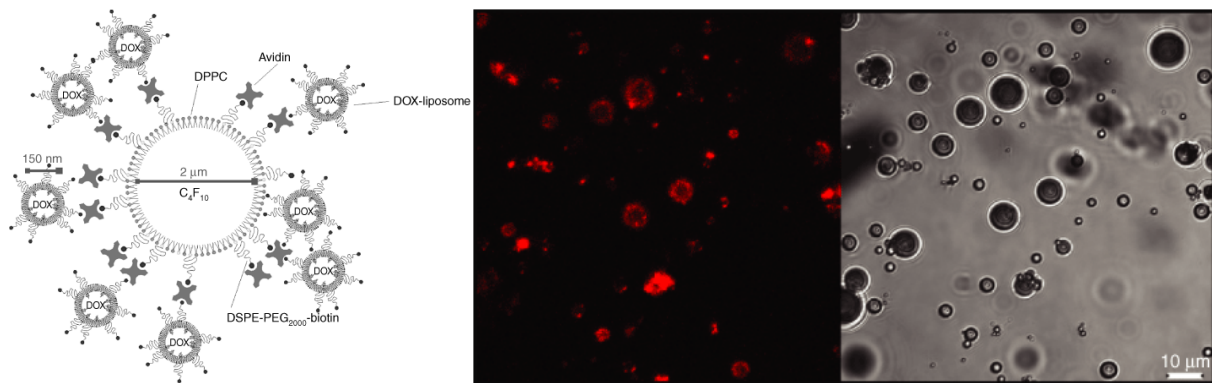


Figure 1. Schematic representation of drug-loaded liposomes coupled with microbubbles. Biotinylated lipids were employed to link both systems via avidin anchoring (left). The doxorubicin loading was observed by CLSM and compared with transmission images (middle and right). Adapted from Lentacker *et al.* (Lentacker, Geers et al. 2009).

More simple and straightforward approaches have also been described, such as the utilization of negatively charged head-group phospholipids (e.g. DSPG) for electrostatic interaction with doxorubicin. In this report, the authors observed a significant tumor inhibition when the system was exposed to ultrasound, suggesting effective drug release nearby the targeted tissue. Nevertheless, only 2.5% of the drug content reached the tumor bed, indicating that the sonoporation effects were limited to a fast – and possibly complete – release of doxorubicin induced by inertial cavitation. In addition, the size range of such UCA prevented more efficient drug diffusion into the tumor (Abdalkader, Kawakami et al. 2015).

Recently, UCA composed of charged phospholipids were employed to anchor nucleic acids and increase transfection rates by the sonoporation therapy (Tsunoda, Mazda et al. 2005) (Yin 2013) (Chertok 2016). Gene therapy is a promising alternative in the treatment of several diseases, including inherited disorders, viral infections and cancers. However, the lack of adapted and efficient gene vectors (for DNA, mRNA, microRNA and small interfering RNA) represents a major obstacle towards gene therapy. Since such small interfering RNA or DNA plasmids are rapidly degraded or captured by macrophages in the blood and, therefore, they require adequate transport into the desired cell (Yang, Cai et al. 2015). As previously observed, a synergic effect among the oscillatory UCA motion – induced by high pressure and low US frequencies – and gene permeation into cells has offered an interesting option to viral vectors, which raise safety concerns for its carcinogenesis, immunogenicity and off-targeted release (Shapiro, Wong et al. 2016). However, the presence of abundant surface electrostatic charges may disturb the stability of phospholipid monolayers and generate formulations with low *in vivo* and shelf stability (Borden, Martinez et al. 2006).

The use of chitosan as an interfacial coating material of microbubbles introduces the advantage to potentiate transfection rates and drug or nanomedicine loading capability to the current generation of gas-core systems. Chitosan is one of the most interesting vectors utilized for transfection for its ability in forming complexes with negatively charged molecules with high loading capability. This polysaccharide forms entanglements with DNA or RNA with dependency on the molar mass and deacetylation degree (DD): according to Liu *et al.*, chitosan comprising DD higher than 84% and M_w in the range of 64 – 170 kDa generate strong and stable complexes with siRNA (Liu, Howard et al. 2007). In addition, chitosan is widely investigated to facilitate endosomal escape and deliver greater siRNA payloads whereas PEGylated surfaces are correlated with poor transfection rates (Van Woensel, Wauthoz et al. 2016) (Vandenbroucke, Lentacker et al. 2008).

Apart from solely acting as a vector, chitosan might be also employed to modify the rate of content released during ultrasonic pulses. Liao *et al.* aimed this goal by modifying the surface of albumin shelled UCA with chitosan. According to pH variations and acoustic pressures in the order of 0.26 MPa, the authors reported distinct release rates of minoxidil – electrostatically anchored with chitosan layer – due to the different conformations assumed by the polymer aided by the mechanical

cavitation of the microbubbles (Liao, Lu et al. 2016). Such interesting performance may be explored to provide further control on the release of sustained amounts of drug nearby affected areas. This is, in fact, an important parameter to maximize the drug's cytotoxic effect: Yu *et al.* analyzed the release rate of microbubbles-loaded with doxorubicin liposomes and observed that the cellular survival rates were reduced only when stable cavitation was induced by low power ultrasonic exposure (Yu, Chen et al. 2016). In this scenario, higher amounts of drug were available due to a sustained release, whereas the rapid microbubble collapse generated by inertial cavitation caused low drug release and, consequently, poor cytotoxicity towards murine squamous cell carcinoma cell line.

1.4 Limitations

Although the C₄F₁₀ microvesicles coated with chitosan present imaging ability and potential to anchor charged drugs along its outer polymeric layer, this system also displays two important limitations: the first is related to its size-range, which restricts the accessibility only to structures located next to large blood vessels. As a result, both imaging and delivery of drug payloads into solid tumors is hindered, allowing only the treatment of peripheral cells by focused ultrasound. Second, the stability is a major issue of consideration because the *in vivo* lifetime of related microbubbles is less than 5 minutes; although chitosan might effectively increase the system's persistence in the bloodstream, the diffusibility of the perfluorinated gas-core is still a predominant factor that reduces the stability of the microvesicles.

An alternative to these issues may rely on the employment of liquid PFCs; as previously reported, easy one-step or mild production protocols can generate stable nanoemulsion droplets at the nanoscale that are more adapted to passively target tumor tissues by the EPR effect (Pisani, Tsapis et al. 2006). Many liquid PFCs were already utilized to augment the stability of gaseous UCA by reducing the surface tension between the phospholipid layer and the C₄F₁₀ core, though maintaining a micrometer size distribution (Abou-Saleh, Peyman et al. 2016). Their use favored the formation of liposomes at the nanoscale, but also displayed low entrapment efficiencies and laborious purification steps. Thereby, we have explored the potential of fluorinated polymers to form rigid-shells to enhance PFC inclusion into nanocapsules.

2. Nano and microcapsules

The third and fourth sections of this thesis have introduced the utilization of end-group fluorinated polymers to improve the stability of perfluorohexane and generate ultrasound-responsive nano and microcapsules. The synthesis of partly fluorinated PLA polymers is based on the limitations of reference polymer materials such as polylactide (PLA)/ poly(lactide-co-glycolide) (PLGA) for the entrapment of low boiling point liquid PFCs (e.g. perfluoropentane, perfluorohexane and perfluoroheptane). Although previous reports successfully employed PFH in ^{19}F -MRI imaging and explore its phase-transition to release therapeutics, the amounts of PFC incorporated remains low and such nanostructured systems are not fully adapted to produce good quality ultrasonic images, ^{19}F contrast or release high drug contents (Srinivas, Cruz et al. 2010) (Li, Wang et al. 2014). Therefore, the proposed end-group fluorine functionalization is considered to improve PFC stabilization and acoustic sensitivity.

The nanocapsules developed in this work display a more suitable interface for compartmentalization and stabilization of fluorophilic components. High doses of chemotherapy agents can be entrapped in the polymeric shell of the NC, which might passively target cancer tissues and release the drug content during ultrasound exposure. This approach represents an important advance compared to the high doses of free drugs that are administered intravenously in cancer patients, affecting all tissues and causing numerous side effects. Therefore, a more homogeneous response in patients that present the EPR effect and an increased therapy efficacy might be envisioned. Despite all, several characterizations are still required and numerous challenges must be overcome to translate this technology into clinical practice. In this section, the impact of the fluorophilic domains during the formulation of nano and microcapsules is further discussed. Additionally, many technical difficulties and further observations are presented and confronted against the literature with the intent to pinpoint required improvements or limitations to the use of the proposed system.

2.1 Interfacial behavior of fluorinated polymers

The assessments of the fluorinated group's behavior at the polymer/PFH interface constituted one of the main challenges faced during the characterization stage. As reported in the 4th chapter, a constant-volume PFH drop formed in an organic phase of CHCl_3 containing the polymers did not show any decrease in the surface tension values compared to the solvent itself or non-fluorinated polymers. We have further analyzed the behavior of the synthesized polymers by comparing the interfacial surface tension of solutions prepared in dichloromethane (CH_2Cl_2), a more polar and also a good solvent for PLA (Hildebrand parameter of $19.8 \text{ MPa}^{0.5}$) (Agrawal, Saran et al. 2004). As previously observed in CHCl_3 , no specific adsorption of the polymers at the PFH-solvent interface was observed by dissolving the polymers in CH_2Cl_2 (**Table 1**). In this case, the interfacial tension increased 2-fold, which suggests that PFH spreads better on CHCl_3 than on CH_2Cl_2 . We have also analyzed diluted polymer solutions (for PLA- C_3F_7 and PLA- $\text{C}_{13}\text{F}_{27}$) down to 0.1 mg.mL^{-1} to avoid the formation of aggregates, however, the interfacial tension was the same as the pure solvent for all assays.

Table 1. Interfacial surface tension at the perfluorohexane/chloroform and perfluorohexane/dichloromethane interfaces with 25 mg.mL^{-1} of polymer.

Polymer	PFH/polymer CHCl_3 (mN.m^{-1})	PFH/polymer CH_2Cl_2 (mN.m^{-1})
PLA- C_6H_{13}	3.0 ± 0.5	6.2 ± 0.5
PLA- C_3F_7	3.0 ± 0.3	6.1 ± 0.7
PLA- C_6F_{13}	3.0 ± 0.5	6.2 ± 0.4
PLA- C_8F_{17}	3.1 ± 0.4	5.9 ± 0.4
PLA- $\text{C}_{11}\text{F}_{23}$	3.0 ± 0.3	5.9 ± 0.3
PLA- $\text{C}_{13}\text{F}_{27}$	3.1 ± 0.4	6.1 ± 0.4

The free solvents exhibited values of 3.2 ± 0.3 for CHCl_3 and 6.0 ± 0.3 for CH_2Cl_2

Explanations for the lack of surface activity during the interfacial tension experiments are attributed to three main factors: (1) the loosely and flexible conformation acquired in CHCl_3 or CH_2Cl_2 . Indeed, SEC analysis in CHCl_3 revealed a Mark-Houwink α exponent of ~ 0.7 for all polymers – in agreement with (Schindler and Harper 1979) and (Tonelli 2014) – that indicates randomly distributed (fluorinated)-PLA chains in solution. Because of such random coil configuration in both solvents, the PLA segments might interfere in the F-groups dynamics by generating steric hindrances and, ultimately, reducing their exposure to PFH. (2) The

low mass ratio of fluorinated groups compared to the PLA chain and the employment of good solvents for the polymer backbone. (3) The low fluorine polarizability; as F-F interactions are characterized by low attractive forces, an effective disorganization in the system is required so the fluorinated domains might get into contact and be excluded from the other phases (Berger, Resnati et al. 2011). Thereby, it is the rearrangement of water or organic molecules that induces the packing between fluorinated species, defined as “fluorophobic effect” (Horváth 1998). In our case, both solvents (CHCl_3 and CH_2Cl_2) display very weak intermolecular van der Waals attractions and, thus, a low driving force to provoke fluorine compartmentalization (Allen, Wood et al. 2013). These features result in a weak potential to provoke conformational reorganization based on the higher solubility of F-groups within a liquid perfluorocarbon phase as well as a consequent interfacial adsorption.

We have also synthesized polymers with an M_n of $2.000 \text{ g}\cdot\text{mol}^{-1}$ to reduce the influence of the polymeric backbone towards the F-units and, even in this case, no interfacial adsorption is observed for the short or long F-chains (C_3F_7 and $\text{C}_{13}\text{F}_{27}$) in such experimental setup (**Figure 2**). This behavior is supported by the absence of surface activity of non-modified PLGA and PLA polymers dissolved in similar solvents, which causes no significant adsorption at the perfluorohexane interface ($\sim 5.5 \text{ mN}\cdot\text{m}^{-1}$ for PLA dissolved in dichloromethane) or at aqueous interfaces (Mousnier, Huang et al. 2014) (Babak, Auzely et al. 2007).

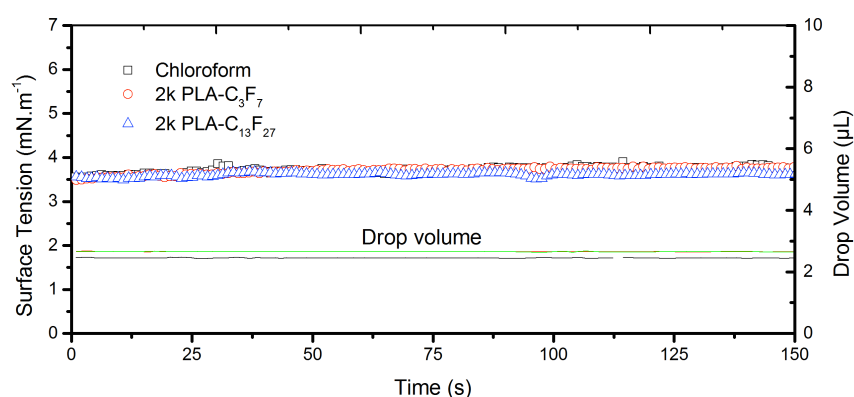


Figure 2: Interfacial surface tension profile at the PFH/polymer interface for 2.000 g/mol $\text{PLA-C}_3\text{F}_7$ (red circles) and $\text{PLA-C}_{13}\text{F}_{27}$ (blue triangles) dissolved in chloroform (black squares). The polymer concentration was fixed at $25 \text{ mg}\cdot\text{mL}^{-1}$. The PFH drop volume was kept constant at $2.2 \text{ }\mu\text{L}$ along the experiment (lines).

Comparatively, water-soluble partly fluorinated surfactants are reported to reduce the surface tension of perfluorocarbons, indicating that the strong hydrophilic interactions of polar head-groups may play an important role in excluding the F domains towards the PFC phase. For example, Astafyeva *et al.* synthesized fluorinated surfactants that caused a clear decrease of PFOB-water interfacial tension, from 48.7 to ~ 11 mN.m⁻¹ by using C₆F₁₃ and C₈F₁₇ end-groups (Astafyeva, Somaglino *et al.* 2015). Many fluorinated surfactants are particularly employed to improve the stability of PFC droplets, such as Zonyl[®] (Zarzar, Sresht *et al.* 2015) and Krytox[®] (Duncanson, Arriaga *et al.* 2014) in the production of microcapsules. Nonetheless, such emulsion-based materials are disadvantageous for intravascular administration for their propensity to coalesce due to Ostwald ripening or molecular diffusion *in vivo*. In addition, the toxicity of these marketed fluorinated surfactants has not been fully evaluated *in vitro* and *in vivo*.

Attempts to improve the surface activity of polymers towards fluorophilic interfaces are, however, under current investigation. In fact, a newly synthesized triblock polymer (Thesis subject of Sophie Houvenagel at Université Paris-Saclay) successfully allowed PFH-CHCl₃ interfacial tension; such polymers are structurally distinct and contain hydrophilic PEG moieties and long pendant chains of heptadecafluorodecyl methacrylate, both end-capped and linked to a main PLA chain (PEG-PLA-PFMA_n – n correspond to the number of methacrylate units containing (CF₂)₇CF₃ groups). These long and pendant F-groups units decreased the PFH surface tension from 3.1 mN.m⁻¹ in pure chloroform to 1.5 and 1.3 mN.m⁻¹ for polymers containing 5 and 10 methacrylate fluorinated units, respectively (**Figure 3**). As a result, such materials represent an interesting potential to stabilize PFCs in organic media. Additionally, they display the advantage of generating capsules or structures already covered by PEG moieties.

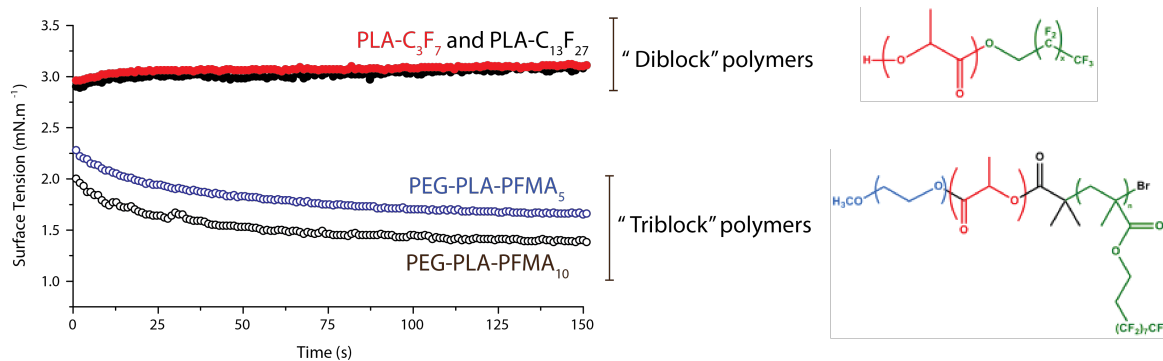


Figure 3: Comparison of the interfacial surface tension profile at the PFH/polymer interface of PLA-C₃F₇ (dark circle), PLA-C₁₃F₂₇ (red circle), PEG-PLA-PEG-PLA-PFMA₅ (blue open circle) and PEG-PLA-PFMA₁₀ (dark open circle).

2.2 Polymer dynamics

Although no surface activity was observed for the fluorinated polymers in organic solution, the solvent-evaporation method used to produce both micro and nanocapsules is a dynamic process associated with transitory interfacial instabilities (Foster, Dorfman et al. 2010). In fact, the resultant higher entrapment efficiency and the distinct morphologies observed for both NC and MC are strong indicatives that a certain extent of fluororous interactions occurred along the process. During the organic solvent elimination, the PLA chain gradually loses its solubility and the polymeric network undergoes constant and less favorable molecular reorganizations (Li, Dong et al. 2015). As the solvents (CHCl₃ or CH₂Cl₂) evaporate faster than PFH, it is possible that the solubility of the fluorinated end-groups decreases more slowly compared to the PLA due to partial solvation in the PFC phase. In this scenario, the fluororous interactions might have provoked conformational rearrangements that facilitated a subsequent compartmentalization of PFH.

A great attention was devoted to investigate the ability of the fluorinated polymers to interact with PFCs by analyzing the impact of the presence of PFH in organic solvents in the dynamics of the fluorinated groups. Because of the difficulty in characterizing the system during the solvent-evaporation process, we performed ¹⁹F-NMR relaxometry studies in polymer solutions with and without PFH to assess the end-groups behavior. Although this condition represents the system just before emulsification, the decreased segmental mobility as verified by T₂ reduction of the CF₃ resonances of fluorinated end-groups (chapter 4) in the presence of the

perfluorocarbon can be related with a plausible higher interaction among the fluorophilic components as already observed by (Koda, Terashima et al. 2015). An enhanced PFH sequestration, as well as an altered F-group conformation during the solvent evaporation process might be compared to the behavior of partly-fluorinated star polymers: such water-soluble and highly fluorinated materials present the ability to remove PFC contaminants from aqueous environments by fluorous interactions and T_2 analysis invariably resulted in decreased local fluorine mobility (Preuschen, Menchen et al. 1999) (Koda, Terashima et al. 2014).

Initially, we evaluated the segmental mobility of the fluorinated chain in $CDCl_3$ and CD_2Cl_2 by spin-lattice (T_1) relaxation. For these analyses, polymers with 2.000 g.mol^{-1} were used to increase the spectral density and facilitate the detection of fluorine resonances at 25 mg.mL^{-1} (**Table 2**). The T_1 values of such polymers displayed similar relaxation rates as presented by the $20.000 \text{ g.mol}^{-1}$ samples in $CDCl_3$ (chapter 4); when CD_2Cl_2 was employed as solvent, a slight increase of T_1 was observed – particularly for the CF_3 resonances – indicating that different conformations of the PLA chain acquired in each solvent can modify the relaxation rate of the fluorinated chains. As the spin-lattice of macromolecules is predominantly dependent on the dipole-dipole relaxation mechanism, the fluorine relaxation rate has a strong dependence on the internuclear distances of 1H and ^{19}F and, thus, the proximity of polymeric PLA domains as well as adjacent fluorinated groups are related to the local segmental mobility (**Equation 1**) (Claridge 2009).

$$\frac{1}{T_1} = \frac{1}{10} \frac{\gamma_F^2 \gamma_H^2 \hbar^2}{r_{FH}^6} \tau_c \left(\frac{3}{(1 + \omega_F^2 \tau_c^2)} + \frac{1}{(1 + (\omega_F - \omega_H)^2 \tau_c^2)} + \frac{6}{(1 + (\omega_F + \omega_H)^2 \tau_c^2)} \right)$$

Equation 1. γ_F and γ_H are the gyromagnetic ratios of fluorine and hydrogen, respectively. \hbar is the Planck's constant divided by 2π ω_F and ω_H are the resonance frequencies of fluorine and hydrogen, respectively and τ_c is the tumbling rate.

Table 2. Spin-lattice relaxation (T_1) values for 2.000 g.mol⁻¹ of correspondent polymer fluorine resonances for samples dissolved in deuterated chloroform and deuterated dichloromethane with or without perfluorohexane. All results are expressed in seconds \pm standard deviation of curve fitting. n=2.

Sample	Resonance	T_1 (s)			
		CDCl ₃	CDCl ₃ +PFH	CD ₂ Cl ₂	CD ₂ Cl ₂ +PFH
PLA-C ₃ F ₇	^a CF ₂	1.25±0.05	1.30±0.01	1.91±0.13	1.54±0.01
	^e CF ₂	1.61±0.05	1.61±0.01	2.55±0.07	1.86±0.01
	CF ₃	2.06±0.06	2.30±0.05	3.47±0.09	2.13±0.01
PLA-C ₈ F ₁₇	^a CF ₂	0.69±0.04	0.60±0.02	0.70±0.02	0.80±0.02
	^b CF ₂	1.05±0.05	1.11±0.03	1.08±0.03	1.58±0.03
	^c CF ₂	0.75±0.04	0.81±0.02	0.79±0.03	0.84±0.06
	^d CF ₂	0.72±0.04	0.87±0.02	0.82±0.02	0.94±0.05
	^e CF ₂	1.34±0.08	----	1.32±0.03	----
	CF ₃	1.89±0.03	----	2.05±0.01	----
PLA-C ₁₃ F ₂₇	^a CF ₂	0.52±0.06	0.50±0.18	0.48±0.05	0.53±0.05
	^b CF ₂	0.88±0.03	2.04±0.17	0.99±0.03	1.14±0.01
	^c CF ₂	0.50±0.04	1.59±0.10	0.81±0.02	0.57±0.01
	^d CF ₂	0.52±0.04	0.84±0.17	0.61±0.02	0.66±0.03
	^e CF ₂	1.10±0.04	----	1.27±0.02	----
	CF ₃	1.72±0.01	----	2.43±0.02	----

After adding PFH, the assays were repeated for all samples. Those dissolved in CDCl₃ showed a discrete increase in T_1 values (very similar to the 20.000 g.mol⁻¹ polymers reported in chapter 4) and the same behavior was observed for PLA-C₈F₁₇ and PLA-C₁₃F₂₇ in CD₂Cl₂. Only PLA-C₃F₇ dissolved in CD₂Cl₂ exhibited a global T_1 reduction. Therefore, we consider two main mechanisms able to produce the relaxation of the fluorinated end-groups as identified by the T_1 measurements: (1) the interaction with PFH based on the higher solubility in a fluorophilic solvent and (2) the distinct polymeric conformations assumed in such media, in which the polymer is expected to present low solubility.

However, based on this observations, its not possible to consider that the ¹⁹F resonances are more effectively relaxed in CDCl₃ (with or without PFH) or suggest a more packed polymer conformation around the fluorinated chains compared to the same system in CD₂Cl₂. Unfortunately, a straightforward assessment of group mobility only by analyzing the spin-lattice results represented a major problem due to the high molecular weight of the polymers. Normally, such large molecules present low tumbling rates in organic solution and T_1 may either

decrease or increase according to the polymer's molecular weight and tumbling rate in solution (τ_c) (**Figure 4**). Therefore, the determination of T_2 – a measurement that is more specific to local motion processes – is also required to fully characterize the end-group dynamics and also the segmental effect caused by the addition on PFH.

According to the discrepancy of T_1 and T_2 values for the same polymer (2.08s and 540 μ s for the CF_3 resonance of PLA- C_3F_7 in CDCl_3), they indeed suggest that the polymers present low τ_c and the spin-spin relaxation measurements are required to confirm those obtained by T_1 relaxation. Moreover, the direct T_1 and T_2 determination of PFH in polymer solution represents an interesting strategy to assess its interactive ability towards the fluorinated end-groups while avoiding interferences from the polymer chains. This approach would consist in determining the PFH dynamics in fluorinated PLA solution and compare it with the fluorocarbon behavior in PLA- C_6H_{13} or other non-fluorinated polymers.

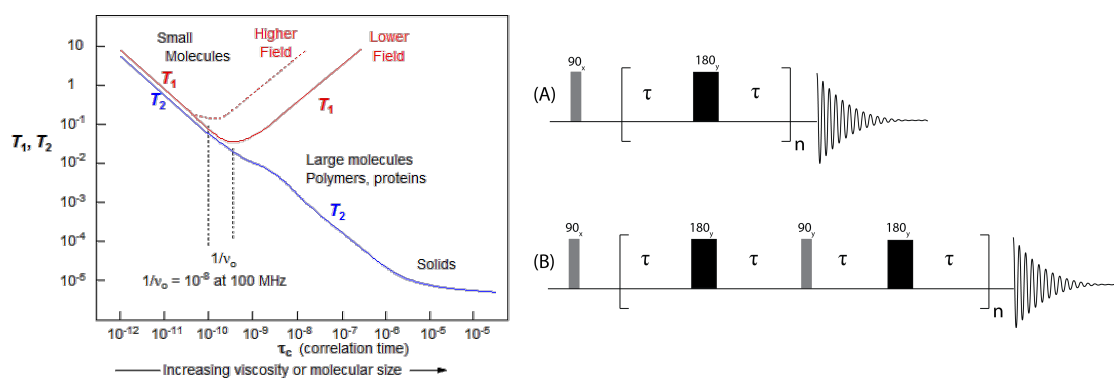


Figure 4. Behavior of T_1 and T_2 as a function of correlation time (left). Pulse sequences for spin-echo CPMG (A) and CPMG with 90_y° refocusing pulse to suppress J modulation (B).

Therefore, our intent is to determine the T_2 of the fluorinated end-groups as well as the free PFH in solution to exclude the interference caused by PLA conformation in the assessment of their interaction. However, we found several difficulties to measure the ^{19}F spin-spin relaxation with the usually employed CPMG pulse sequence (**Figure 4A**); Initially, (1) it was observed that the fluorine intensity was very low relative to the total weighted polymer mass, which required an increased number of scans to provide a relatively good resolution. In turn, it increased considerably the total time of the experiment (~ 12 h for 20 time evolutions); (2) each polymer required the adjustment of the τ (D_{20}) delay for specific CF_2 or CF_3 resonances – for example, to effectively measure the T_2 decay for the CF_3 of PLA-

C_3F_7 , PLA- C_8F_{17} and PLA- $C_{13}F_{27}$ in $CDCl_3$, a τ of 1 ms, 0.5 ms and 0.25 ms were used, respectively. (3) Adding PFH to the polymer solution invariably overlaps many resonances, such as the CF_3 signals for PLA- C_8F_{17} and PLA- $C_{13}F_{27}$, preventing a direct analysis of the PFC effect towards the fluorinated chain. (4) ^{19}F - ^{19}F homonuclear J-coupling that hindered the decay of specific signals or caused them to relax unequally, interfering with a correct correlation and potentially caused the appearance of biexponential profiles in some cases. An example is illustrated in **Figure 5**: the image compares the decay of the CF_3 and aCF_2 resonances of PLA- C_8F_{17} in pure $CDCl_3$. In this case, the signal intensity of aCF_2 decays before the one of CF_3 , indicating a faster relaxation process; however, the low signal intensity and J coupling hinders a precise analysis of this process. Accordingly, both signals suffered intense J modulation because the 180° pulse has double effect of rotating the coherence of one active spin, exchanging α and β states for its coupling partners (Adams, Holroyd et al. 2013). As a result, individual phase corrections at each spectra is required to measure the decay rate, a process that is easier for the CF_3 resonances for their higher intensities than aCF_2 groups. To provide a more accurate measurement and allow the assessment of specific CF_2 resonances, the intense J coupling can be reduced by using multiplet-selective 180° pulses containing an extra 90°_y pulse (**Figure 4B**) that exchanges coherence between spins and reverses the apparent sense of J modulation (Aguilar, Nilsson et al. 2012).

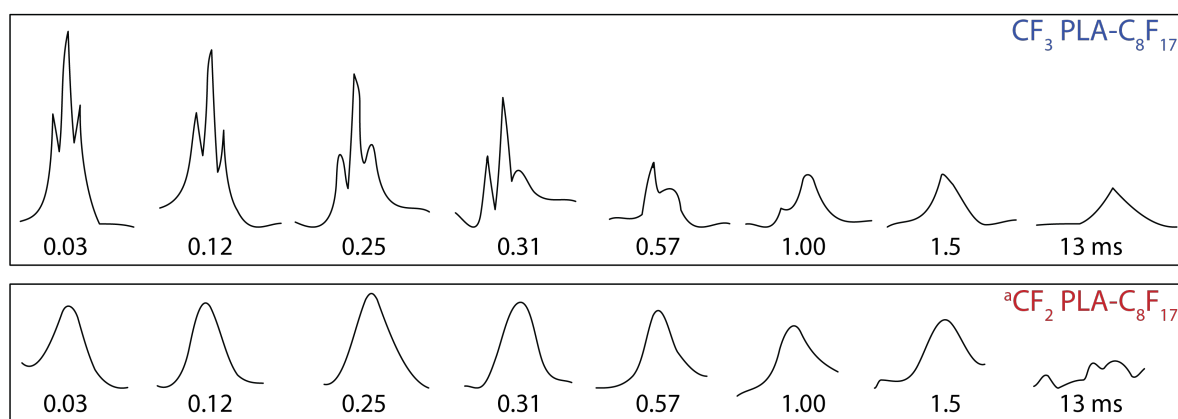


Figure 5. T_2 decay of CF_3 and aCF_2 resonances of PLA- C_8F_{17} obtained in $CDCl_3$ with regular CPMG pulse sequence. Due to loss of coherence, all spectra were individually phase-corrected.

2.3 Solvent influence on PFH entrapment and MC morphology

As previously introduced, entrapping low boiling point PFCs into rigid-shelled structures is a common problem found in many studies (Srinivas, Cruz et al. 2010) (Mousnier, Huang et al. 2014). This issue derives from the stability, non-polar character and weak intermolecular forces that characterize PFCs. According to Horváth, fluorinated molecules are defined as those that contain ≥ 60 weight percent fluorine in $C(sp^3)-F$ bonds; these molecules normally undergo phase-separation from polar and non-polar compounds due to their disinclination to participate in van der Waals interactions (Horváth 1998). In turn, a low miscibility with common organic solvents is observed for liquid PFCs such as perfluorohexane and perfluoropentane (Babiak, Němcová et al. 2008).

As a result, the solvent and its rate of evaporation display a great role in the final morphology of capsules and the final PFC content. We have addressed this issue by comparing the features and the PFH encapsulation in NC and MC produced with CH_2Cl_2 as organic phase (boiling point of $39.6^\circ C$ against $61.2^\circ C$ for $CHCl_3$). CH_2Cl_2 is normally used to produce both NC and MC containing PFOB by the solvent-evaporation process with high entrapment efficiency ($\sim 85\%$) (Diou, Tsapis et al. 2012). However, we observed that the PFH encapsulation was always lower for NC produced with fluorinated and non-fluorinated polymers – in suspension or freeze dried – that were dissolved in CH_2Cl_2 . The NC produced in CH_2Cl_2 exhibited a plateau of 8% against 15% for those produced in $CHCl_3$ (**Figure 6**). As CH_2Cl_2 has a lower boiling point than $CHCl_3$, it evaporates faster and, possibly, exposes PFH to the aqueous media in a more effective manner, which favors the PFC elimination. Comparatively, PFOB has a higher boiling point than PFH ($143^\circ C$ vs $56^\circ C$) and is not as volatile as the latter, a predominant factor that avoids its loss during the solvent-evaporation process. Since PFH and the fluorinated segments present low dipole moments, the utilization of solvents with lower polarizability – the case of $CHCl_3$ compared to CH_2Cl_2 – might enhance their stabilization in solution.

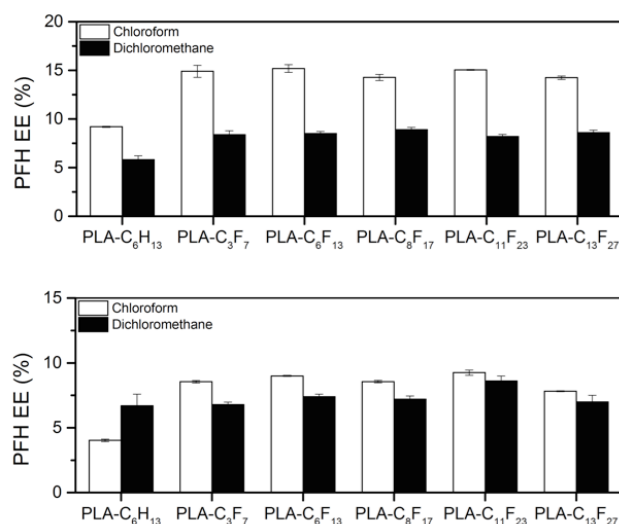


Figure 6. Perfluorohexane entrapment efficiency in nanocapsules prepared in chloroform (white bars) and dichloromethane (dark bars) in suspension (top) and freeze-dried (bottom).

Many solutions are envisioned to enhance PFH entrapment only by modifying the solvent-evaporation conditions. For instance, You *et al.* has utilized isopropanol 5% w/v to rapidly extract the solvent (You, Wang et al. 2016); this approach can potentially decrease the loss of PFC in the initial steps of the process by causing the polymeric shell to precipitate faster and engulf more PFC droplets. Another possibility consists in performing the solvent-evaporation step at lower temperatures in order to decrease the loss of PFH by volatilization and stimulate the shell to precipitate by adding acetone or isopropanol. In both cases, the use of a solvent with higher boiling point and end-group fluorinated polymers could indeed enhance the entrapment of PFCs. Moreover, the employment of fluorescent probes exclusively soluble in the PFC phase could provide important pieces of information regarding the loss and solvation process of PFH during the production of NC and MC. Recently, Sletten *et al.* reported the synthesis of highly fluorinated fluorescent molecules spanning the visible spectrum; many compounds showed stability into the perfluorinated core of nanoemulsions and are promising candidates to aid on the assessment of PFC entrapment, shell stability and *in vivo* imaging (Sletten and Swager 2014).

By dissolving the polymers in CH_2Cl_2 , the morphology of MC changed compared to those produced in CHCl_3 . A clear but subtle distinction was observed according to the fluorinated end-group length in both solvents. In all cases, PLA-

C_6H_{13} , PLA- C_3F_7 and PLA- C_6F_{13} exhibited core-shell morphologies comprising a well centered PFH phase as previously observed for their counterparts prepared in $CHCl_3$; however, increasing the end-group length to PLA- C_8F_{17} , $C_{11}F_{23}$ and $C_{13}F_{27}$ generated proportionally higher extents of randomly distributed or decentered PFH cores (white arrows in **Figure 7**). The difference in MC morphology for samples prepared in those two distinct solvents is illustrated in **Figure 8**. In CH_2Cl_2 , a different molecular conformation may have reduced the fluorophilic character generated by the F-extremities and, consequently, the PFH nucleation occurred faster and more effectively during the solvent evaporation phase. Ultimately, the formation of decentered capsules reflected the distinct spatial arrangement of fluorophilic regions that led the fluorocarbon to phase-separate and nucleate as a single drop in this organic media. Altogether, these results indicate that the final morphology of MC can be adjusted according to the rate of solvent evaporation and end-group length. Because of the several nuclei of PFH, capsules with multinuclear conformation might be more easily disrupted by ultrasound and their utilization in chemoembolization or drug delivery system in regions that are sensitive to temperature variations could be preferred.

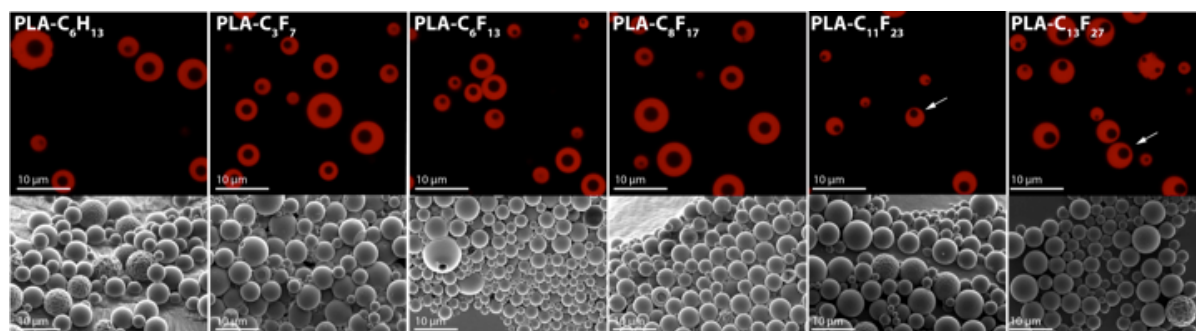


Figure 7. Confocal (top) and scanning electron microscopy (bottom) images of microcapsules formulated in dichloromethane. Scale bar represents 10 µm.

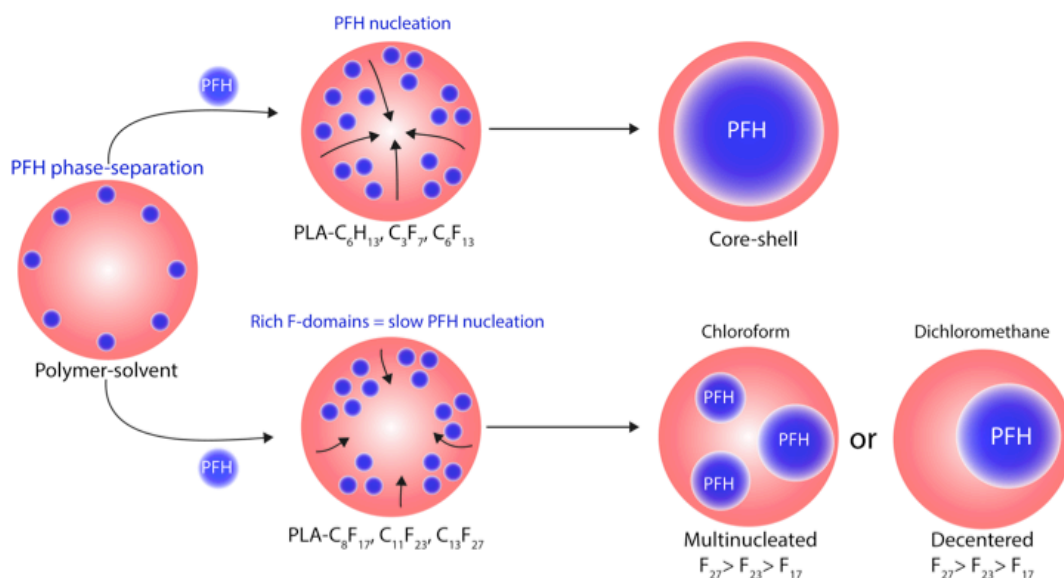


Figure 8. Schematic representation of the perfluorohexane phase-separation and nucleation process in the organic phase constituted by fluorinated polymers of distinct lengths dissolved in chloroform and dichloromethane.

2.4 Theranostic potential

2.4.1 Imaging

2.4.1.2 Ultrasound imaging

Although liquid PFCs are widely explored for their ultrasound imaging potential, few applications describe their echogenic response at the nanoscale. In general, most reports explore the phase-transition behavior of PFP or PFH by stabilizing these materials into micelles or soft shells to generate nanodroplets (Couture, Bevan et al. 2006) (Hannah, Luke et al. 2016). Once irradiated by pulsed-laser or high acoustic pressures, an intense, but transient echo enhancement is observed – as illustrated in **Figure 9** for PFP droplets in distinct US conditions (Williams, Wright et al. 2013). This phenomenon is investigated to image tumor tissues that are susceptible to the EPR effect and to increase specific-tissue detection by targeted agents in ultrasound guided molecular imaging (Marsh, Partlow et al. 2007) (Rapoport, Kennedy et al. 2010) (Sheeran, Streeter et al. 2013)

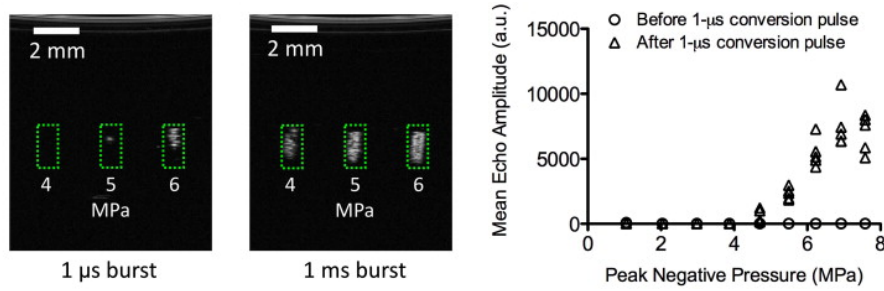


Figure 9: Ultrasound B-mode images at 40 MHz of perfluoropentane nanodroplets. The samples were exposed to 10 MHz bursts of focused ultrasound with peak-negative pressures of 4, 5 and 6 MPa with 1 μ s or 1 ms and the echo amplitude is presented for each respective condition. Adapted from Williams *et al.* (Williams, Wright *et al.* 2013).

Despite their size (~ 150 nm), a limited ultrasound imaging capability is reported for NC containing a PFOB core. Pisani *et al.* considered the role of shell (PLGA) compressibility and sample concentration at clinical US frequencies on the *in vitro* acoustic response (**Figure 10**). The same NC also displayed an effective *in vivo* echo enhancement during concentrated bolus injection (Pisani, Tsapis *et al.* 2008). Comparatively, our PFH NC were able to increase the scattered echo compared to the ones containing PFOB, possibly because of the higher compressibility (1.2×10^{-12} m.kg $^{-3}$ Pa $^{-1}$ for PFH vs 0.6×10^{-12} m.kg $^{-3}$ Pa $^{-1}$ for PFOB) and lower vaporization threshold presented by PFH. Nonetheless, even for such samples, the contrast is not long-lasting and its intensity is several orders of magnitude inferior to the commercially available microbubbles. All these evidences confirm that advances on formulation, the structure of polymeric shell (thickness) and the PFC characteristics might improve the acoustic response of nanostructured systems.

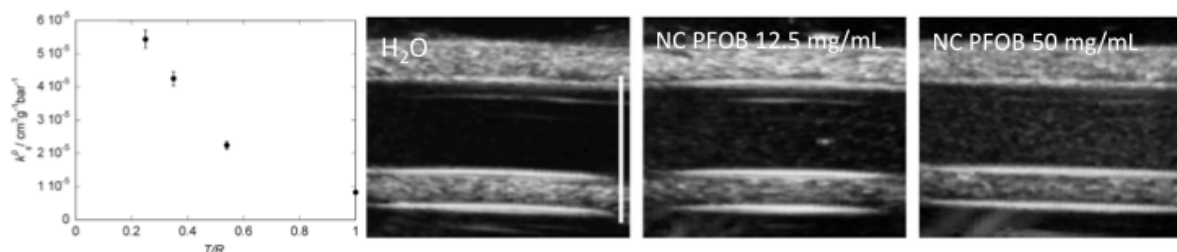


Figure 10: Adiabatic compressibility of NC PFOB as function of thickness-radius ratio (T/R) (left). Higher k° indicates more compressible NC. Ultrasound *in vitro* images in non-linear mode with different sample concentrations (right). Adapted from Pisani *et al.* (Pisani, Tsapis *et al.* 2008)

2.4.1.3 ^{19}F -MR imaging

Furthermore, stabilized PFCs might also be tracked *in vivo* by ^{19}F -MRI; ^{19}F has a gyromagnetic ratio nearly equivalent to the proton, a spin $\frac{1}{2}$ nucleus and 100% of natural abundance. Therefore, exogenously administered fluorinated materials are possible to be monitored without interference from background signal since all fluorine present inside the body is found at the solid state in the bones and teeth – thus, exhibiting very short T_2 relaxation times (Code, McNeill et al. 1990). A series of related NC and NP containing PFC were already analyzed for their ability to generate ^{19}F -MRI contrast, such as perfluorodecalin, perfluorohexane, perfluorooctane, perfluorooctyl bromide and perfluoro-5-crown ether (Srinivas, Cruz et al. 2010) (Dewitte, Geers et al.). Recently, Diou *et al.* disclosed the role of surface PEGylation for PFOB NC to increase the circulation time and allow to detect CT-26 xenograft tumors prone to the EPR effect by ^{19}F -MRI (Figure 11) (Diou, Tsapis et al. 2012).

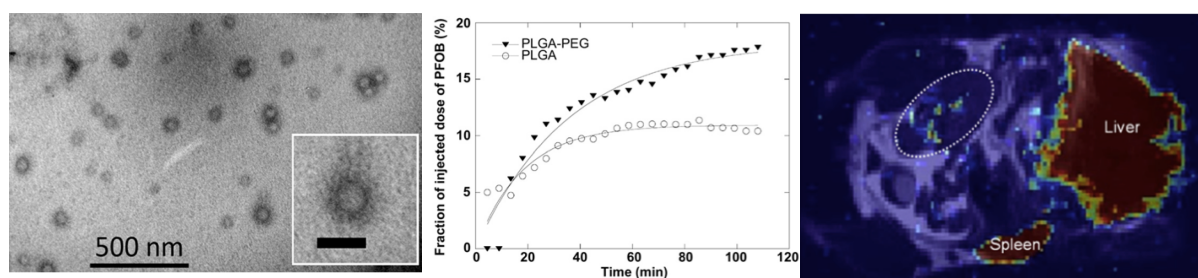


Figure 11: TEM images of PLGA-PEG NC. The insert is a zoom on one capsule to demonstrate a PEG shell (left). Evolution of PFOB concentration in the liver, as measured by ^{19}F -MRI during the first 90 min following the IV administration of PLGA or PLGA-PEG nanocapsules (center). ^{19}F -MR image superimposed with anatomical ^1H -MR image of a tail-head longitudinal cross section of a mouse 7h after intravenous injection of NC for a tumor of 720 mm^3 (white dotted circles) (right). Adapted from Diou *et al.* (Diou, Tsapis et al. 2012).

The ^{19}F spectrum of our NC containing PFH after suspension in aqueous media has confirmed that they also present the potential to be tracked by ^{19}F -MRI; though a more considerate attention must be given to its external interface in order to reduce a fast complement activation and rapid elimination by the mononuclear phagocyte system. Nevertheless, no signals arising from the polymer's CF_3 or CF_2 fluorinated groups were observed, indicating a low segmental mobility once the shell is formed around the PFH core. This effect is particularly illustrated for NC

formulated with PLA-C₃F₇, which displays a CF₃ group resonance at -79.0 ppm that does not overlap with the PFH CF₃ signal (-78.9 ppm) in CDCl₃: as the polymer precipitates at the interface and the NC are resuspended in water, the polymer CF₃ resonance is no longer detectable (**Figure 12**), rendering the shell undetectable by ¹⁹F-MRI – only the PFH signal is potentially considered for this technique.

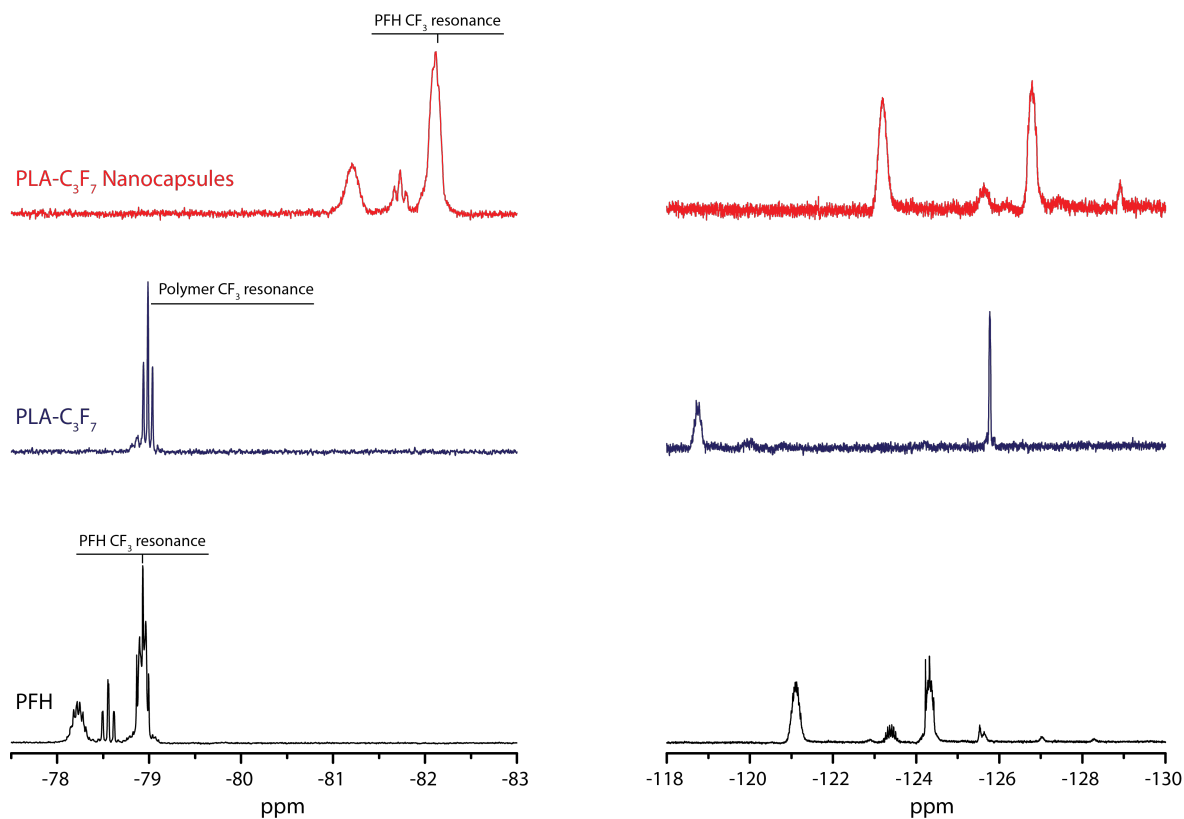


Figure 12: ¹⁹F-NMR magnification of CF₃ and CF₂ regions of concentrated NC formulated with PLA-C₃F₇ (top), pure PLA-C₃F₇ in CDCl₃ (middle) and PFH in CDCl₃ (bottom).

2.4.2 Drug release mediated by ultrasound

Entrapping fully fluorinated liquids into nanostructured systems has offered the possibility to increase the acoustic sensitivity and modulate the material's behavior extra corporeally by ultrasound. Such PFCs present low boiling points and high vapor pressure values compared to other fluorinated liquids: C₅F₁₂ (PFP), C₆F₁₄ (PFH) and C₇F₁₆ vaporize at 87.6, 29.1 and 10.5 kPa at 25°C, respectively. Conversely, PFCs substituted with heteroatoms used as intravascular contrast agents, such as C₈F₁₇Br (PFOB) and C₁₅F₃₀O₅ (PFCE), exhibit vapor pressure values of 1.46 and 0.92 kPa at 25°C, respectively. During an ultrasonic cycle, the

positive and negative pressure peaks oscillates around the atmospheric pressure – 100 kPa – and, thus, PFCs that present higher vapor pressure are exposed for longer periods to the rarefractive phase and may start phase-transition earlier (Singh, Husseini et al. 2012). Therefore, it's easier to attain a gas-phase nucleation by utilizing fully fluorinated PFCs (**Figure 13**).

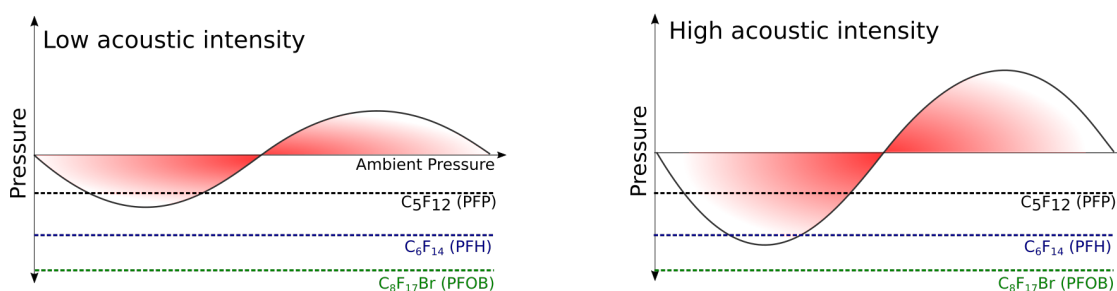


Figure 13: Schematic representation (not in scale) of low and high acoustic pressure variation relative to the vapor pressures of PFP, PFH and PFOB at 25°C. Adapted from Singh *et al.* (Singh, Husseini et al. 2012).

As a result, several biomedical applications explore the liquid-to-gas transition of PFCs that present high vapor pressure values to increase ultrasound scattering of nanostructures (Li, Wang et al. 2014), unblock obstructed blood vessels (You, Wang et al. 2016), deliver O₂ to hypoxic tissues (Song, Feng et al. 2016) and trigger the release of chemotherapeutics in solid tumors (Ektate, Kapoor et al. 2016).

In fact, recent studies have shown the feasibility of entrapping chemotherapeutic agents, such as doxorubicin and paclitaxel into PLGA NC containing a PFOB core – because these drugs present low solubility in fluorinated liquids, they were exclusively distributed along the polymeric thin shell. As reported by Boissenot *et al.*, such loaded NC ameliorated the outcome of CT26 colon cancer cells *in vitro* and *in vivo* compared to the currently employed Taxol[®] (Boissenot, Fattal et al. 2016). However, the treatment improvement is related with passive targeting based on the EPR effect and any specific drug release induced by ultrasound would be hindered because of the PFOB low vapor pressure and high boiling point.

Furthermore, the acoustic response of NC is strictly dependent on the formulation size and the stabilizing layer properties. According to Chlon *et al.*, the use of polymeric layers with higher M_w and crystallinity degrees are related with

decreased acoustic activities and cavitation effects (Chlon, Guedon et al. 2009). In particular, PLA or PLGA layers are described to exhibit low compressibility and generate thick shells that hinder efficient PFC size oscillation (Sarrazin, Tsapis et al. 2016). Thereby, the use of PFP or PFH represents an important evolution to systems that are intended to deliver drugs for their ability to rapidly vaporize under high acoustic pressures and reduce the cavitation threshold to burst the polymeric shell inside the tumor bed, where the chemotherapeutic should be accumulated.

3. References

Abdalkader, R., S. Kawakami, J. Unga, R. Suzuki, K. Maruyama, F. Yamashita and M. Hashida (2015). "Evaluation of the potential of doxorubicin loaded microbubbles as a theranostic modality using a murine tumor model." *Acta Biomaterialia* **19**: 112-118.

Abou-Saleh, R. H., S. A. Peyman, B. R. G. Johnson, G. Marston, N. Ingram, R. Bushby, P. L. Coletta, A. F. Markham and S. D. Evans (2016). "The influence of intercalating perfluorohexane into lipid shells on nano and microbubble stability." *Soft Matter* **12**(34): 7223-7230.

Adams, R. W., C. M. Holroyd, J. A. Aguilar, M. Nilsson and G. A. Morris (2013). ""Perfecting" WATERGATE: clean proton NMR spectra from aqueous solution." *Chemical Communications* **49**(4): 358-360.

Agrawal, A., A. D. Saran, S. S. Rath and A. Khanna (2004). "Constrained nonlinear optimization for solubility parameters of poly(lactic acid) and poly(glycolic acid)—validation and comparison." *Polymer* **45**(25): 8603-8612.

Aguilar, J. A., M. Nilsson, G. Bodenhausen and G. A. Morris (2012). "Spin echo NMR spectra without J modulation." *Chemical Communications* **48**(6): 811-813.

Allen, F. H., P. A. Wood and P. T. A. Galek (2013). "Role of chloroform and dichloromethane solvent molecules in crystal packing: an interaction propensity study." *Acta Crystallographica Section B* **69**(4): 379-388.

Amoozgar, Z., J. Park, Q. Lin and Y. Yeo (2012). "Low Molecular-Weight Chitosan as a pH-Sensitive Stealth Coating for Tumor-Specific Drug Delivery." *Molecular Pharmaceutics* **9**(5): 1262-1270.

Astafyeva, K., L. Somaglino, S. Desgranges, R. Berti, C. Patinote, D. Langevin, F. Lazeyras, R. Salomir, A. Polidori, C. Contino-Pepin, W. Urbach and N. Taulier (2015). "Perfluorocarbon nanodroplets stabilized by fluorinated surfactants:

characterization and potentiality as theranostic agents." Journal of Materials Chemistry B **3**(14): 2892-2907.

Babak, V. G., R. Auzely and M. Rinaudo (2007). "Effect of electrolyte concentration on the dynamic surface tension and dilational viscoelasticity of adsorption layers of chitosan and dodecyl chitosan." Journal of Physical Chemistry B **111**(32): 9519-9529.

Babiak, P., A. Němcová, L. Rulíšek and P. Beier (2008). "On the miscibility of ethers and perfluorocarbons: An experimental and theoretical study." Journal of Fluorine Chemistry **129**(5): 397-401.

Berger, R., G. Resnati, P. Metrangolo, E. Weber and J. Hulliger (2011). "Organic fluorine compounds: a great opportunity for enhanced materials properties." Chemical Society Reviews **40**(7): 3496-3508.

Bloustine, J., T. Virmani, G. M. Thurston and S. Fraden (2006). "Light Scattering and Phase Behavior of Lysozyme-Poly(Ethylene Glycol) Mixtures." Physical Review Letters **96**(8): 087803.

Boissenot, T., E. Fattal, A. Bordat, S. Houvenagel, J. Valette, H. Chacun, C. Gueutin and N. Tsapis (2016). "Paclitaxel-loaded PEGylated nanocapsules of perfluorooctyl bromide as theranostic agents." European Journal of Pharmaceutics and Biopharmaceutics **108**: 136-144.

Borden, M. A., G. V. Martinez, J. Ricker, N. Tsvetkova, M. Longo, R. J. Gillies, P. A. Dayton and K. W. Ferrara (2006). "Lateral Phase Separation in Lipid-Coated Microbubbles." Langmuir **22**(9): 4291-4297.

Chlon, C., C. Guedon, B. Verhaagen, W. T. Shi, C. S. Hall, J. Lub and M. R. Bohmer (2009). "Effect of Molecular Weight, Crystallinity, and Hydrophobicity on the Acoustic Activation of Polymer-Shelled Ultrasound Contrast Agents." Biomacromolecules **10**(5): 1025-1031.

Claridge, T. D. M. (2009). High resolution NMR techniques in organic chemistry. Tetrahedron Organic Chemistry Series.

Code, R. F., K. G. McNeill and J. E. Harrison (1990). "In Vivo measurement of accumulated bone fluorides by nuclear magnetic resonance." Journal of Bone and Mineral Research **5**(S1): S91-S94.

Cool, S. K., B. Geers, S. Roels, S. Stremersch, K. Vanderperren, J. H. Saunders, S. C. De Smedt, J. Demeester and N. N. Sanders (2013). "Coupling of drug containing liposomes to microbubbles improves ultrasound triggered drug delivery in mice." J Control Release **172**(3): 885-893.

Corbet, C., H. Ragelle, V. Pourcelle, K. Vanvarenberg, J. Marchand-Brynaert, V. Pr at and O. Feron (2016). "Delivery of siRNA targeting tumor metabolism using non-covalent PEGylated chitosan nanoparticles: Identification of an optimal combination of ligand structure, linker and grafting method." Journal of Controlled Release **223**: 53-63.

Couture, O., P. D. Bevan, E. Cherin, K. Cheung, P. N. Burns and F. S. Foster (2006). "Investigating perfluorohexane particles with high-frequency ultrasound." Ultrasound in Medicine & Biology **32**(1): 73-82.

Dewitte, H., B. Geers, S. Liang, U. Himmelreich, J. Demeester, S. C. De Smedt and I. Lentacker "Design and evaluation of theranostic perfluorocarbon particles for simultaneous antigen-loading and ¹⁹F-MRI tracking of dendritic cells." Journal of Controlled Release **169**(1-2): 141-149.

Diou, O., N. Tsapis, C. Giraudeau, J. Valette, C. Gueutin, F. Bourasset, S. Zanna, C. Vauthier and E. Fattal (2012). "Long-circulating perfluorooctyl bromide nanocapsules for tumor imaging by (FMRI)-F-19." Biomaterials **33**(22): 5593-5602.

Duncanson, W. J., L. R. Arriaga, W. L. Ung, J. A. Kopechek, T. M. Porter and D. A. Weitz (2014). "Microfluidic Fabrication of Perfluorohexane-Shelled Double Emulsions for Controlled Loading and Acoustic-Triggered Release of Hydrophilic Agents." Langmuir **30**(46): 13765-13770.

Ektate, K., A. Kapoor, D. Maples, A. Tuysuzoglu, J. VanOsdol, S. Ramasami and A. Ranjan (2016). "Motion Compensated Ultrasound Imaging Allows Thermometry and Image Guided Drug Delivery Monitoring from Echogenic Liposomes." Theranostics **6**(11): 1963-1974.

Foster, T., K. D. Dorfman and H. Ted Davis (2010). "Giant biocompatible and biodegradable PEG-PMCL vesicles and microcapsules by solvent evaporation from double emulsion droplets." Journal of Colloid and Interface Science **351**(1): 140-150.

Hannah, A. S., G. P. Luke and S. Y. Emelianov (2016). "Blinking Phase-Change Nanocapsules Enable Background-Free Ultrasound Imaging." Theranostics **6**(11): 1866-1876.

Horv th, I. T. (1998). "Fluorous Biphasic Chemistry." Accounts of Chemical Research **31**(10): 641-650.

Hosny, N. A., G. Mohamedi, P. Rademeyer, J. Owen, Y. Wu, M.-X. Tang, R. J. Eckersley, E. Stride and M. K. Kuimova (2013). "Mapping microbubble viscosity using fluorescence lifetime imaging of molecular rotors." Proceedings of the National Academy of Sciences **110**(23): 9225-9230.

Huynh, E., Y. C. LeungBen, B. L. Helfield, M. Shakiba, J.-A. Gandier, C. S. Jin, E. R. Master, B. C. Wilson, D. E. Goertz and G. Zheng (2015). "In situ conversion of

porphyrin microbubbles to nanoparticles for multimodality imaging." *Nat Nano* **10**(4): 325-332.

Ishak, R. A. H., G. A. S. Awad, N. M. Zaki, A. E.-H. A. El-Shamy and N. D. Mortada (2013). "A comparative study of chitosan shielding effect on nano-carriers hydrophilicity and biodistribution." *Carbohydrate Polymers* **94**(1): 669-676.

Koda, Y., T. Terashima and M. Sawamoto (2014). "Fluorous Microgel Star Polymers: Selective Recognition and Separation of Polyfluorinated Surfactants and Compounds in Water." *Journal of the American Chemical Society* **136**(44): 15742-15748.

Koda, Y., T. Terashima and M. Sawamoto (2015). "Fluorinated Microgels in Star Polymers: From In-Core Dynamics to Fluorous Encapsulation." *Macromolecules* **48**(9): 2901-2908.

Lentacker, I., B. Geers, J. Demeester, S. C. De Smedt and N. N. Sanders (2009). "Design and Evaluation of Doxorubicin-containing Microbubbles for Ultrasound-triggered Doxorubicin Delivery: Cytotoxicity and Mechanisms Involved." *Mol Ther* **18**(1): 101-108.

Li, H., J. Wang, P. Wang, J. Zheng, F. Song, T. Yin, G. Zhou, R. Zheng and C. Zhang (2014). "Phase-transition contrast nanocapsules triggered by low-intensity ultrasound." *Chemical Communications* **50**(96): 15163-15166.

Li, W., H. Dong, G. Tang, T. Ma and X. Cao (2015). "Controllable microfluidic fabrication of Janus and microcapsule particles for drug delivery applications." *RSC Advances* **5**(30): 23181-23188.

Liao, A.-H., Y.-J. Lu, Y.-C. Lin, H.-K. Chen, H.-K. Sytwu and C.-H. Wang (2016). "Effectiveness of a Layer-by-Layer Microbubbles-Based Delivery System for Applying Minoxidil to Enhance Hair Growth." *Theranostics* **6**(6): 817-827.

Liu, X., K. A. Howard, M. Dong, M. Ø. Andersen, U. L. Rahbek, M. G. Johnsen, O. C. Hansen, F. Besenbacher and J. Kjems (2007). "The influence of polymeric properties on chitosan/siRNA nanoparticle formulation and gene silencing." *Biomaterials* **28**(6): 1280-1288.

Marsh, J. N., K. C. Partlow, D. R. Abendschein, M. J. Scott, G. M. Lanza and S. A. Wickline (2007). "Molecular imaging with targeted perfluorocarbon nanoparticles: Quantification of the concentration dependence of contrast enhancement for binding to sparse cellular epitopes." *Ultrasound in Medicine and Biology* **33**(6): 950-958.

Moghimi, S. M., A. J. Andersen, D. Ahmadvand, P. P. Wibroe, T. L. Andresen and A. C. Hunter (2011). "Material properties in complement activation." *Adv Drug Deliv Rev* **63**(12): 1000-1007.

Mousnier, L., N. Huang, E. Morvan, E. Fattal and N. Tsapis (2014). "Influence of polymer end-chemistry on the morphology of perfluorohexane polymeric microcapsules intended as ultrasound contrast agents." Int J Pharm **471**(1-2): 10-17.

Mura, S. and P. Couvreur (2012). "Nanotheranostics for personalized medicine." Adv Drug Deliv Rev **64**(13): 1394-1416.

Pisani, E., N. Tsapis, B. Galaz, M. Santin, R. Berti, N. Taulier, E. Kurtisovski, O. Lucidarme, M. Ourevitch, B. T. Doan, J. C. Beloeil, B. Gillet, W. Urbach, S. L. Bridal and E. Fattal (2008). "Perfluorooctyl Bromide Polymeric Capsules as Dual Contrast Agents for Ultrasonography and Magnetic Resonance Imaging." Advanced Functional Materials **18**(19): 2963-2971.

Pisani, E., N. Tsapis, J. Paris, V. Nicolas, L. Cattel and E. Fattal (2006). "Polymeric nano/microcapsules of liquid perfluorocarbons for ultrasonic imaging: physical characterization." Langmuir **22**(9): 4397-4402.

Preuschen, J., S. Menchen, M. A. Winnik, A. Heuer and H. W. Spiess (1999). "Aggregation Behavior of a Symmetric, Fluorinated, Telechelic Polymer System Studied by ¹⁹F NMR Relaxation." Macromolecules **32**(8): 2690-2695.

Rapoport, N., A. M. Kennedy, J. E. Shea, C. L. Scaife and K.-H. Nam (2010). "Ultrasonic Nanotherapy of Pancreatic Cancer: Lessons from Ultrasound Imaging." Molecular Pharmaceutics **7**(1): 22-31.

Sarrazin, B., N. Tsapis, L. Mousnier, N. Taulier, W. Urbach and P. Guenoun (2016). "AFM Investigation of Liquid-Filled Polymer Microcapsules Elasticity." Langmuir **32**(18): 4610-4618.

Schindler, A. and D. Harper (1979). "Polylactide. II. Viscosity–molecular weight relationships and unperturbed chain dimensions." Journal of Polymer Science: Polymer Chemistry Edition **17**(8): 2593-2599.

Shapiro, G., A. W. Wong, M. Bez, F. Yang, S. Tam, L. Even, D. Sheyn, S. Ben-David, W. Tawackoli, G. Pelled, K. W. Ferrara and D. Gazit (2016). "Multiparameter evaluation of in vivo gene delivery using ultrasound-guided, microbubble-enhanced sonoporation." Journal of Controlled Release **223**: 157-164.

Sheeran, P. S., J. E. Streeter, L. B. Mullin, T. O. Matsunaga and P. A. Dayton (2013). "Toward Ultrasound Molecular Imaging With Phase-Change Contrast Agents: An In Vitro Proof of Principle." Ultrasound in Medicine & Biology **39**(5): 893-902.

Singh, R., G. A. Hussein and W. G. Pitt (2012). "Phase transitions of nanoemulsions using ultrasound: Experimental observations." Ultrasonics Sonochemistry **19**(5): 1120-1125.

Sletten, E. M. and T. M. Swager (2014). "Fluorofluorophores: Fluorescent Fluorous Chemical Tools Spanning the Visible Spectrum." Journal of the American Chemical Society **136**(39): 13574-13577.

Song, X., L. Feng, C. Liang, K. Yang and Z. Liu (2016). "Ultrasound Triggered Tumor Oxygenation with Oxygen-Shuttle Nanoperfluorocarbon to Overcome Hypoxia-Associated Resistance in Cancer Therapies." Nano Letters **16**(10): 6145-6153.

Srinivas, M., L. J. Cruz, F. Bonetto, A. Heerschap, C. G. Figdor and I. J. M. de Vries (2010). "Customizable, multi-functional fluorocarbon nanoparticles for quantitative in vivo imaging using F-19 MRI and optical imaging." Biomaterials **31**(27): 7070-7077.

Sun, Y., Y. Zheng, H. Ran, Y. Zhou, H. Shen, Y. Chen, H. Chen, T. M. Krupka, A. Li, P. Li, Z. Wang and Z. Wang (2012). "Superparamagnetic PLGA-iron oxide microcapsules for dual-modality US/MR imaging and high intensity focused US breast cancer ablation." Biomaterials **33**(24): 5854-5864.

Tonelli, A. E. (2014). "PLLA in Solution: A Flexible Random-Coil or an Extended, Rather Rigid Helical Polymer." Macromolecules **47**(17): 6141-6143.

Tsunoda, S., O. Mazda, Y. Oda, Y. Iida, S. Akabame, T. Kishida, M. Shin-Ya, H. Asada, S. Gojo, J. Imanishi, H. Matsubara and T. Yoshikawa (2005). "Sonoporation using microbubble BR14 promotes pDNA/siRNA transduction to murine heart." Biochemical and Biophysical Research Communications **336**(1): 118-127.

Van Woensel, M., N. Wauthoz, R. Rosière, V. Mathieu, R. Kiss, F. Lefranc, B. Steelant, E. Dilissen, S. W. Van Gool, T. Mathivet, H. Gerhardt, K. Amighi and S. De Vleeschouwer (2016). "Development of siRNA-loaded chitosan nanoparticles targeting Galectin-1 for the treatment of glioblastoma multiforme via intranasal administration." Journal of Controlled Release **227**: 71-81.

Vandenbroucke, R. E., I. Lentacker, J. Demeester, S. C. De Smedt and N. N. Sanders (2008). "Ultrasound assisted siRNA delivery using PEG-siPlex loaded microbubbles." Journal of Controlled Release **126**(3): 265-273.

Williams, R., C. Wright, E. Cherin, N. Reznik, M. Lee, I. Gorelikov, F. S. Foster, N. Matsuura and P. N. Burns (2013). "Characterization of Submicron Phase-change Perfluorocarbon Droplets for Extravascular Ultrasound Imaging of Cancer." Ultrasound in Medicine & Biology **39**(3): 475-489.

Yang, H., W. Cai, L. Xu, X. Lv, Y. Qiao, P. Li, H. Wu, Y. Yang, L. Zhang and Y. Duan (2015). "Nanobubble-Affibody: Novel ultrasound contrast agents for targeted molecular ultrasound imaging of tumor." Biomaterials **37**: 279-288.

You, Y. F., Z. G. Wang, H. T. Ran, Y. Y. Zheng, D. Wang, J. S. Xu, Z. B. Wang, Y. Chen and P. Li (2016). "Nanoparticle-enhanced synergistic HIFU ablation and

transarterial chemoembolization for efficient cancer therapy." Nanoscale **8**(7): 4324-4339.

Yu, F. T. H., X. Chen, J. Wang, B. Qin and F. S. Villanueva (2016). "Low Intensity Ultrasound Mediated Liposomal Doxorubicin Delivery Using Polymer Microbubbles." Molecular Pharmaceutics **13**(1): 55-64.

Zarzar, L. D., V. Sresht, E. M. Sletten, J. A. Kalow, D. Blankschtein and T. M. Swager (2015). "Dynamically reconfigurable complex emulsions via tunable interfacial tensions." Nature **518**(7540): 520-524.

General conclusion

The work developed in this thesis has demonstrated that the stability and the content of perfluocarbons, either gaseous or liquids, can be improved in micron or nano-sized systems. As a consequence of the functional chitosan layer or the fluorinated end-groups, the acoustic response and the ultrasound signal persistence was greatly enhanced. All such results allow us to consider the employment of related systems as theranostic tools to diagnose and treat tumors in the future. Nonetheless, the translation of such technology to the clinical practice would require even higher entrapment efficiencies of PFH and extend the persistence of the gaseous decafluorobutane core *in vivo*. Both agents still require adjustments in the formulation, such as the presence of external PEGylated chains to ensure furtivity and passively target tumor tissues by the EPR effect. Furthermore, the thickness (or other parameters, e.g. surface charge, conformation and crystallinity) of the polymeric layers would have to be adapted according to the total drug dose required for the treatment as well as the ultrasound acoustic intensity necessary to disrupt the polymeric layers *in vivo*. As very few is currently known about the impact of fluorinated end-groups, specific assays intended to disclose their bioaccumulative effect are also required. Although the systems described so far are not fully adapted to deliver drug payloads, their assembly and characterization represents only the initial steps towards the synthesis of fully capable theranostic agents. Altogether, the novel microvesicles and nanocapsules develop in this thesis are promising candidates to enhance the therapeutic outcomes of solid tumors and other diseases.